Temporal tissue dynamics from a single snapshot

Jonathan Somer[1,2], Shie Mannor[1,3], Uri Alon[2,3]

1. Technion Israel Institute of Technology, Department of Electrical & Computer Engineering
2. Weizmann Institute of Science, Department of Molecular Cell Biology
3. Email: shie@technion.ac.il, uri.alon@weizmann.ac.il

Abstract:

Physiological and pathological processes such as inflammation or cancer emerge from the interactions between cells over time. However, methods to follow cell populations over time within the native context of a human tissue are lacking, since tissue biopsy offers only a single snapshot. Here we present one-shot tissue dynamics reconstruction (OSDR), an approach to estimate a dynamical model of cell populations based on a single tissue sample. OSDR uses spatial proteomics data to learn how the composition of cellular neighborhoods influences division rate, providing a dynamical model of cell population change over time. We apply OSDR to human breast cancer data, and reconstruct two fixed points of fibroblasts and macrophage interactions. These fixed points correspond to hot and cold fibrosis, in agreement with co-culture experiments that measured dynamics directly. We then use OSDR to discover a pulse-generating excitable circuit of T and B cells in the tumor microenvironment, suggesting temporal flares of adaptive anti-cancer responses. OSDR can be applied to a wide range of spatial transcriptomic or proteomic assays to enable analysis of tissue dynamics based on patient biopsies.

Introduction:

Physiological processes involve cell populations that change over time (Adler, Chavan, and Medzhitov 2023). Some cell populations expand and others are removed, as occurs in development and in the immune response to pathogens ("The Spectrum of Inflammatory Responses," n.d.). A clinically important example of changing cell populations is the evolution of the cancer microenvironment, in which the growing tumor recruits stromal and immune cells that are crucial for tumor survival (Sahai et al. 2020; Mayer et al. 2023; Gascard and Tlsty 2016; Tlsty and Coussens 2006; Schürch et al. 2020; Binnewies et al. 2018; Combes, Samad, and Krummel 2023). Understanding cell dynamics and the underlying cell-cell communication circuits is a major goal of tissue biology. Understanding these circuits can enable new treatment strategies based on sculpting cell populations in desired ways (Wang et al. 2023).

However, measuring the dynamics of cell populations in human tissues is currently very difficult. Biopsies provide a single snapshot, and taking multiple biopsies is unfeasible and does not provide longitudinal evidence from the same cells.

Current strategies to measure tissue dynamics do not apply to human biopsy. For example cell lines, mice, organ-on-a-chip (Leung et al. 2022) or organoid models (Kim, Koo, and Knoblich 2020) are treated as replicas and are analyzed at different time points. Ex-vivo tissues can be followed over time but lack the native immune context (Kokkinos et al. 2021). Intravital

fluorescence microscopy has made it possible to follow living cells within animal models (Pittet et al. 2018; Entenberg, Oktay, and Condeelis 2023). Recent advances employ synthetic biology to engineer cells to record their activity or lineage ((Quinn et al. 2021), *Horns et al. 2023*). These approaches are restricted to animal models or in vitro-settings, limiting their ability to capture the complexity of *in vivo* dynamics in humans.

The emergence of single-cell technologies offers new opportunities for studying tissues at high resolution. Notable approaches use single-cell data for understanding cell-cell communication at a single time point (Efremova et al. 2020; Jerby-Arnon and Regev 2022; Browaeys, Saelens, and Saeys 2020; Armingol, Baghdassarian, and Lewis 2024). Other approaches attempt to infer dynamics of processes such as transcription within individual cells on a timescale of hours, such as RNA velocity, ergodic rate analysis and Zman-seq (La Manno et al. 2018; Kafri et al. 2013; Kirschenbaum et al. 2023). These methods do not address the challenge of understanding how cell populations change on the tissue level, processes that could take days to weeks.

Here we present an approach to estimate cell population dynamics based on a spatial biopsy snapshot (Figure 1A). This approach, ‘One-Shot Tissue Dynamics Reconstruction’ (OSDR), is based on using a cell-division marker to determine division rates as a function of neighborhood composition, providing a dynamical model of how cell populations change over time. We apply OSDR to human breast cancer spatial proteomics samples, and reconstruct a fibroblast-macrophage circuit with two steady states of hot and cold fibrosis, in agreement with co-culture experiments that measure dynamics directly. We then use OSDR to discover a pulse-generating excitable circuit of T cells and B cells, suggesting that cancer surveillance in the tumor microenvironment operates in temporal flares, as opposed to the steady-state picture implicit in current literature. The present approach opens the way to infer cell population dynamics from a single snapshot of patient biopsies.

(A) **Overview of One-Shot Tissue Dynamics Reconstruction (OSDR)**

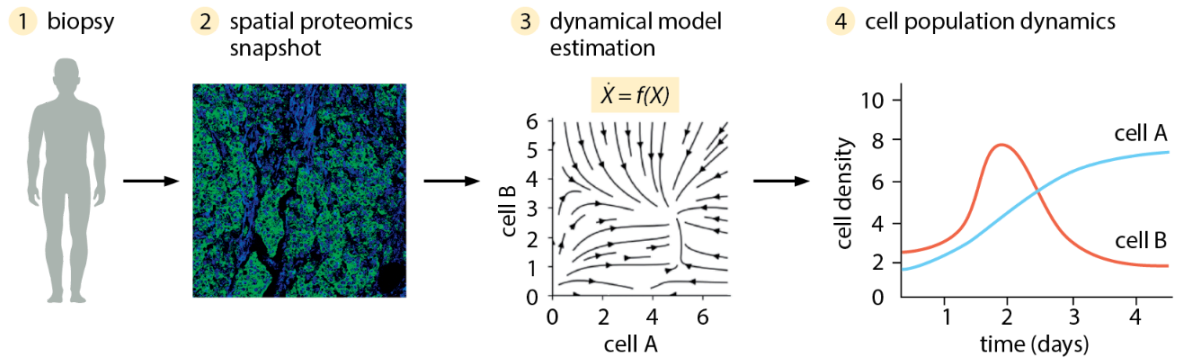

(B) **Neighborhood composition maps to a location in state-space**

(C) **Cell division and death markers determine change in tissue composition**

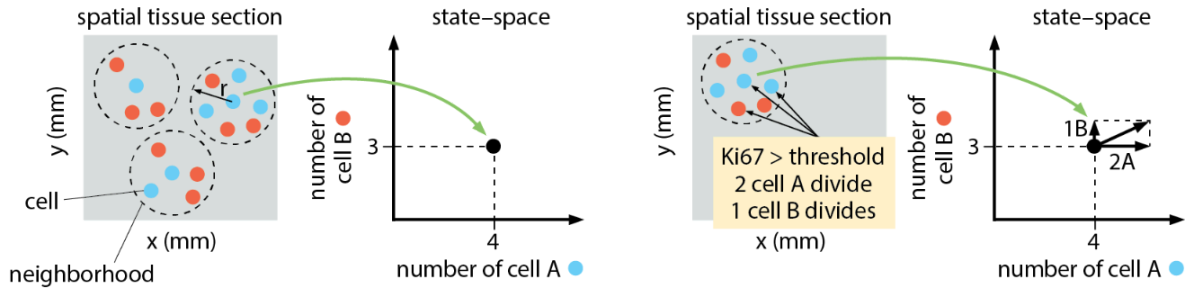

(D) **Breast-cancer tissue with neighborhood mapped to a location in a phase-portrait estimated by OSDR**

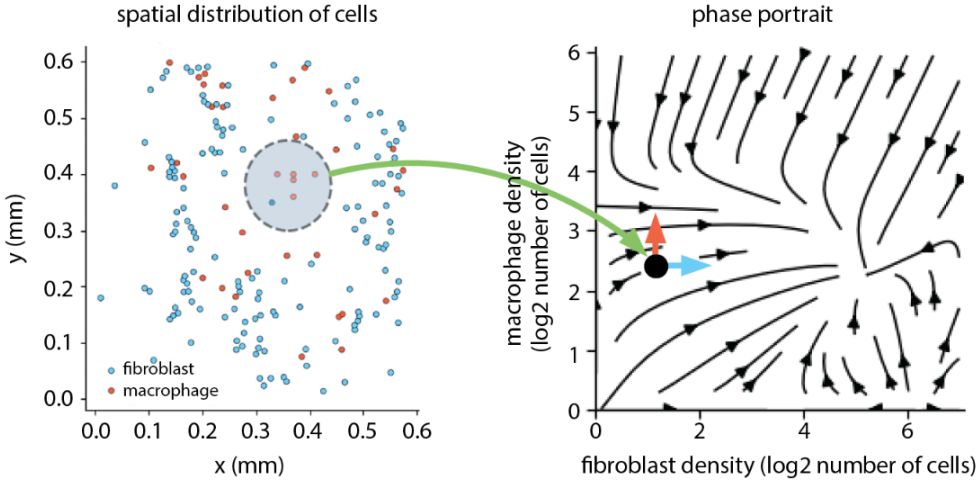

(E) **Probabilistic division and death events for each cell produce a stochastic trajectory of tissue composition over time**

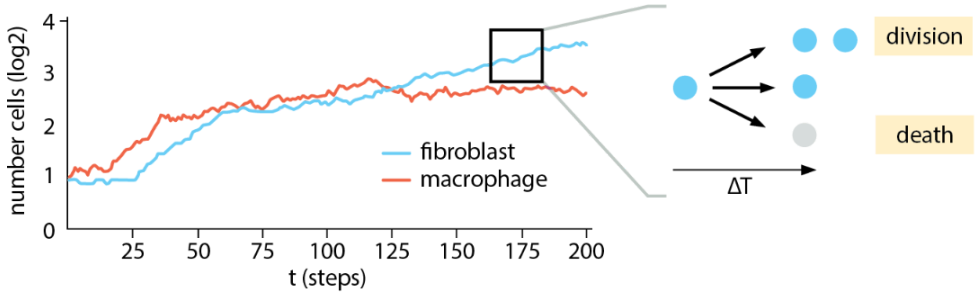

Figure 1: Overview of One-Shot Tissue Dynamics Reconstruction (OSDR). A) Overview: OSDR uses spatial proteomics of a biopsy to infer cell population dynamics. B) The number of cells in a neighborhood map to a location in state-space. C) Cell division rates, inferred from markers, determine the direction of change in state-space. D) Example breast-cancer tissue section (left) from a dataset by Danenberg et al. 2022. Gray circle marks a neighborhood in the tissue. The neighborhood is mapped to its corresponding location in a phase portrait estimated using OSDR (right). E) OSDR can simulate stochastic future trajectories of cell populations.

Results

Approach for inferring cellular population dynamics from a spatial omics snapshot

The aim of this study is to introduce a method for inferring a dynamical model of cell populations based on a single tissue sample (Fig 1A), and to use this method to understand the dynamics of the breast cancer microenvironment.

We consider biopsy sections stained for proteins that include cell type markers and cell-division markers. Specifically here we use MIBI spatial proteomics samples (Keren et al. 2019), but in principle other spatial proteomic or spatial transcriptomic assays can also be used (Methods). From this data we generate a list of cell locations and division status for each cell type. We model this snapshot data as a dynamical system. The variables are cell concentrations, such as fibroblasts per unit area. In such a system, the change in cell counts will be a balance between division, death, and migration. Our goal is to infer this dynamical system, and use it to predict the future changes in cell populations.

We separate the dynamics into two parts, one that results from cell division and death within a tissue, and a second part that results from migration and influx of cells from circulation. We infer the first component from markers for cell division or death. We then use this estimated component to quantify the net contribution of external sources of cells (Methods, S5,6). In our analyses local proliferation and removal explained the cell population dynamics.We therefore focus on the dynamical equations for the rate of change of each cell type given by its division rate minus removal rate. This model captures the dynamics resulting from growth-factor signaling circuits within a tissue.

The key idea is to use a spatial omics snapshot in order to estimate the division and removal rates of cells by means of molecular markers for division (and if available, removal), as a function of the composition of the cells neighborhood.

In order to estimate the effect of each cell type on the growth and removal of other cells, we assume that the local neighborhood surrounding each cell observed in a biopsy slide contains growth factors secreted by nearby cells. We thus tabulate, for each cell in a slide, its type, as well as the number and types of cells within a radius r (Fig 1B). We use r=80um based on measurements of in-vivo cell-cell interaction ranges (Oyler-Yaniv et al. 2017) (Methods). The results are not sensitive to the choice of radius r (S3E, S4F).

We represent each possible neighborhood composition as a point in a state space whose axes are the numbers of cells of each type (Fig 1B). The rate of change of the cell concentrations in a given neighborhood is deduced from division markers. By using data on many different neighborhoods, available from the spatial heterogeneity of the samples, one obtains the probability of division as a function of neighborhood cell composition (equations in Fig2, Methods). This provides the direction of change for each neighborhood composition, the velocity vector v, represented by an arrow in the state space (Fig 1C). Taking all of the data together provides the phase portrait, which shows the entire dynamics (Fig 1D). The phase portrait

allows detection of the system's stable fixed points, and predicts cell population dynamics from any initial concentration (Fig 1E).

This approach is precise when cells across the sample obey the same underlying dynamics. In reality, varying proximity to blood vessels or tumor mass can create zones with different levels of metabolites, hypoxia, inflammation and other factors that can affect the dynamics (Setten et al. 2022). To control for these effects, we show below that the estimated dynamics are preserved across such zones by including terms for density of endothelial or tumor cells in our model (S3G, S4G). We also show that the estimated dynamics are preserved across various patient subgroups defined by external factors such as tumor genetics or stage (S3H, S4H).

This is a general approach that can be tailored to diverse spatial omics technologies (Methods). In order to implement this using current datasets, we developed software that can be applied to spatial data that includes the commonly measured cell division marker KI67. We define division events using KI67 thresholds based on experiments in human cell lines by Uxa et al. 2021 (Methods, Fig 2A).

Ideally one would also like a marker for cell death, but currently available markers are not generally considered to be sufficient to quantify cell death (Kari et al. 2022). To make progress we bypass the death marker by assuming that death rate is a constant for each cell type, namely that removal rate is not affected by the composition of the cell's neighborhood. We find that the results are robust to wide variations in the value of this constant removal rate (S3F, S4D). To be concrete, we therefore approximate the removal rate by the mean division rate for each cell type - an assumption that is exact in the case of (quasi) steady state tissues in which mean removal and division rates are equal.

To estimate the division probability as a function of neighboring cell composition, we consider neighborhoods of radius r around each cell, and tabulate division (KI67 > threshold) as a function of neighborhood composition (Fig 2A,B). We then model the dependence of the probability to divide on composition with logistic regression. Other types of statistical or machine learning models can also be used. We use the estimated models to construct a stochastic equation for division minus death rate (Fig. 2C). Plotting the expected direction of change for each possible neighborhood composition produces a phase portrait (Fig 2D). We call this approach one-shot tissue dynamics reconstruction (OSDR). Its essential advance is the use of division rates measured at the level of single cells at one time-point to produce dynamics at the level of tissues.

To test the feasibility of the OSDR approach, we begin with simulated data. We asked how many cells are required in order to reconstruct a known dynamical system. In each simulation we stipulate a specific dynamical system in which cells affect each other's growth rate. We then simulate experimental spatial data by running the dynamics from various initial conditions of cell density, for a period of time that results in distributions of spatial cell concentrations that resemble experimental data. This creates a variety of cell compositions.

We used OSDR to reconstruct the phase portraits and compared them to the actual phase portrait of the known dynamic system used in each simulation. We studied all possible phase

portrait topologies of two cell types, where each cell type can be stable on its own, or stable only in the presence of the other cell type. This results in 4 phase portrait topologies (Fig 2E). We find that a few thousand cells are typically sufficient to reconstruct the fixed point structure reliably (S2 D,E,F,G,H). We conclude that the OSDR algorithm can reconstruct simple 2D dynamics from simulated cell data and recover the underlying phase portrait given enough cells.

(A) **Division marker KI67 > threshold defines division events during past Δt**

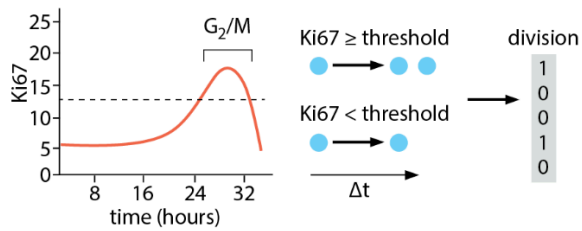

(B) **OSDR predicts a cell's probability for division using the number of cells of each type within a radius r**

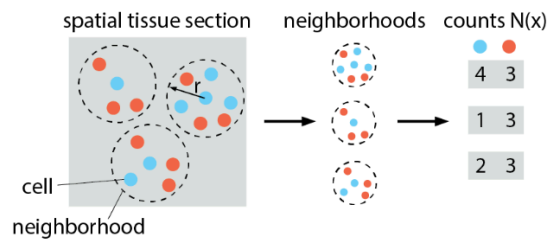

(C) **OSDR is based on a probabilistic rate equation**

deterministic rate equation:

$$\frac{dX}{dt} = \frac{\#\,\text{divisions}}{dt} - \frac{\#\,\text{deaths}}{dt}$$

stochastic equation (OSDR):

$$\frac{dX}{\Delta t} = \sum_{x \in \text{tissue}} O(x) \qquad O(x) = \begin{cases} +1/\Delta t & \text{with probability: } p^{+}(N(x)) \\ -1/\Delta t & p^{-}(N(x)) \\ 0 & \text{remaining} \end{cases}$$

division and death probabilities, p^{+} and p^{-}, depend on each cell's neighborhood $N(x)$, and are estimated using statistical models

(D) **A deterministic ordinary differential equation can be derived from the stochastic models using the expected direction of change**

$$X := \begin{bmatrix} X_1 \\ X_2 \\ \vdots \\ X_k \end{bmatrix} \qquad \frac{d}{dt} X = f(X) = \begin{bmatrix} E[\frac{d}{\Delta t} X_1] \\ E[\frac{d}{\Delta t} X_2] \\ \vdots \\ E[\frac{d}{\Delta t} X_k] \end{bmatrix}$$

each coordinate in the state vector is the density of one cell type

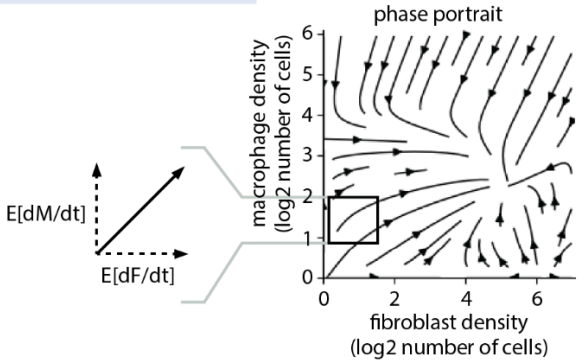

(E) **OSDR accurately reconstructs dynamics from simulations of known dynamical circuits**

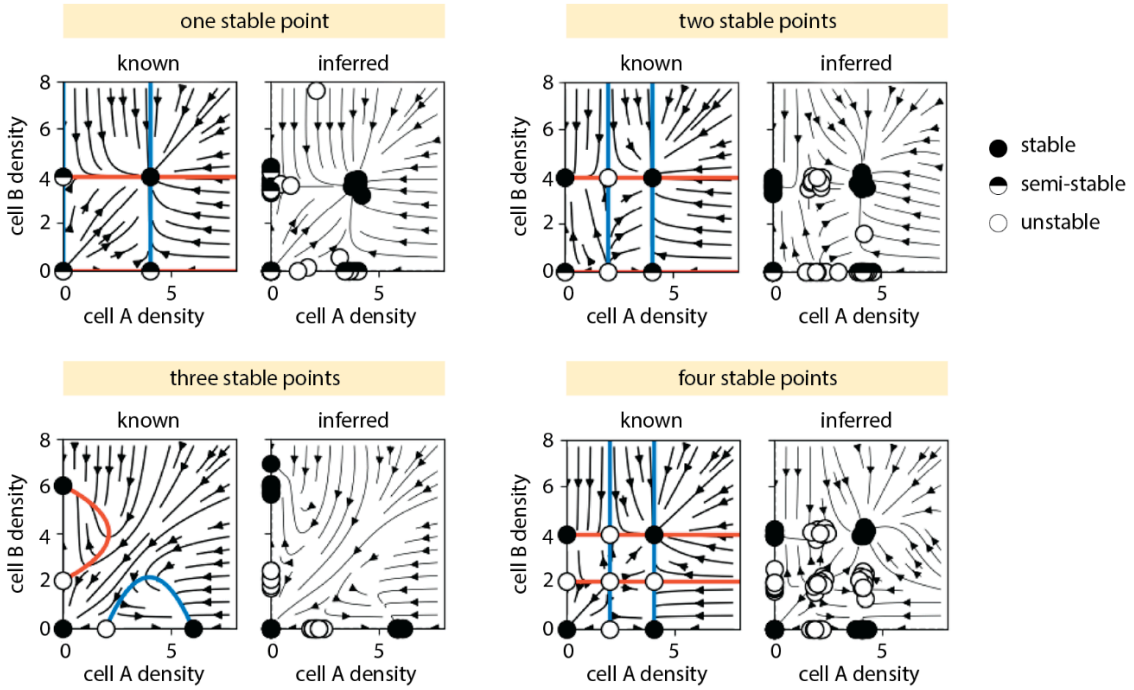

Figure 2: OSDR approach for inferring cell dynamics based on a spatial proteomics snapshot. A) Division events are defined by Ki67 measurement above a threshold. B) Cell division probability is inferred as a function of neighborhood composition using logistic regression. C) rate equations are inferred from division probability as a function of neighborhood composition. D) OSDR provides a phase portrait and differential equations for calculating cell population dynamics. E) OSDR accurately reconstructed dynamics from simulations of known dynamical circuits based on simulated data of 10,000 cells. '*Known'* figures (left) display the ground-truth model used during simulation. Arrows indicate directions of change and colored lines are nullclines in which only one cell type changes. Black dots and white dots are stable and unstable fixed points. '*Inferred'* figures display the estimated fixed points from 10 simulations, for the four two-cell phase portrait topologies. Each *Inferred* figure also displays the OSDR arrows from the first simulation of the 10.

OSDR reconstructs breast cancer fibroblast and macrophage dynamics in agreement with in-vitro dynamic experiments.

We next test the OSDR approach using spatial proteomics data. We selected the breast cancer microenvironment as a useful test case because of recent work which established *in vitro* dynamics for fibroblasts and macrophages in a breast cancer medium (Mayer et al. 2023), supplying a reference phase portrait for the cell population dynamics.

The in-vitro phase portrait was obtained by seeding mice mammary fibroblasts (F) and bone-marrow derived macrophages (M) at different initial concentrations in co-cultures and following the changes in the cell populations over several days (Fig 3A). This is a measurement of the population level dynamics. In the presence of breast-cancer conditioned medium, F and M cells showed a phase portrait with several distinct fixed points (Fig 3B). Fibroblasts and macrophages supported each other in a fixed point called 'hot fibrosis' - in the sense that both fibroblasts and macrophages coexist. Fibroblasts alone could support themselves in a 'cold fibrosis' fixed point. Macrophages were induced by the cancer conditioned medium to form a macrophage-only fixed point at high macrophage densities.

To test ODSR, we analyzed a MIBI spatial proteomics dataset of human breast cancer samples by (Danenberg et al. 2022). The dataset includes samples from 693 treatment-naive primary breast tumor biopsies totalling 1.12 million cells. The samples are from patients recruited to the METABRIC study (Curtis et al. 2012; Pereira et al. 2016), and include various breast-cancer genotypes and stages, see (Danenberg et al. 2022) for a complete specification. Each sample is approximately a 500um x 500um tissue section, and all samples were imaged on the same slide. Cell types were identified using standard markers and include fibroblasts, macrophages, endothelial cells, adaptive immune cells and epithelial cells. The data includes the KI67 marker.

Since OSDR infers division probability (KI67>threshold) based on the identity of neighboring cells, we first asked whether variation in KI67 is indeed explained by the composition of the cell's neighborhoods in the data. This is not obvious, because this variation may stem from other (unmeasured) factors such as gradients of nutrients, hypoxia or inflammation (Setten et al. 2022). We performed logistic regression with cell counts as features (number of neighboring cells of each type) and KI67 as target (KI67 over threshold, see Methods). We find that cell-counts accurately capture a wide range of division rates (Fig 3C, Fig S2 A,B,C). All fits were very significant (p-value $< 10^{-13}$) (S2C). We conclude that the counts of neighboring cells are strong predictors of division rates.

We next used OSDR to obtain a phase portrait for cancer-associated fibroblasts and macrophages (methods, Fig S3A). We focused on neighborhoods with only these two cell types, along with epithelial and endothelial cells. We excluded neighborhoods with adaptive immune cells since these cells affect the dynamics and were not present in the in vitro experiments (S3I). The samples included a total of 69,874 fibroblasts with 796 divisions (1.1%), and 3,761 macrophages with 79 divisions (2.1%).

The OSDR approach used the division probabilities of fibroblasts (Fig 3D) and macrophages (Fig 3E) as a function of neighborhood composition to yield the phase portrait shown in Fig 3F.

Notably, the reconstructed phase portrait shares most of the key features of the in-vitro portrait (Fig 3B). There is a stable fixed point in which fibroblasts and macrophages support each other, namely a hot fibrosis fixed point. There is a cold fibrosis fixed point with fibroblasts only. There is a third semi stable fixed point with high numbers of macrophages without fibroblasts.

We tested the robustness of the OSDR phase portrait. The fixed-point structure of the phase portrait is robust to resampling of cells and samples (S3B,C). It is also consistently found in a wide range of parameter choices (neighborhood radius, KI67 threshold) (S3 D,E) and death rates (S3F), inclusion of endothelial or tumor cells in the statistical model (S3G), or when considering only patient subgroups with specific cancer stage, tumor size, breast-cancer genotype, patient survival time or type of treatment (S3H).

We conclude that the reconstructed phase portrait captures the salient features of the in-vitro phase portrait. Whereas the in-vitro phase portrait used dynamical measurements of cell populations over days, the reconstructed portrait uses a single snapshot with cell density and division information.

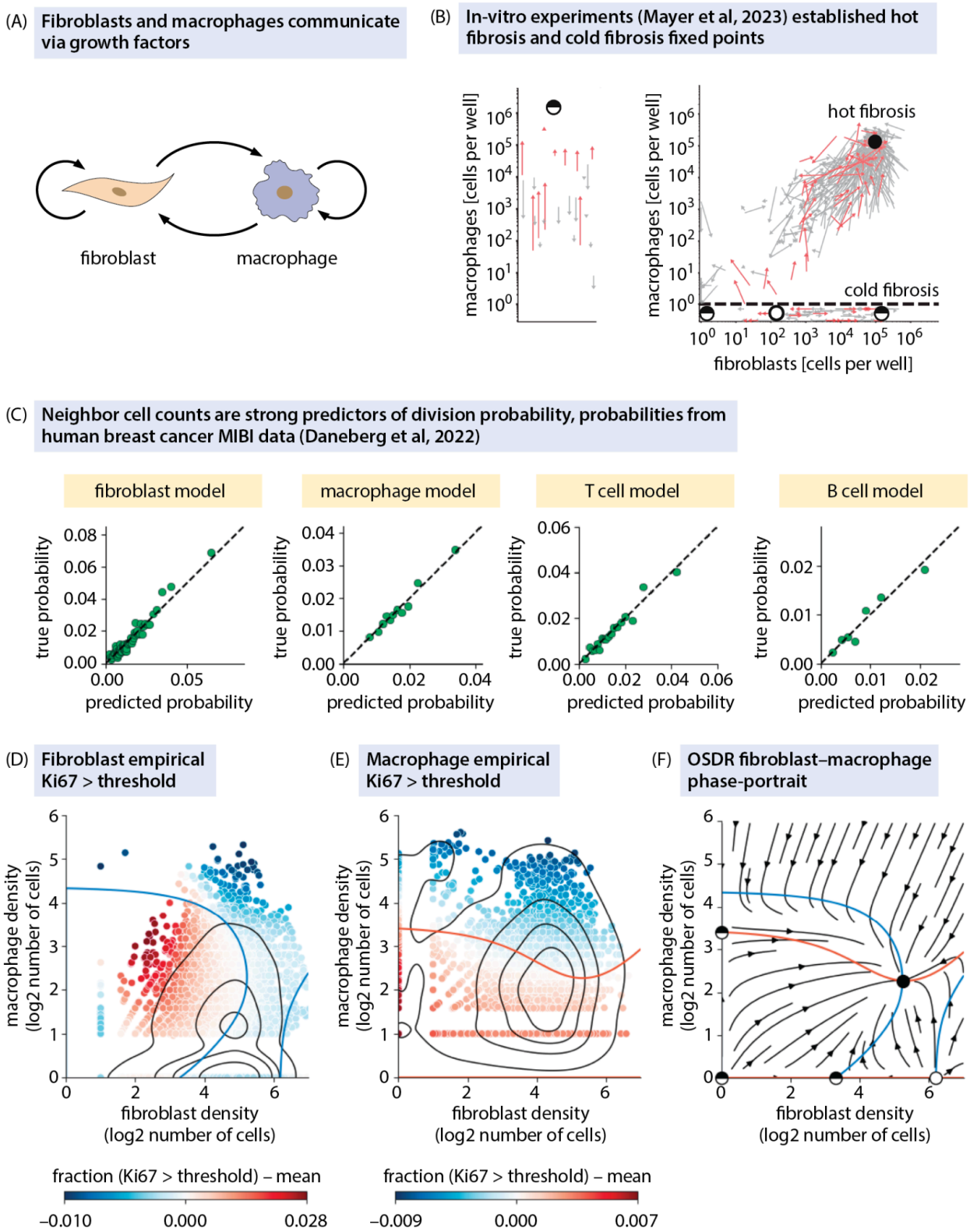

Figure 3: OSDR reconstructs breast-cancer fibroblast and macrophage dynamics in agreement with in-vitro dynamic experiments. A) The breast-cancer microenvironment includes interactions between cancer associated fibroblasts (F) and macrophages (M). B) The in vitro co-culture experiments of Mayer et. al. followed F and M cells in breast cancer conditioned

medium (red arrows) or standard medium (gray arrows), to establish a phase portrait with several fixed points (colored circles). Arrows are changes in cell concentration over 4 days. C) Statistical inference on MIBI data from human breast cancer biopsies (Danenberg et al. 2022) captures a wide range of division probabilities based on cell counts in the neighborhood. Each dot corresponds to a subset of 4000 cells. The x-axis is the model's average predicted probability for a cell and the y-axis is the experimental fraction of dividing cells, as determined by Ki67 > threshold. D) KI67 marker in fibroblasts as a function of neighborhood composition (Methods) from the MIBI breast cancer dataset, colored line separates inferred regions of rising and falling cell numbers (nullcline). Black contours represent density. E) same as D for macrophages. F) OSDR inferred phase portrait for breast-cancer-associated fibroblasts and macrophages. Black and white circles are stable and unstable fixed points respectively.

An excitable pulse-generating circuit of T and B cells in the breast cancer microenvironment

We next considered two other cell types from the breast cancer MIBI dataset, T cells and B cells (Fig 4A). These cells are components of the adaptive immune system which play a major role in the cancer microenvironment, providing protective roles to cancer, and providing therapeutic roles in immune therapy.
We analyzed all neighborhoods which contained at least one T and/or one B cell. This includes a total of 74,006 T cells and 27,643 B cells, with 1,069 and 213 division events respectively. Thus, about 1.4% of the T cells and 0.7% of the B cells showed division events, consistent with previous breast cancer data (Wu et al. 2021).

We estimated the dynamics between T and B cells using OSDR. The inferred phase portrait has a striking feature called excitability. It shows a stable fixed point at zero cells (Fig 4D). However, if T cells are raised above a threshold, they generate a pronounced pulse in which T cells rise, followed by B cells, and then both populations reduce to zero (Fig 4E). This pulse is similar to pulses observed in autoimmune diseases such as relapsing-remitting MS (Lebel et al. 2023).

Similar to the fibroblast-macrophage analysis above, the estimated dynamics were robust to resampling at the level of both cells & patients (S4 B,C) and were consistent under a wide range of death rates, neighborhood sizes and Ki67 thresholds (S4 D,E,F). The dynamics are not confounded by unmodeled cell types, and remain consistent for different patient subgroups (S4G,H).

The pulsatile adaptive immune response in the inferred model is shown in Fig 4E, where T cells rise, followed by B cells that inhibit them, and then both cell populations decline. The model further indicates that after a pulse there is a refractory period, where B cells are still high and T cells are low. During this period, a new pulse cannot be generated due to the inhibitory effects of the B cells (Fig 4F). A new pulse is possible only after the recovery period (Fig 4F).

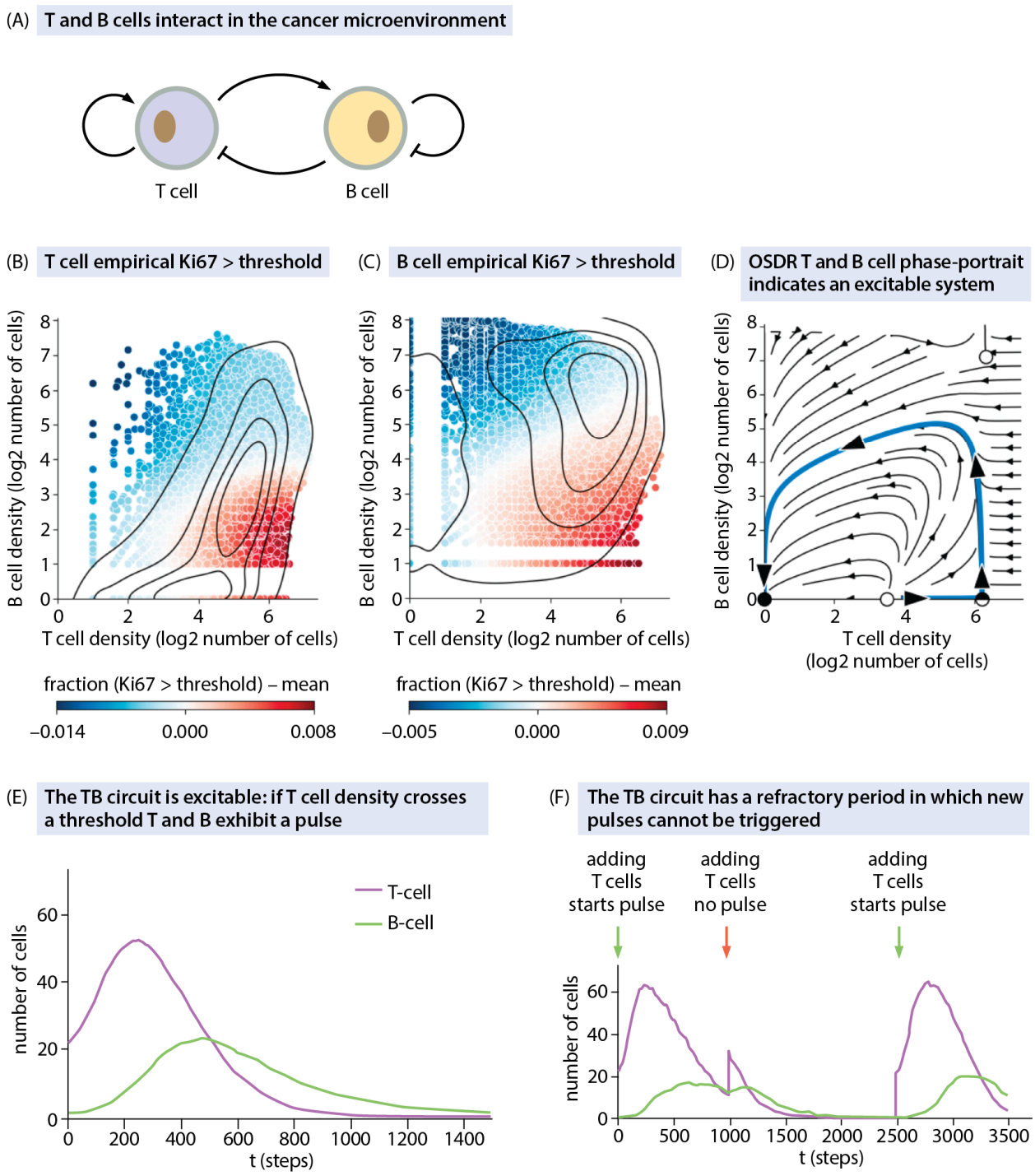

Figure 4: OSDR infers a pulse-generating excitable circuit of T cells and B cells in the breast cancer microenvironment. A) T cells and B cells interact in the tumor microenvironment by secreted cytokines. B) KI67 fraction above threshold from the MIBI dataset of (Danenberg et al. 2022) for B) T cells and C) B cells. D) inferred phase portrait. The blue highlighted trajectory displays a large pulse of adaptive immune cells. E) Simulation of inferred dynamics shows that high enough T cell levels trigger a pulse of T cells followed by B cells . F) Each pulse is followed by a refractory period, as evidenced in simulations in which additional T

cells are added at different times (small vertical arrows). A new pulse is generated only when T cells are introduced after B cells from the previous pulse have declined.

Discussion

We presented the One-Shot Tissue Dynamics Reconstruction (OSDR) approach to discover cell population dynamics from a tissue omics snapshot. OSDR infers division rates as a function of neighborhood cell composition using a cell-cycle marker, and uses this to recover a phase portrait from a biopsy. We used OSDR to analyze spatial proteomics snapshots (MIBI-TOF, Keren et al. 2019) of human breast cancer tumor microenvironment (TME) samples (Danenberg et al. 2022). The estimated fibroblast-macrophage dynamics agree with dynamics measured directly from co-culture experiments in breast cancer conditioned medium, showing a flow towards fixed points of hot and cold fibrosis, as well as self-sustaining macrophages. OSDR also infers the unanticipated possibility of excitable immune pulses in cancer immunosurveillance - T cells and B cells in the breast TME form a pulse-generating circuit, in which T cells rise, followed by inhibitory B cells causing decline of both populations. This suggests a temporal view of the tumor microenvironment with flares of adaptive immunity. Our approach opens the possibility of obtaining cell population dynamics, and hence tissue composition over time, from snapshots of patient biopsies.

The OSDR approach

OSDR can be applied to any experimental modality that provides measurements of cell location, type and division marker levels. Possible modalities range from standard quantitative immunostaining to state-of-the-art spatial transcriptomics and proteomics (Hickey et al. 2022). Our results suggest that OSDR works well with data on the order of thousands of cells and above. It is possible to implement OSDR using different markers for division or death.

OSDR can in principle enable an individualized dynamical model for a given patient based on a single biopsy. The present study used 0.25 mm^2 breast cancer samples, and used hundreds of samples from different patients to obtain large cell numbers. One can obtain the required number of cells from a single biopsy, provided that it is large enough (e.g. multiple sections from a biopsy of a few cubic millimeters totaling an area of 0.2 cm^2). This is feasible using current MIBI technology (Keren et al. 2019). One can then ask how the dynamical behavior of the sample correlates with prognosis and treatment response.

In this study we inferred division probabilities using logistic regression. The features in the regression were based on the number of cells of each type within a fixed radius. We show that these features are strong predictors of a cell's division rate (Fig 3c, S2a). Future studies could develop more sophisticated models for this task in order to utilize additional spatial features, markers and interactions.

Another interesting extension is to incorporate prior knowledge on cell motion within the spatial simulations of OSDR. For movement within the tissue, this could be done by applying a neighborhood-dependent spatial translocation to each cell at every time step. Flux from external

sources can also be modeled by placing new cells in the tissue. As an example, for immune cells this approach could include system-level dynamics involving translocation between tumor, lymph nodes and circulation, as well as local cell-cell interactions.

The cell-circuit models inferred by OSDR could be used to identify key cell-cell interactions that drive the dynamics. These key interactions can suggest interventions to guide tissue composition towards desired states. As inspiration, we note recent studies by (Adler et al. 2020; Miyara et al. 2023; Wang et al. 2023) in which a cell-circuit approach identified the myofibroblast autocrine loop as a critical component in fibrosis. Experimental inhibition of this autocrine loop reduced fibrosis in two mouse models, for myocardial infarction (Miyara 2023) and for NASH liver cirrhosis (Wang 2023). OSDR can propose similar targets for multi-cellular circuits. For example, OSDR predicts that increasing B-cell removal rate will produce higher T-cell levels. This is a nonlinear effect resulting from the negative feedback of B cells on T cells. The effect of such interventions can be modeled by perturbing parameters in the OSDR equations that describe each interaction.

Dynamics of the breast tumor microenvironment

We used OSDR to infer the dynamics of cancer-associated fibroblasts and macrophages in the breast TME. The inferred phase portrait shows that fibroblasts alone (cold fibrosis) or macrophages alone can support themselves. When both cell types are present, their numbers increase to approach a hot fibrosis fixed point where both cell types support each other. These dynamics agree with in-vitro measurements of mouse mammary fibroblasts and BMDM-derived macrophages followed over several days of growth in cancer conditioned medium. The inference of distinct stromal states suggests that the breast TME can harbor hot fibrosis as well as states with only one of the two cell types.

Such hot and cold fibrosis states may be influenced by spatial fields of hypoxia and inflammatory cytokines which can alter the circuit parameters and cause bifurcations between the states, as suggested by recent work on kidney pathology (Setten et al. 2022). Future work can employ spatial omics methods to infer such fields (using markers for hypoxia and inflammatory molecules for example), and to refine the OSDR circuit models. Therapeutically, it would be important to understand the relation of hot and cold fibrosis TME states with outcome.

We also studied the dynamics of T and B cells in the breast TME using OSDR. These adaptive immune cells are crucial for cancer immunosurveillance and for immunotherapy. Most accounts of immune-surveillance of advanced cancer seem to consider it as a steady-state process (Weinberg 2014), in which T cells become exhausted. In contrast to this static picture, we infer a dynamic process - pulsatile T and B dynamics in the TME. The phase portrait suggests that T cells, once they cross a concentration threshold, induce their own proliferation and that of B cells, whereas B cells have an inhibitory effect on the growth of both cell types.

These inferred interactions align with immunological principles. T cells promote their own activation and proliferation, as well as that of B cells, via cytokines such as IL-2, IL-4 & IL-21 (Murphy and Weaver 2016; “Quorum Sensing Allows T Cells to Discriminate between Self and Nonself,” n.d.). Regulatory roles of B cells in the TME are also well-documented (Wolf H.

Fridman et al. 2022; Engelhard et al. 2021; Laumont et al. 2022; Murakami et al. 2019; Cai et al. 2016; Shalapour et al. 2017; 2015; Yuen, Demissie, and Pillai 2016). Such regulatory B cell effects have been observed in human breast cancers and associated with poor prognosis (Ishigami et al. 2019). Regulatory B-cell activity is, in part, induced by cytokines released by T-cells such as IL-21 (Yoshizaki et al. 2012).

Together, these interactions can generate pulses of activity when activated T cells cross a concentration threshold. Such pulses or flare-ups are observed in autoimmune diseases (Lebel et al. 2023; Oleinika, Mauri, and Salama 2019; Yoshizaki et al. 2012). A rise and fall of adaptive immune cells with time is also a hallmark of pathogen response (Murphy and Weaver 2016). The inferred timescale of the pulses in the present study, on the order of weeks, roughly agrees with the flare duration in the autoimmune and pathogen contexts.

The T and B cell pulsatile circuit also predicts a refractory period after each pulse. During the refractory period, a new pulse of T cells cannot be started due to high levels of inhibitory B cells. Only after B cells have declined can a new pulse be generated. This refractory period is similar conceptually to that found in neuronal action potentials, also an excitable system (Izhikevich and FitzHugh 2006).

A T cell refractory period can potentially bear on the timing of cancer immunotherapy. It may be beneficial to time immunotherapy doses so that they don't overlap the refractory period of the previous dose. Reduction of dose frequency may reduce immune-related adverse events, which currently cause treatment termination in up to 30% of patients (Martins et al. 2019). More generally, the existence of such T and B cell pulses can conceptually add a temporal dimension to research on the TME, with flares of adaptive activity.

Such adaptive immune flares can also address the pleiotropic effects of B cells observed in tumors. On the one hand depleting B cells in mice improved outcome in several cancer models (Qin et al. 1998; Shah et al. 2005; Brodt and Gordon 1978; Barbera-Guillem et al. 2000; Lee-Chang et al. 2013). On the other, B cells in human tumors (primarily in tertiary lymphoid structures) are associated with improved prognosis in many cancers (Laumont et al. 2022; Wolf H. Fridman et al. 2022, 20; Wolf Herman Fridman et al. 2020). One possible explanation is that observing high B cell counts in tumors indicates that T cells have crossed a sufficiently high level for a flare of immune attack; depleting B cells may reduce their inhibition and sustain the T cell pulses for longer durations.

Limitations

The dynamics estimated by OSDR are less reliable in areas of state space (cell-concentration space) with sparse data. We suggest interpreting phase-portraits together with the state-space density plots of the underlying samples and being wary of extrapolation. The current implementation approximates the death rate as a constant rate that maintains overall homeostasis. Establishing reliable markers for cell death rate may improve model estimates in cases where regulation of death rate by neighboring cells dominates proliferation. The OSDR model as currently implemented also assumes that cell migration and transdifferentiation is a negligible source of change for cell populations; these effects can be evaluated using the

current OSDR simulation by including flux terms and modes of cell movement. Direct measurement of TME dynamics *in vivo*, for example by intravital microscopy (Entenberg, Oktay, and Condeelis 2023), could provide a rigorous test of OSDR predictions.

Summary

We presented the OSDR approach to infer cell population dynamics in a tissue based on spatial snapshots from biopsies. We then showed the utility of OSDR in understanding the breast cancer microenvironment. We validated OSDR by comparison to macrophage and fibroblast dynamics in vitro, and used OSDR to infer T and B cell pulses in the breast tumor microenvironment, adding a temporal dimension to cancer immunosurveillance. OSDR could help discover cell population dynamics in other tissues and conditions based on biopsies - including developmental processes and pathological processes such as autoimmunity or fibrosis. Tissue dynamics can unlock mechanisms of pathology and rationalize the impact of treatment aimed at changing tissue composition to reach therapeutic goals.

Methods

The number of cells of a given type in a tissue section can change by division or death, moving in or out of the section (flux) or transdifferentiation (Weinreb et al. 2018). If we restrict ourselves to modeling cell-types who do not transdifferentiate at appreciable rates such as T-cells and Macrophages and analyze tissues in which flux is negligible relative to rates of death or division or add flux terms post-hoc, we remain with the following equation for the rate of change of a population of cells of type i:

$$\frac{dX_i}{dt} = \frac{\#divisions}{dt} - \frac{\#\ deaths}{dt}$$

OSDR aims to transition from static observations of cell division or death in a tissue into rates. The key insight is as follows - if we obtain a marker for cell division (or death), and in each cell division the marker remains above a defined threshold for a time period dt, then all observed divisions occurred within the last dt hours. Thus:

$$\frac{dX_i}{dt} = \frac{\#divisions}{time\ a\ division\ remains\ observable} - \frac{\#\ deaths}{time\ a\ death\ remains\ observable}$$

A cell's rate of division or death is influenced by the signals that it receives from its environment, its access to nutrients, its genetics and factors such as physical contact with other cells. We call this complete set of factors the cell's "neighborhood". This definition sets an ideal, and we denote the particular set of features used to approximate this ideal as $N(x)$, where x is some cell in the tissue.

If we consider cells with identical neighborhoods, a fraction of them will be dividing. This fraction is higher if the neighborhood induces a high rate of division and vice versa. We thus view the observations of division or death as random events whose probabilities are determined by the cell's neighborhood. Thus, for cell x of type i, the distribution of the observation $O_{i,t}(x)$ of a division or death event is modeled as follows:

$$O_{i,t}(x) = \begin{cases} +1/dt^{+} & \text{with probability:} \quad \mathrm{p}_i^{+}(N(x)) \\ -1/dt^{-} & \qquad\qquad\qquad\quad \mathrm{p}_i^{-}(N(x)) \\ 0 & \qquad\qquad\qquad\quad \text{remaining} \end{cases}$$

Where p_i^+, p_i^- are the statistical inference-models for division or death, and dt^+, dt^- are the durations of observed division or death markers respectively. In this study, dt^+ is defined as 1 time unit (roughly a few hours, see (Uxa et al. 2021)), and the approximation of the death rate as the mean division rate is defined using the same time units. Thus, in this implementation $dt^+=dt^-=1$. We divide by the durations so that we get the following simple formula for the (stochastic) change in the number of cells in each timestep:

$$\frac{dX_i}{dt} = \sum_{x \in X_i} O_{i,t}(x)$$

Tissues are heterogenous, and the diverse cellular compositions in different regions result in various directions of change. In order to analyze the change at a certain *state*, rather than the change in complete tissues, we compute the expected change with respect to an initial condition where all cells have the same neighborhood (this can be seen as placing a number of cells at the exact same location, in a setting without migration):

$$\begin{aligned} E_x[\frac{dX_i}{dt}] &= E[\sum_{x \in X_i} O_{i,t}(x)] \\ &= \#X_i[p_i^{+1}(N(x)) - p_i^{-1}(N(x))] \end{aligned}$$

In this study, we use as features the number of neighboring cells of each type within a certain predefined radius. The choice of these features is based on a separation of timescales argument - the half-life of typical signaling proteins (by endocytosis or degradation) is much shorter than the rates of cell division and death ("Endocytosis as a Stabilizing Mechanism for Tissue Homeostasis | PNAS," n.d.). As a result, the signaling proteins reach a steady state before the density of cells changes considerably. This steady-state is then proportional to the density of secreting cells. The neighborhoods can thus be represented as a vector of cell densities:

$$X := \begin{bmatrix} X_1 \\ X_2 \\ \vdots \\ X_k \end{bmatrix}$$

As a result, we can interpret the models as components of a set of ordinary differential equations defined over a state-space of cell densities:

$$\dot{X} := \begin{bmatrix} E[\dot{X}_1] \\ E[\dot{X}_2] \\ \vdots \\ E[\dot{X}_k] \end{bmatrix} = \begin{bmatrix} X_1[p_1^{+1}(X) - p_1^{-1}(X)] \\ X_2[p_2^{+1}(X) - p_2^{-1}(X)] \\ \vdots \\ X_k[p_k^{+1}(X) - p_k^{-1}(X)] \end{bmatrix} = f(X)$$

Note that OSDR is inference-model-agnostic, while we employ logistic regression here, other statistical inference models can be adopted within this framework. In addition, this approach can be applied to data acquired by any technology that enables classification and spatial localization of discrete cells, together with robust measurement of a set of markers for division (and possibly death).

Model Inference Algorithm:

Input:

Cell level annotations: $(B_i, T_i, \vec{x}_i, O_i)$ for cell $i = 1,\dots N$

- B_i - an ID for the biopsy sample cell i came from. B_i is used to formalize that a cell can only influence cells from the same tissue.
- $T_i \in T$ - cell type for cell i (e.g T_i = "Fibroblast"), and let T be the set of types.
- For any $t \in T$ let n_t be the total number of cells of type t. We shall also assume some order on the cells of type t, such that: $t[j] = i$ for any index $j \in \{1,\dots n_t\}$, and the original index $i \in \{1,\dots, N\}$.
- $\vec{x}_i \in R^2$- 2D spatial coordinates for cell i.
- $O_i \in \{0, 1\}$ - binary observation of division

Algorithm:

For each cell-type $t \in T$, :

1. Compute a table of features $X_t \in R^{n_t x T}$.

$$X_t[i, t'] := \sum_{j=1}^{N} 1[B_j = B_{t[i]},\ T_j = t',\ ||\vec{x}_{t[i]} - \vec{x}_j|| < r]$$

   Here $t[i]$ is the original index of the i'th cell of type t. The value at row i and column t', is a count of all cells that came from the same tissue as cell $t[i]$, that have type t' and are within a distance r.
   Row i in X_t is our representation for the "neighborhood" of cell $t[i]$ - the counts of all cell-types in its proximity. Denote this vector by $N(t[i]) := X_{T_i}[i,:]$
2. Perform feature transformations on X_t, such as adding interaction terms. (transformations are selected through a separate process of cross validation)
3. Define the binary labels $y_t \in \{0, 1\}^{n_t}$:

$$y_t[i] = O_{t[i]}$$

4. Fit a multivariate logistic regression model p^+_t for division rate based on the features and labels X_t, y_t.
5. Define death rate:
   $p^-_t = mean(y_t)$

Output:

$$\left((p^{+}_{t}, p^{-}_{t}) : t \in T\right)$$

Ki67 Thresholds:

We used previous data to establish a KI67 threshold for cell division events. Uxa et. al, 2021 demonstrated that Ki67 levels peak towards the G2/M phase of the cell cycle, with preserved kinetics (up to scale) across two human and one mouse cell line. We adjust Ki67 levels to correct for different scaling and division rates between cell lines (S1a,b) by selecting Ki67 values above a noise threshold T_n, subtracting T_n and dividing by the Ki67 standard deviation. We choose $T_n = 0.5$ mean isotopic counts because this is the typical magnitude of experimental noise in this dataset (S1c). This produces distributions with similar shape (S1d) in accordance with the cell line results of Uxa et al. We define a cell division by the normalized Ki67 above a division threshold T_d. Example fractions of dividing cells are provided in S1e. The resulting model estimates are robust to T_d values between 0 and 1 on this adjusted scale (S1D)

Choice of spatial proteomics technology

Out of the currently available spatial-omics technologies, multiplexed protein imaging was the most suitable for our setting. Current barcode-based spatial-transcriptomics (Tirado-Lee, n.d.) aggregate cells in spots of 55 micron diameter so they don't associate transcript levels with single discrete cells. Also, because the distance between spot centers is 100 micrometers, if we place a cell in the center of a spot, we measure less than 1/9 of the area immediately surrounding it (area of a circle of radius 27.5 micrometers, within another of radius 72.5). Fluorescent based approaches like MERFISH allow modeling single cells but they recover a small fraction of every transcript in the tissue. This is a barrier for basing the analysis on levels of a single transcript - Ki67. MIBI-TOF provides measurements within well-defined cells, reliable measurement of Ki67 and, in terms of cost, makes datasets in the order of magnitude of hundreds of thousands of cells feasible. Classical staining methods should also be feasible for analyzing specific pairs of cells. For example, for analyzing fibroblasts and macrophages, we could use 4 markers: fibroblast and macrophage markers, a cell nucleus marker, and Ki67.

Enforcing Maximal Density:

We assume there cannot be a net positive flux at the maximal observed density of a cell type. We apply a correction in the form of:

$$p_i^{correction} = c_i \cdot d_i^{n}$$

Where d_i is the density of cell i, and the power n controls the steepness - high n implies the correction applies primarily to higher densities (S1F). The constant term c_i is defined as the minimal correction ensuring non-positive flux at max density (D_i). We compute division minus death rates at the maximal density of one cell, over all possible values of the second cell:

$$c_i \cdot D^n_i = \max_{N(x):d_i=D_i} p^+_i(N(x)) - p^-_i(N(x))$$

In practice, the state-space region near maximal density for both cell types is unpopulated by cells, so we use values up to the 95% quantile density for each type. This is more robust to artifacts due to extrapolation in areas with minimal data and produces smaller corrections (S1G). For the FM model this correction is trivial because the estimated net flux is negative at high densities, for the TB model the correction applies only to T-cells (S1G,H).

Simulation of dynamical models:

We simulate spatial data based on a known dynamical model (i.e functions p^+ and p^-) using the following procedure:

1. Sample a random initial number of cells for each cell type.
2. Sample a random spatial position in the tissue for each cell.
3. For n steps:
    a. Compute for each cell the probability of division or death based on its current neighborhood.
    b. Sample an event of division, death or none based on the computed probabilities
    c. Remove dead cells and place a new cell next to each dividing cell (here, location of new cells is sampled uniformly within the neighborhood. It's straightforward to incorporate knowledge about cell motility at this stage, if available).

This produces a tissue section whose density and spatial distribution is biased by the dynamics, as we assume is the case for real tissues. We repeat the procedure 100 times from various initial densities and sample with replacement 50K cells evenly from all tissues. From this pool we then sample 1K, 5K, 10K or 25K cells for the model fits.

Because empirical distributions in our data had tails towards lower cell-densities, we sampled the initial cell densities from a beta distribution biased towards lower densities (parameters 2,4 scaled to a maximal value of 7). Model parameters were selected to produce division rates in ranges that resemble real data (mostly within 1%-6%). The fraction of divisions was approximately 2% for all models. We selected the number of simulation time steps as that required to produce distributions qualitatively similar to real data.

To evaluate model fits we tested whether the correct location and type of stable or semi-stable fixed points were recovered. To account for discretization error, if a stable point on an axis was recovered, and an unstable point was located within 1 cell from that point, we count it as a semi-stable. Such a point effectively has no basin of attraction. The same precaution should apply to interpretation of model fits in general.

For a detailed analysis of the simulations of each ground truth model see S2C,D,E,F,G.

Plotting Ki67 levels as a function of neighborhood composition:

Figures 3D,E and 4B,C display the measured Ki67 > Threshold as a function of neighborhood composition. To transform the cell-level binary division events into rates, we compute a local average and subtract the mean division rate. For the local average, we used a gaussian smoothing kernel over the cell-density state space, providing a non-parametric plot of the division rate. The kernel's gamma parameter controls the degree of smoothing. We plot a value of gamma that produces contours of similar complexity as those of the estimated parametric models.

<u>Estimating magnitude of error due to unmodeled terms such as cell migration:</u>

We apply the mass continuity equation to the state-space of *neighborhoods*. Each neighborhood is analogous to a particle moving through a space whose coordinates are defined by the densities of each cell type. For example, x, y could be the density of fibroblasts and macrophages. The velocity through this space is determined by the rate of change in each cell type. This velocity is the sum of $\vec{v}\ (x, y)$, the division minus removal rates we estimate from data, and $\vec{u}(x, y)$, which includes unmodeled terms such as cell migration and differentiation from stem cells.

$$\frac{\partial \rho}{\partial t} = -\vec{\nabla}\,[\rho \cdot (\vec{v} + \vec{u})]$$

<u>Notation:</u>

$\rho(x, y)$ - density of neighborhoods at location x, y

$\vec{v}(x, y) + \vec{u}(x, y)$ - velocity of a neighborhood in the state-space.

$\vec{v}\ (x, y)$ - division minus death rate field, estimated from data.

$\vec{u}\ (x, y)$ - velocity field due to unmodeled terms such as cell migration (will be estimated now)

For our large sample of patients, we assume that sampling the same tumors within a few days would produce approximately the same distribution. This implies that $\frac{\partial \rho}{\partial t} \approx 0$. Thus:

$$0 = -\vec{\nabla}\,[\rho \cdot (\vec{v} + \vec{u})] = -\vec{\nabla}\,(\rho \cdot \vec{v}) - \vec{\nabla}\,(\rho \cdot \vec{u})$$

So we can compute the divergence of the cell migration field:

$$\vec{\nabla}\,(\rho \cdot \vec{u}) = -\vec{\nabla}\,(\rho \cdot \vec{v})$$

This is sufficient for identifying the regions in state-space where cell migration would produce a net increase or decrease in density. Practically, we estimate ρ by computing the location of each patient's tissue in the state-space followed by kernel density estimation. We then numerically

evaluate the divergence $\vec{\nabla}(\rho \cdot \vec{v})$. By plotting $\vec{\nabla}(\rho \cdot \vec{v})$ we get the negative divergence of the migration field. This produces the sources (negative $\vec{\nabla}(\rho \cdot \vec{v})$) and sinks (positive $\vec{\nabla}(\rho \cdot \vec{v})$) of the cell migration field. Note, for interpretability we divide the rates by the maximal ρ so that units are in [fractions of maximal density / Δt].

For the Fibroblast-Macrophage model the residual field produces a net effect that disperses cells from the peak density. This form of error could be explained by unmodeled stochasticity, so we model the dynamics using a Fokker-Plack equation. Let X be the location of a neighborhood in state-space, then it's velocity is given by the following stochastic differential equation:

$$\frac{dX}{dt} = (\vec{v} + \vec{u}) + \sqrt{2D} \cdot \epsilon$$

Where ϵ is a standard Brownian motion. The Fokker-Planck equation states that the density of neighborhoods changes according to:

$$\frac{\partial \rho}{\partial t} = -\nabla[\rho \cdot (\vec{v} + \vec{u})] + D\nabla^2(\rho)$$

Using the same argument as before, we assume $\frac{\partial \rho}{\partial t} = 0$, so we model the cell migration field as:

$$\nabla(\rho \cdot \vec{u}) = -\nabla(\rho \cdot \vec{v}) + D\nabla^2(\rho)$$

We select D that best explains the error of the deterministic model using ordinary least squares regression with D as a single parameter:

$$D = \arg\min_D ||\nabla(\rho \cdot \vec{u}) - D\nabla^2(\rho)||_2 = \arg\min_D ||\nabla(\rho \cdot \vec{v}) - D\nabla^2(\rho)||_2$$

Supplementary:

Supplementary 1 - Method

Supplementary 1a - Empirical Ki67 distributions have right tails

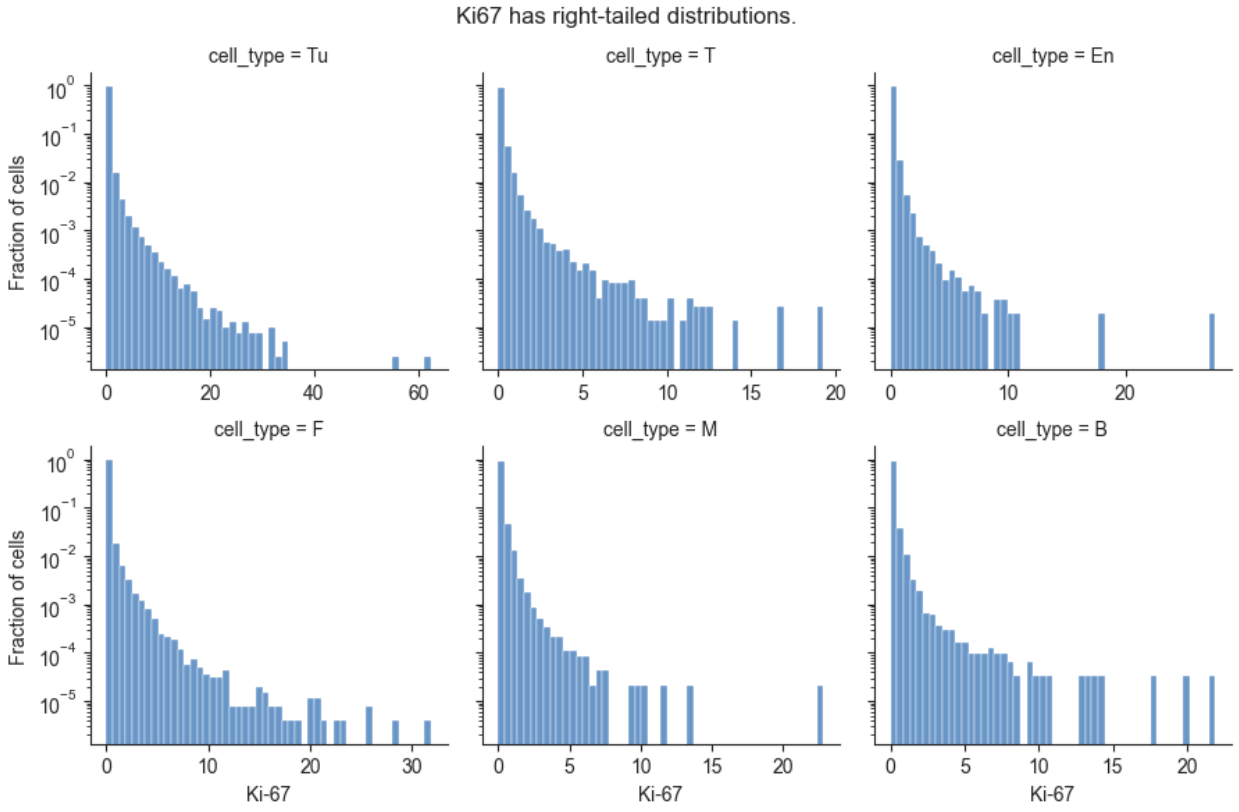

Supplementary 1b - Varying fractions of cell with Ki67 > 0 or Ki67 > noise among different cell types

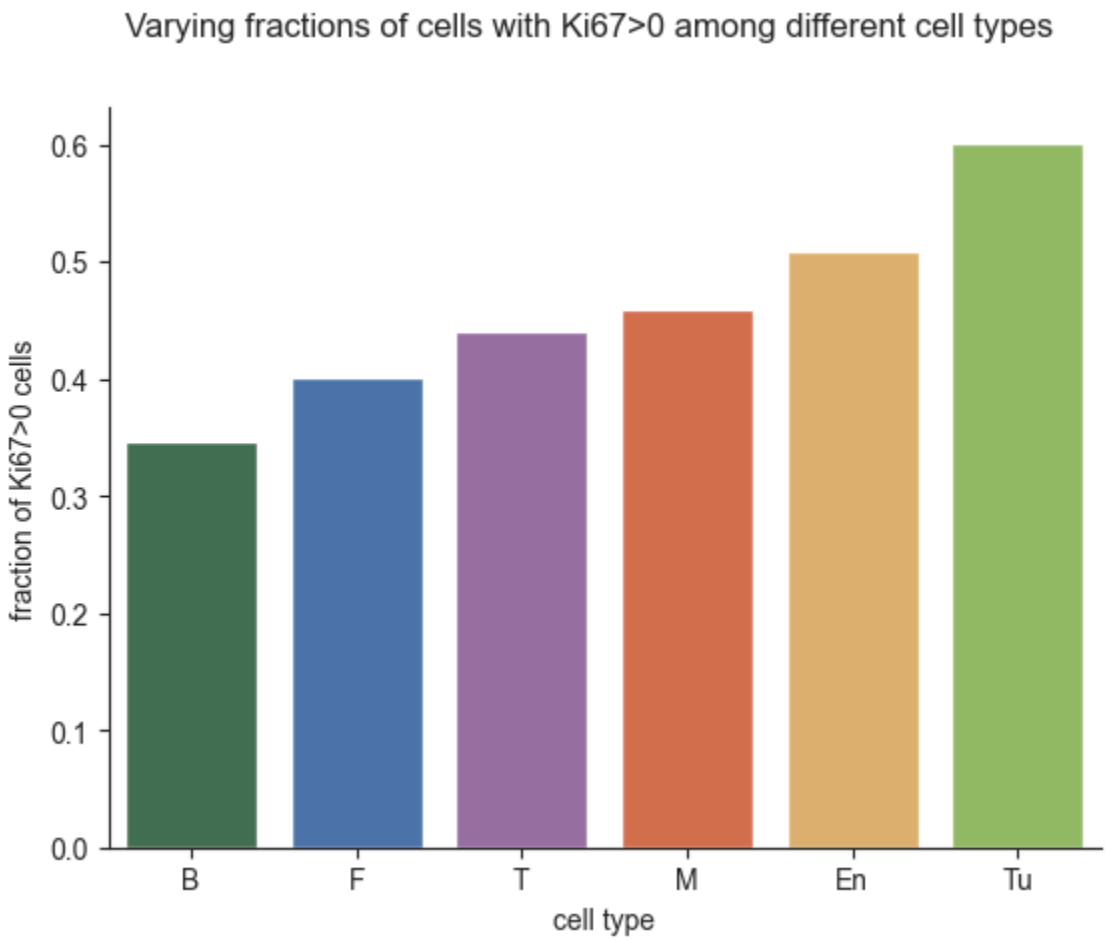
Varying fractions of cells with Ki67>0 among different cell types
fraction of Ki67>0 cells
0.0
0.1
0.2
0.3
0.4
0.5
0.6
B
F
T
M
En
Tu
cell type

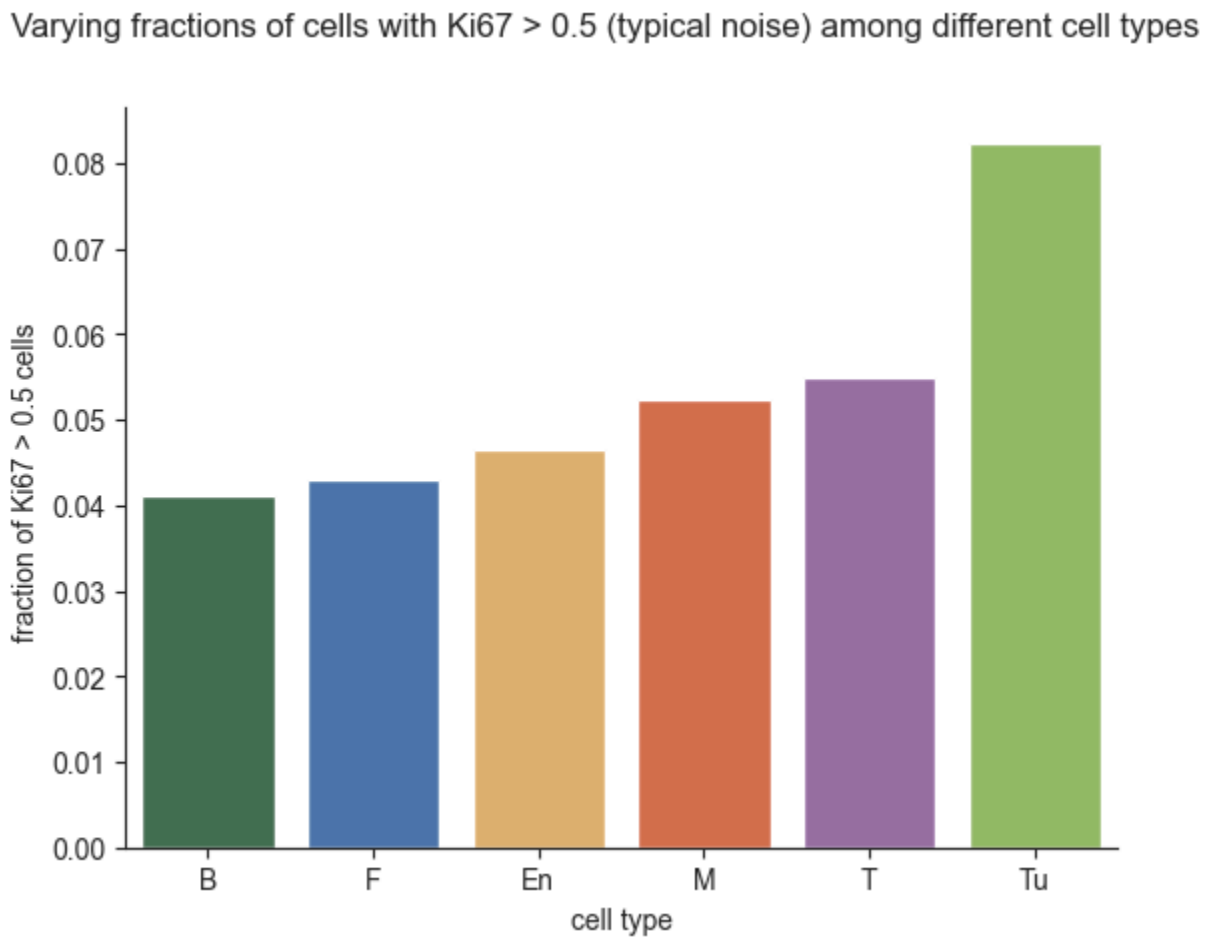

Supplementary 1c - Typical magnitude of noise of MIBI protein markers is 0.5

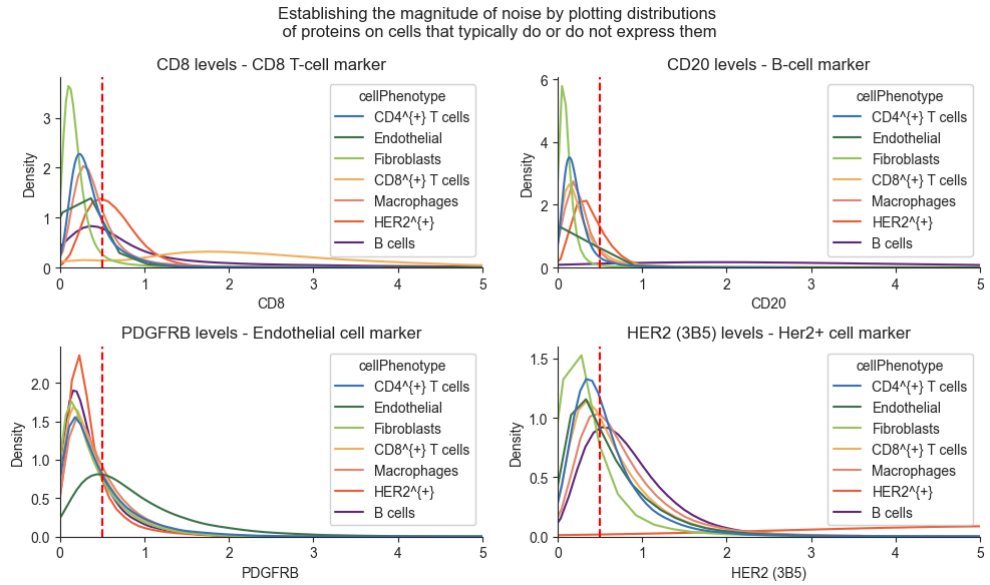

Supplementary 1d - Adjusted Ki67 distributions have similar shapes

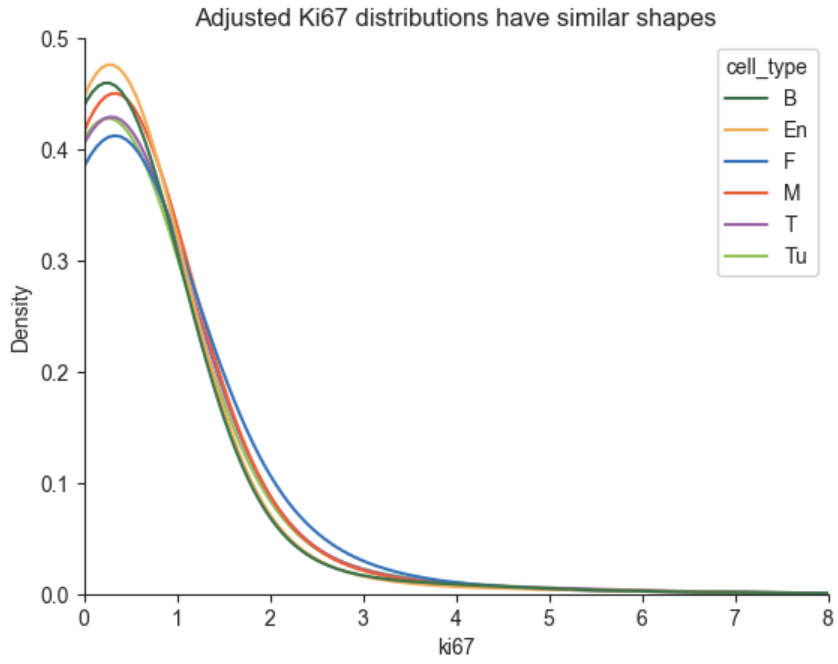

Supplementary 1e - Fraction of dividing cells (adjusted Ki67 > threshold of 0.5)

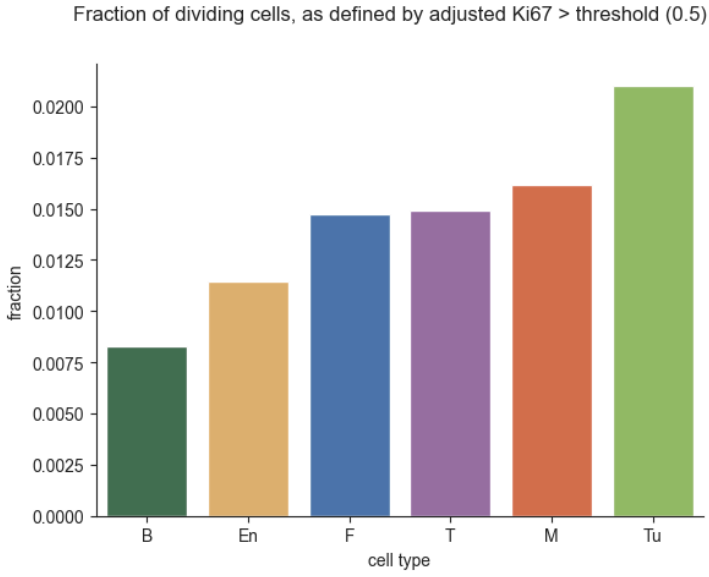

Supplementary 1f - maximal density correction power-term n determines steepness:

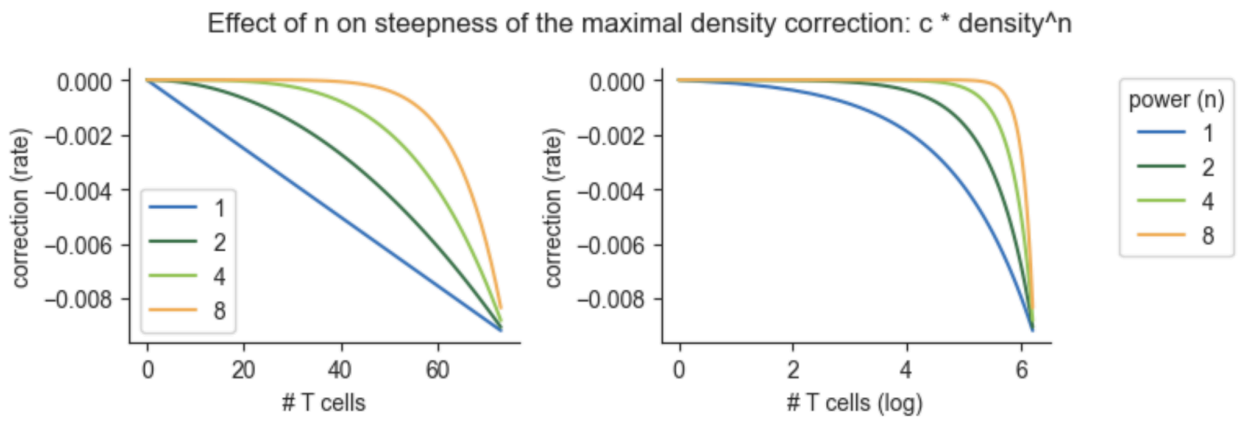

Note how a power of 1 dominates the dynamics over the entire phase portrait. Also note the marginal influence of additional powers. We preferred a higher power (8) as it preserves as much of the original phase portrait as possible.

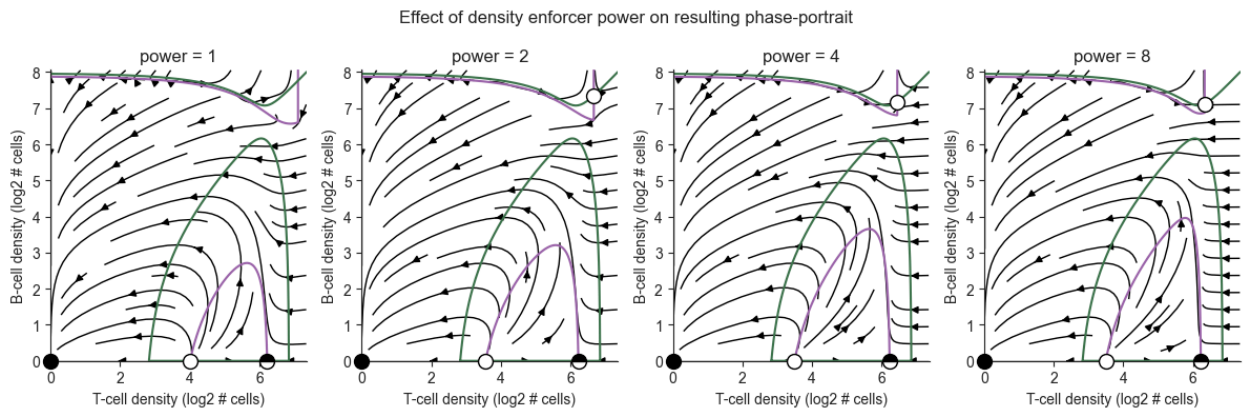

Supplementary 1g - maximal density correction in the TB model - separating the original and correction components of the phase portrait (power n=8):

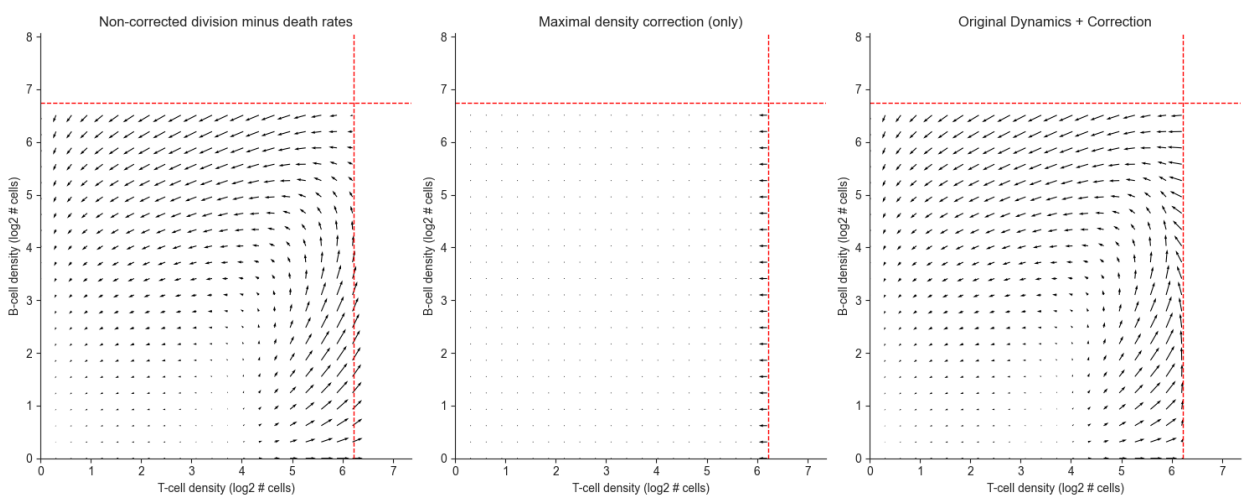

Supplementary 2 - Model Estimation

Supplementary 2a. Calibration plots for all cell types, compared with calibration on same data with permuted divisions

Each green dot aggregates 4000 cells, red lines are min & max true probabilities. The x-axis location of a dot is the model's average predicted probability for a cell in that subset. The y-axis location is determined by the fraction of cells that are truly dividing, as determined by a Ki67 measurement > threshold.

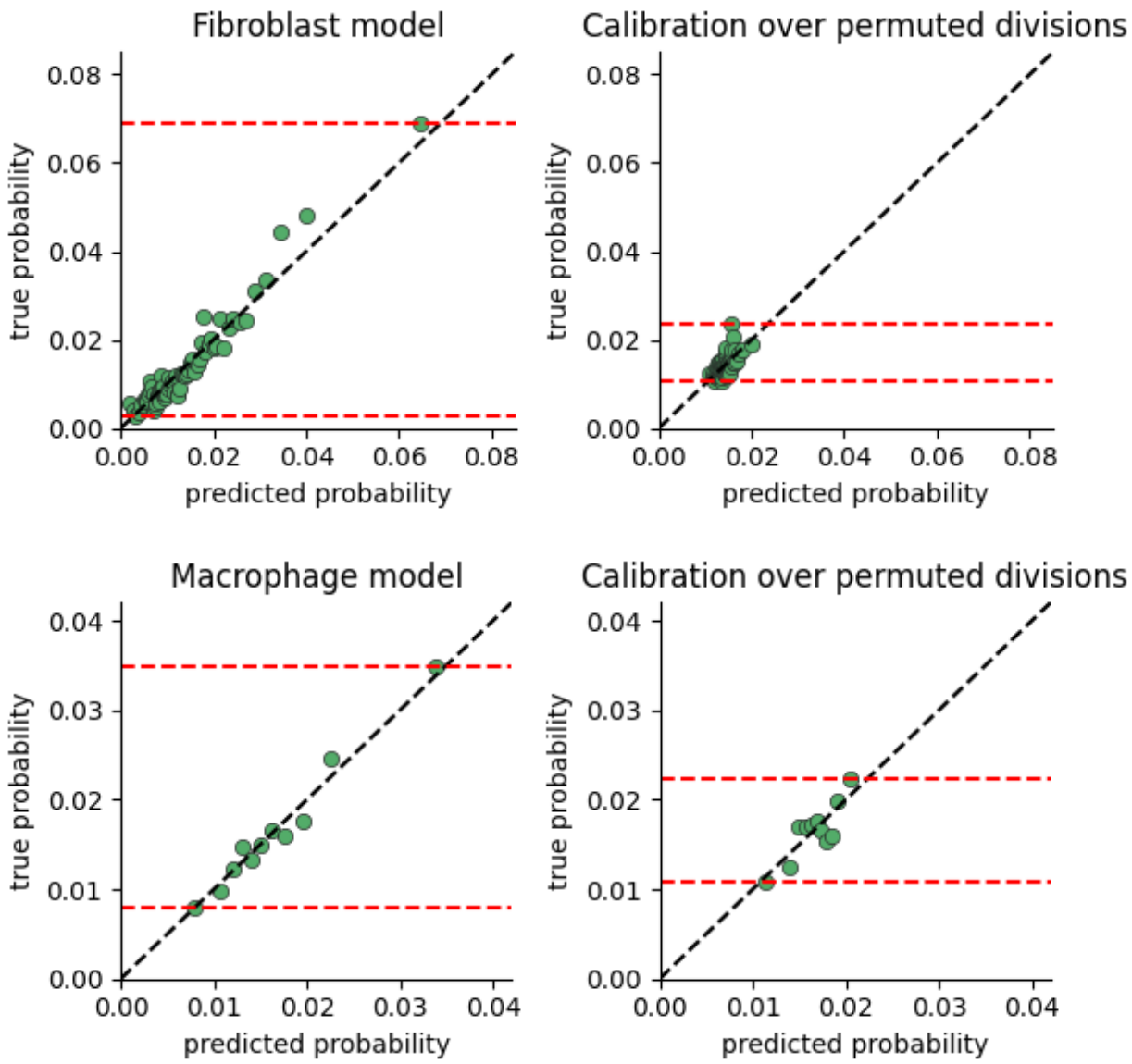

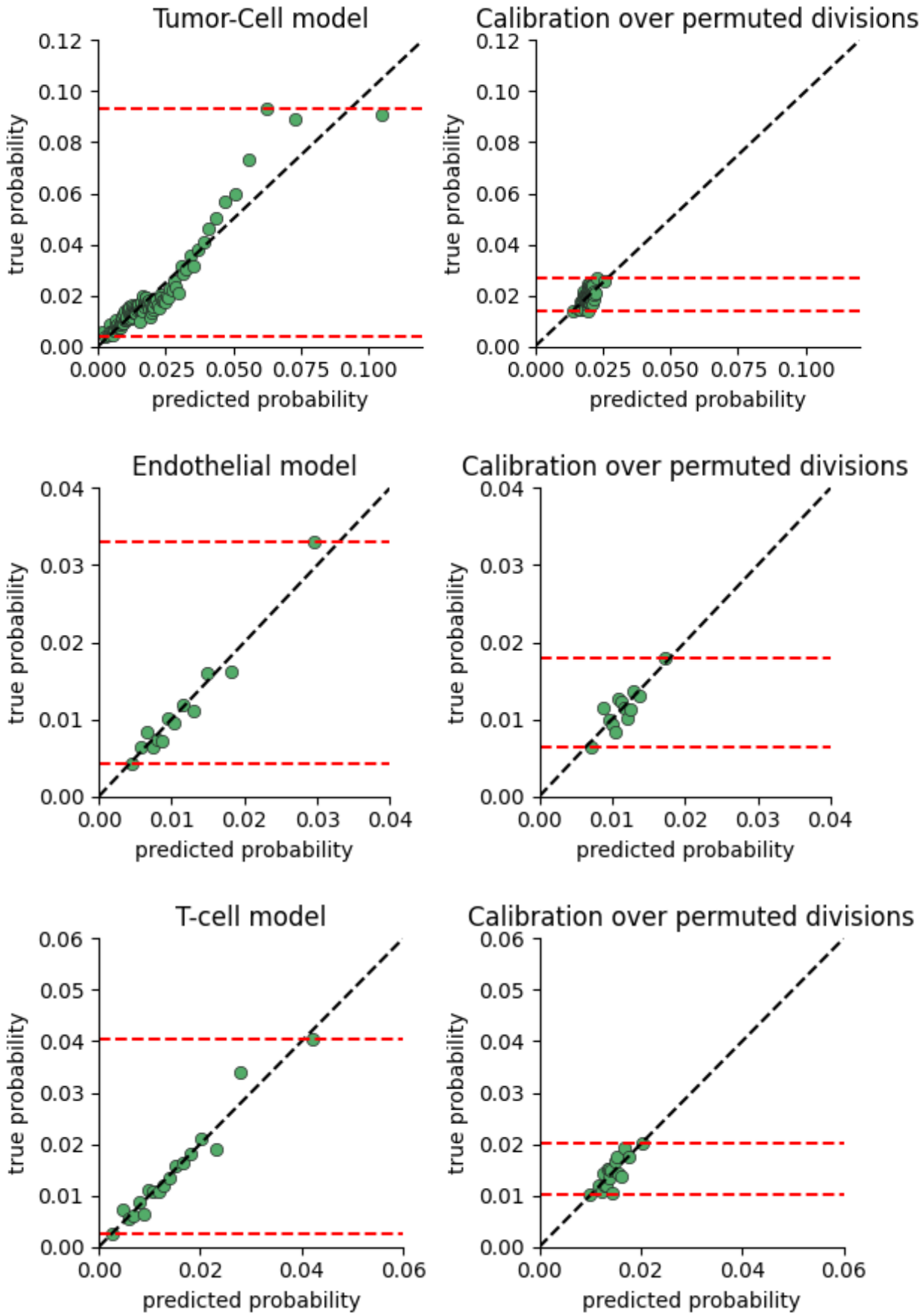
Tumor-Cell model
Calibration over permuted divisions
Endothelial model
Calibration over permuted divisions
T-cell model
Calibration over permuted divisions
true probability
predicted probability
0.00
0.02
0.04
0.06
0.08
0.10
0.12
0.000
0.025
0.050
0.075
0.100
0.01
0.03
0.05

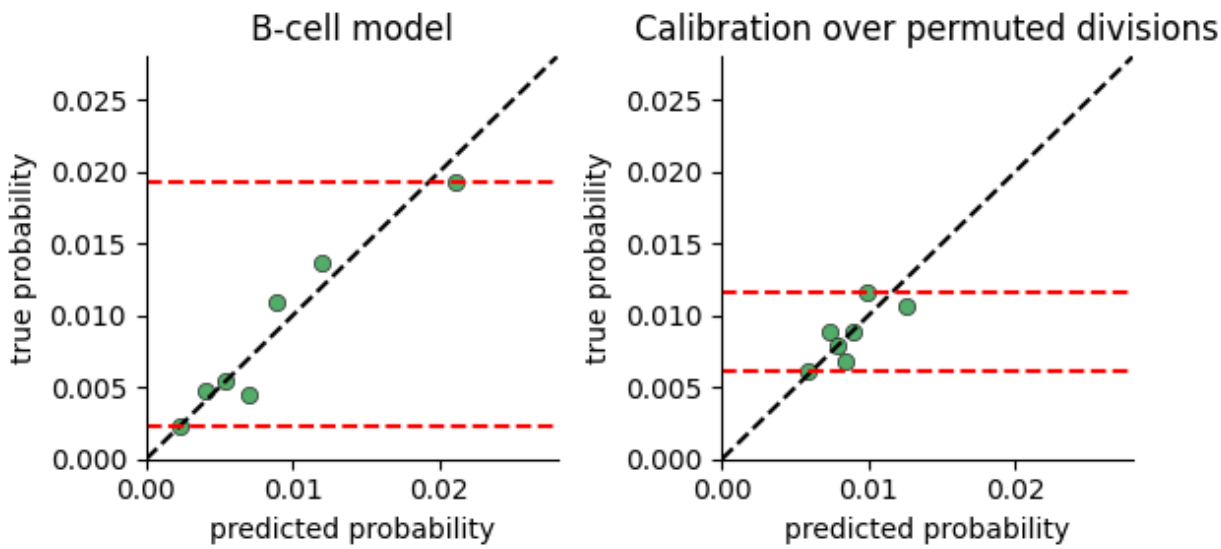

Supplementary 2b. Example model fit and features in the fibroblast division rate model:

The variable for each cell type is log(1 + cell count). We include up to 2nd order interactions (i.e all 2nd order polynomial terms are included)

Dep. Variable:	division	No. Observations:	258596
Model:	Logit	Df Residuals:	258568
Method:	MLE	Df Model:	27
Date:	Mon, 15 Apr 2024	Pseudo R-squ.:	0.04140
Time:	16:12:14	Log-Likelihood:	-18523.
converged:	True	LL-Null:	-19324.
Covariance Type:	nonrobust	LLR p-value:	0.000

	coef	std err	z	P>|z|	[0.025	0.975]
1	-1.8109	0.272	-6.647	0.000	-2.345	-1.277
F	-1.5678	0.106	-14.759	0.000	-1.776	-1.360
M	1.5237	0.100	15.283	0.000	1.328	1.719
Tu	0.3658	0.057	6.435	0.000	0.254	0.477
En	-0.3789	0.085	-4.439	0.000	-0.546	-0.212
T	-0.6910	0.091	-7.580	0.000	-0.870	-0.512
B	0.5771	0.121	4.755	0.000	0.339	0.815

F^2	0.1464	0.012	12.307	0.000	0.123	0.170
F M	-0.1193	0.016	-7.315	0.000	-0.151	-0.087
F Tu	0.0264	0.009	3.050	0.002	0.009	0.043
F En	0.0880	0.015	5.997	0.000	0.059	0.117
F T	0.0638	0.014	4.457	0.000	0.036	0.092
F B	-0.0130	0.018	-0.707	0.480	-0.049	0.023
M^2	-0.1260	0.012	-10.464	0.000	-0.150	-0.102
M Tu	-0.0576	0.009	-6.345	0.000	-0.075	-0.040
M En	-0.0580	0.013	-4.604	0.000	-0.083	-0.033
M T	0.0274	0.015	1.841	0.066	-0.002	0.057
M B	-0.0422	0.017	-2.517	0.012	-0.075	-0.009
Tu^2	-0.0455	0.005	-9.052	0.000	-0.055	-0.036
Tu En	-0.0270	0.007	-3.636	0.000	-0.042	-0.012
Tu T	0.0344	0.008	4.108	0.000	0.018	0.051
Tu B	-0.0208	0.010	-2.113	0.035	-0.040	-0.002
En^2	-0.0189	0.009	-2.035	0.042	-0.037	-0.001
En T	0.0699	0.011	6.313	0.000	0.048	0.092
En B	-0.0325	0.013	-2.576	0.010	-0.057	-0.008
T^2	0.0400	0.010	4.187	0.000	0.021	0.059
T B	0.0028	0.016	0.173	0.862	-0.029	0.035
B^2	-0.0768	0.011	-7.090	0.000	-0.098	-0.056

Supplementary 2c. Logistic regression model log-likelihood ratio p-values

cell_type	LLR p-value
F	0.000000e+00
M	1.390545e-15
Tu	0.000000e+00
En	1.823899e-24
T	4.976010e-72
B	4.747885e-14

Supplementary 2D. 2-cell simulations - overview

In sections 2D,E,F,G we present results from simulations used to test feasibility of the OSDR approach and the required sample size for recovering various aspects of a ground truth model, including location and type of fixed points. The four models considered exhibit the four possible organizations of stable fixed points for two cells, such that each cell is stable either in the presence of the other cell or not.

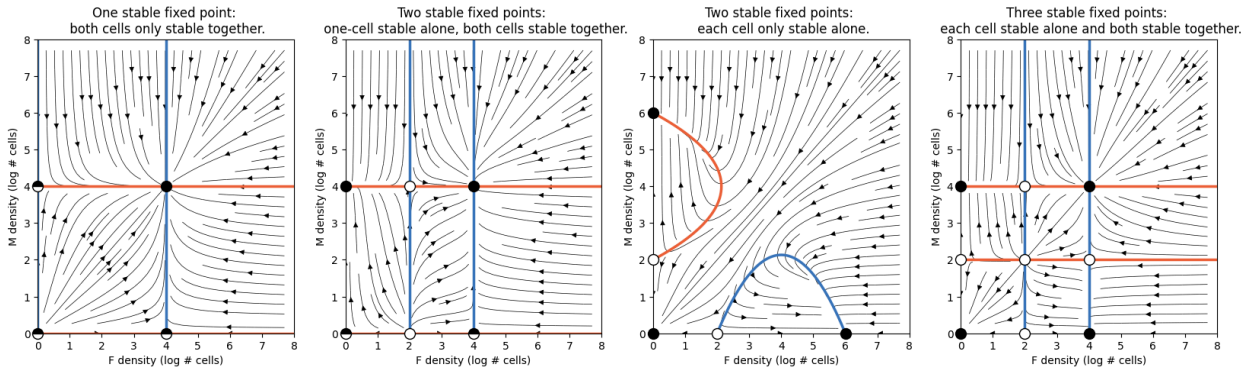

The following simulations show that some aspects are recovered with very few cells (as little as 1K), such as a stable point off-axis or presence of any kind of stability on an axis. Discerning between types of stability on the axes requires more cells. At 25K cells all aspects are recovered with high accuracy.

Supplementary 2E. Simulation 1 - One fixed point

Ground truth model:

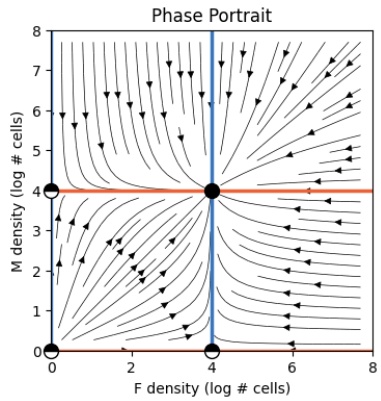

Division & death rates have magnitudes resembling real data (total divisions: 2.2% and 2.1% for F, M respectively)

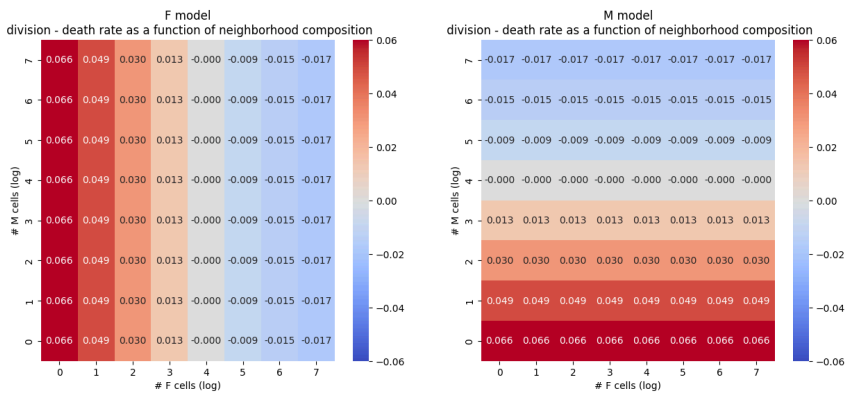

Distribution produced by spatial simulation:

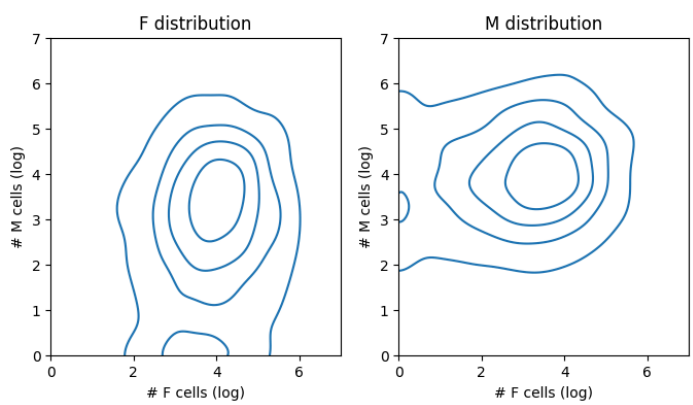

Distribution of fixed points for different sample sizes:

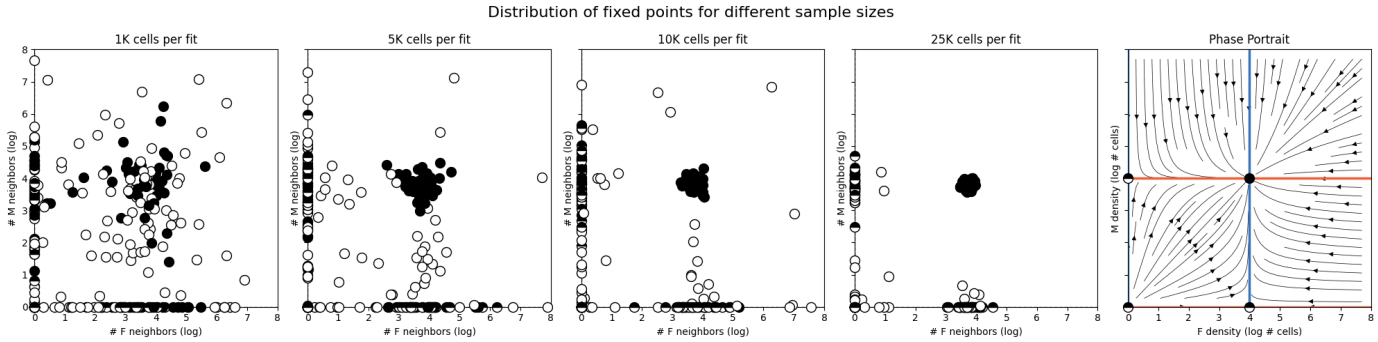

Accuracy of recovered model attributes as a function of sample size:

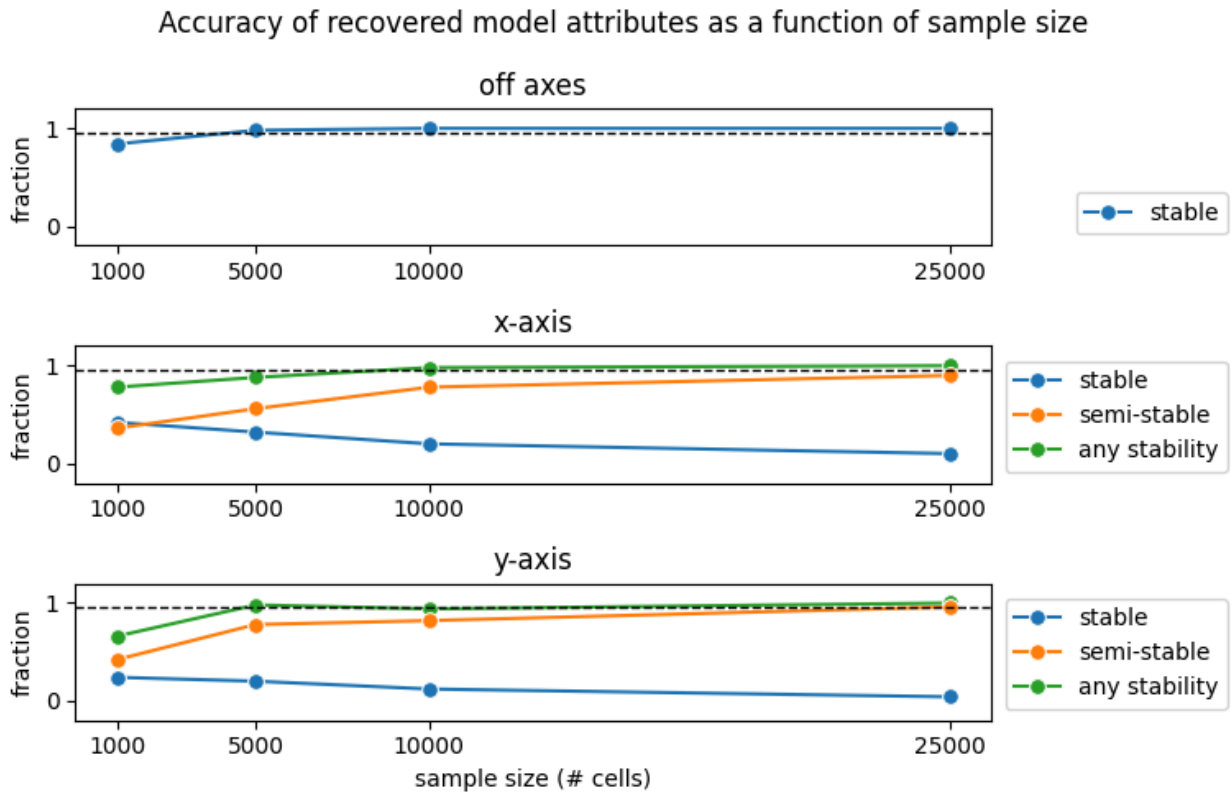

Supplementary 2F. Simulation 2 - Two fixed points

Ground truth model:

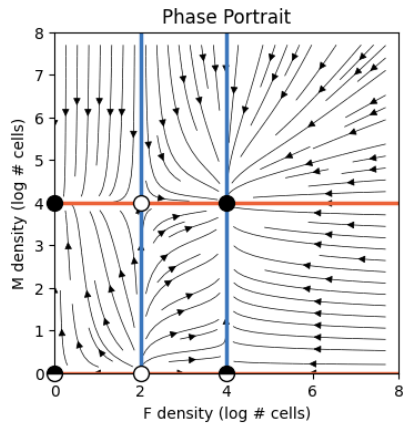

Division & death rates have magnitudes resembling real data (total divisions: 1.6% and 2.3% for F, M respectively)

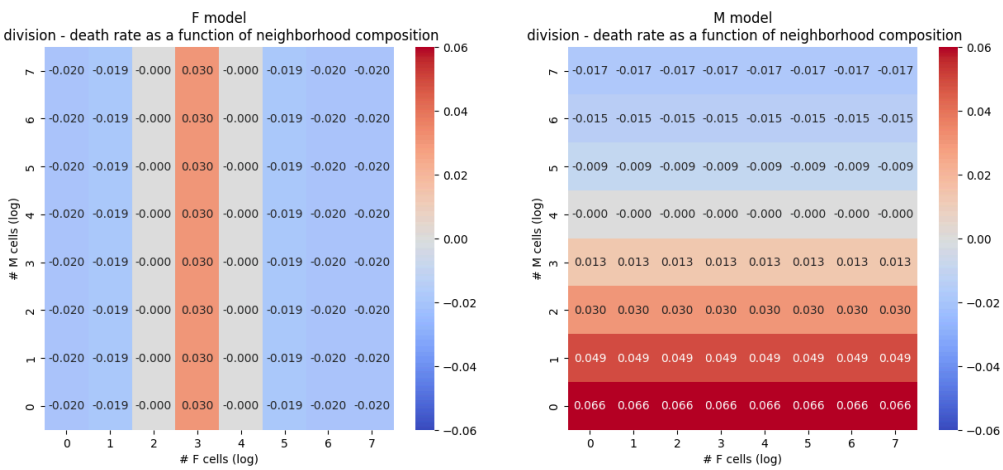

Distribution produced by spatial simulation:

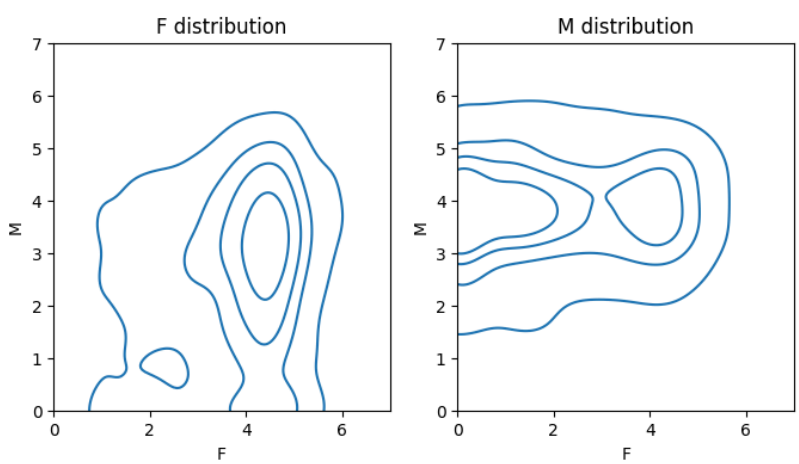

Distribution of fixed points for different sample sizes:

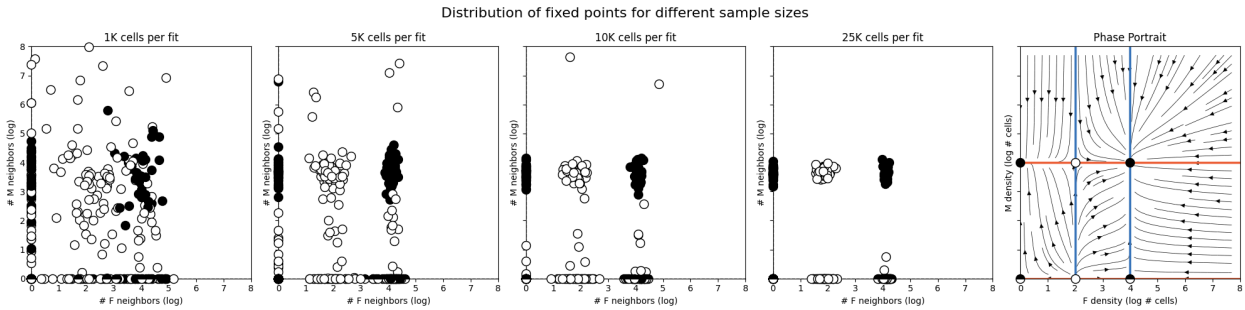

Accuracy of recovered model attributes as a function of sample size:

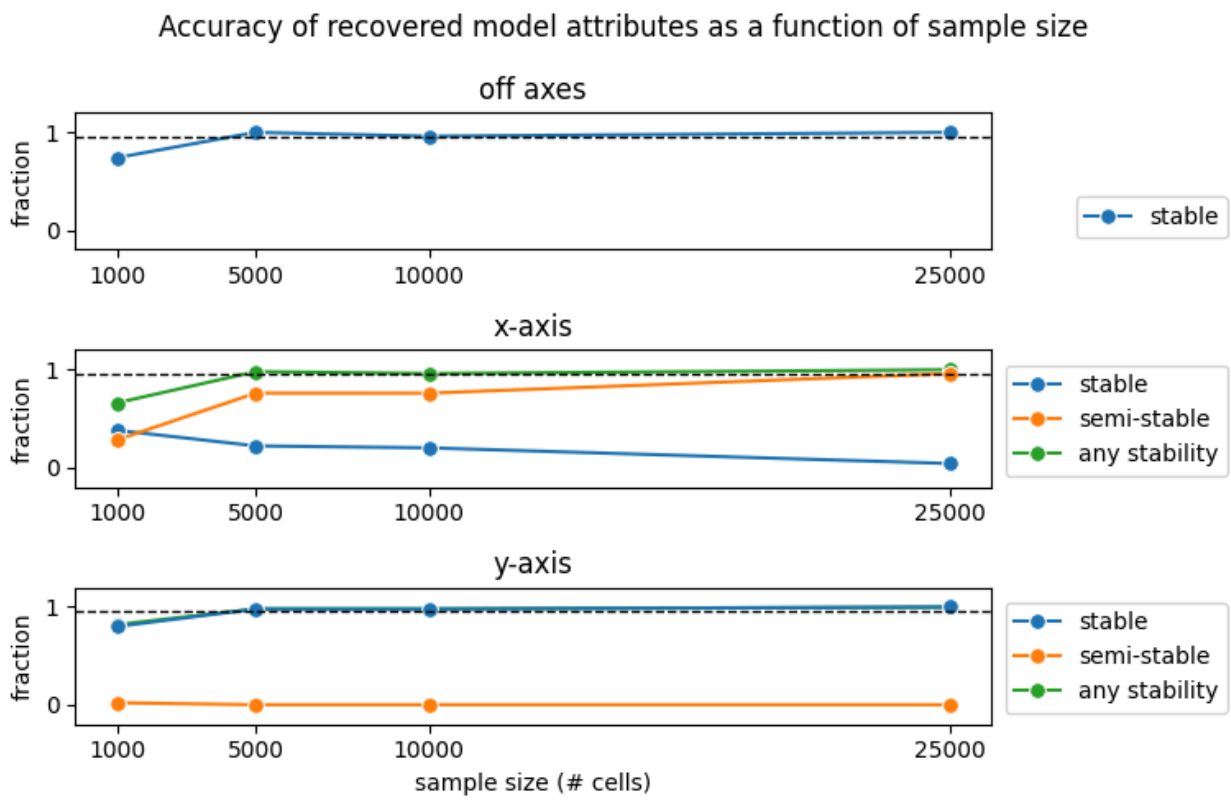

Supplementary 2G. Simulation 3 - Two fixed points, one on each axis

Ground truth model:

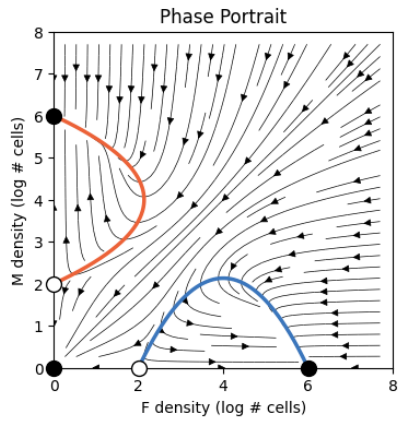

Division & death rates have magnitudes resembling real data (total divisions: 2.3% and 2.1% for F, M respectively)

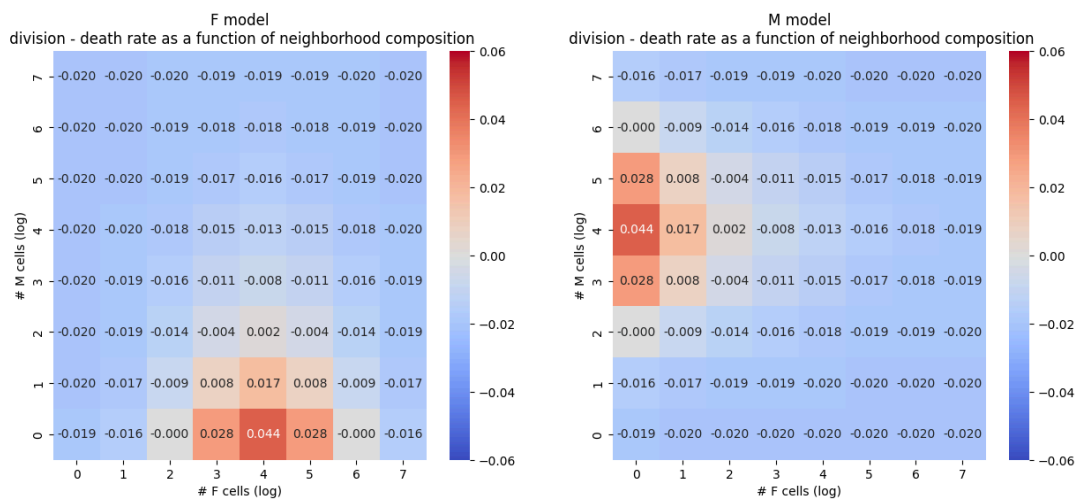

Distribution produced by spatial simulation:

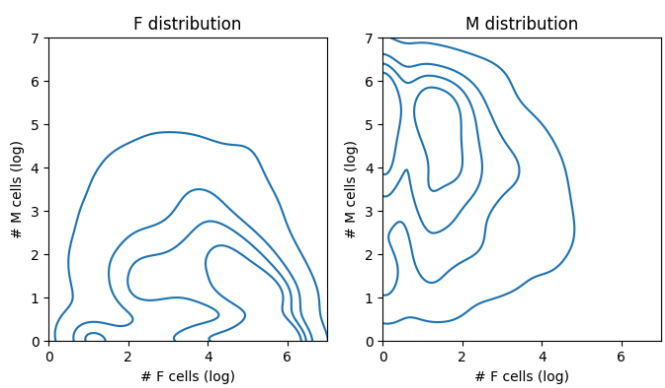

Distribution of fixed points for different sample sizes:

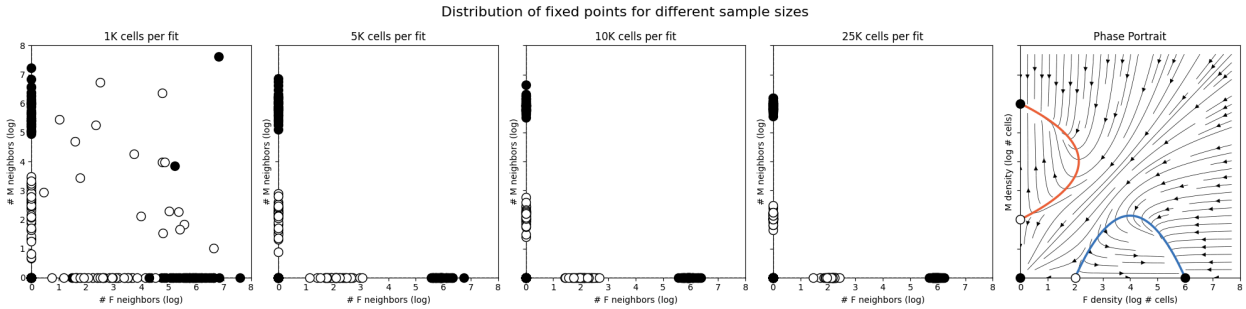

Accuracy of recovered model attributes as a function of sample size:

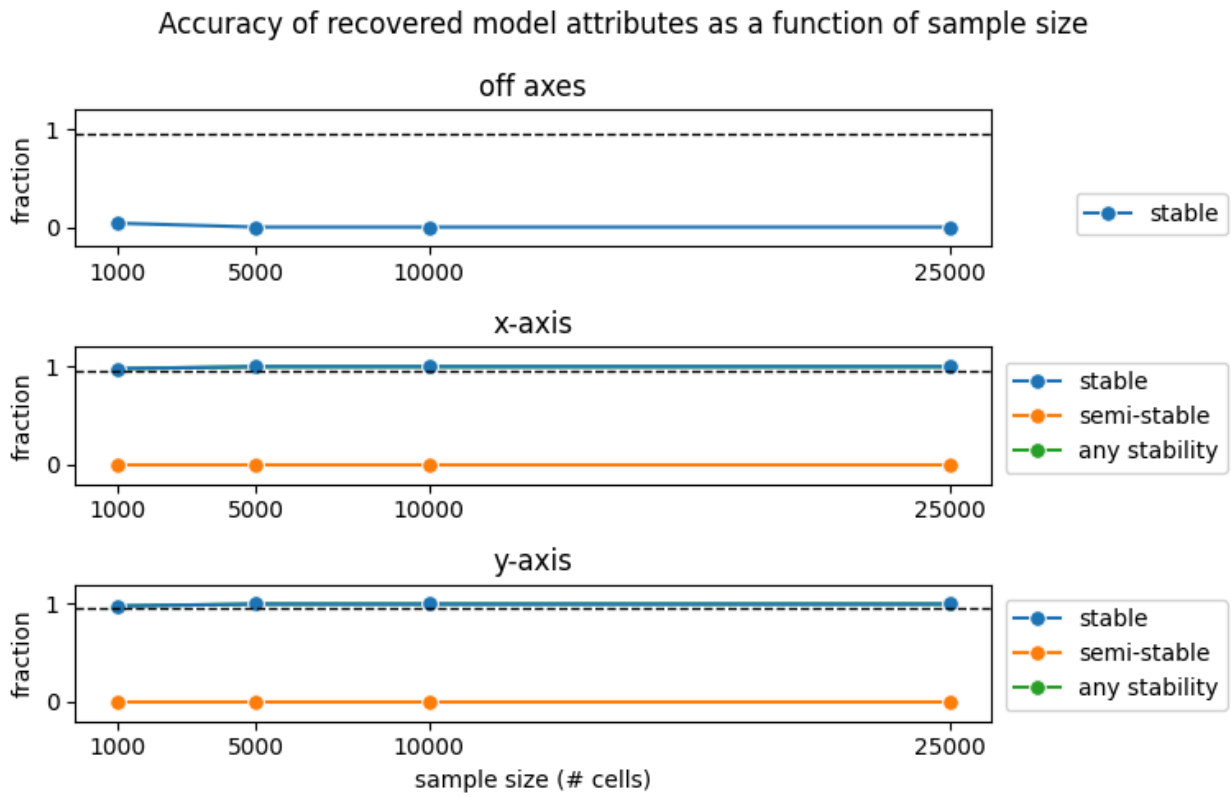

S2H) Simulation 4 - Three fixed points, one on each axis and one off-axes

Ground truth model:

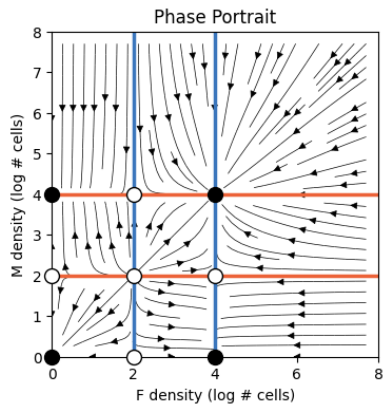

Division & death rates have magnitudes resembling real data (total divisions: 2.4% and 2.2% for F, M respectively)

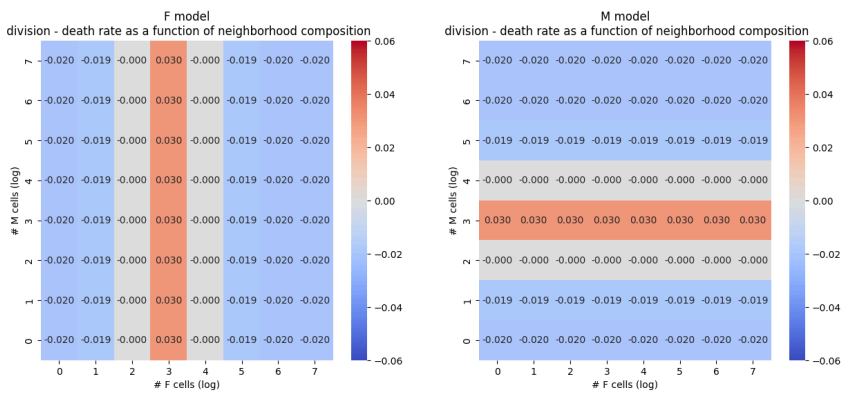

Distribution produced by spatial simulation:

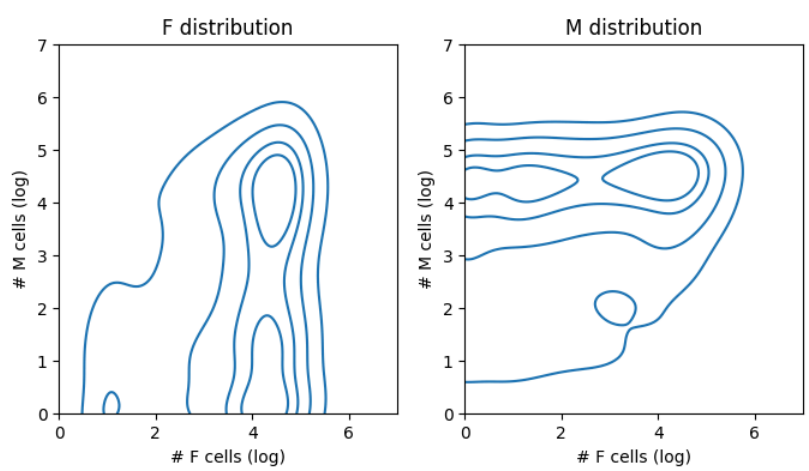

Distribution of fixed points for different sample sizes:

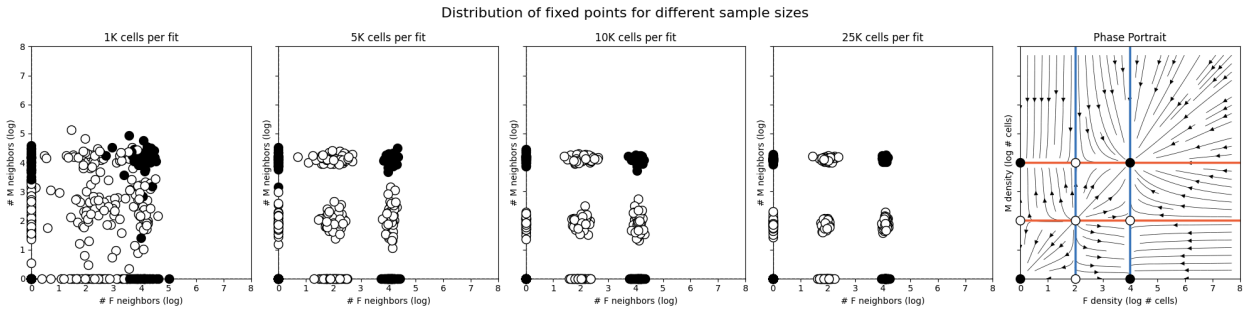

Accuracy of recovered model attributes as a function of sample size:

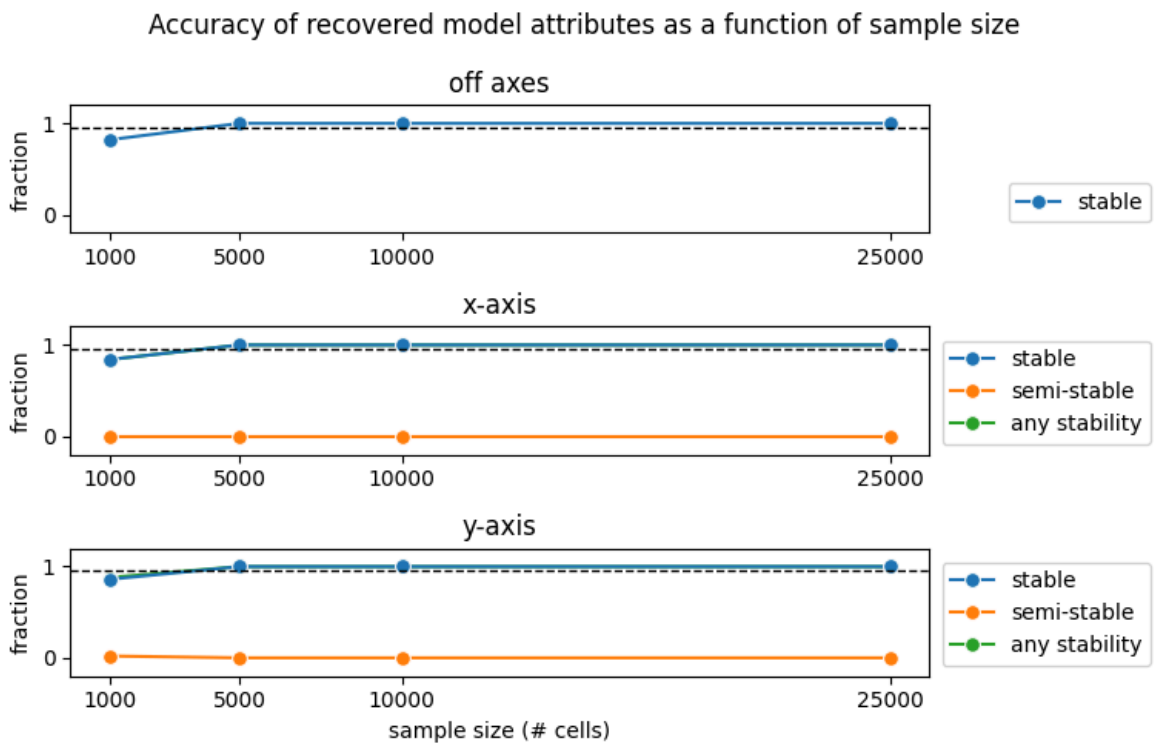

Supplementary 3: Fibroblast-macrophage analysis

S3A) Model selection using cross-validation suggests a 2nd order polynomial

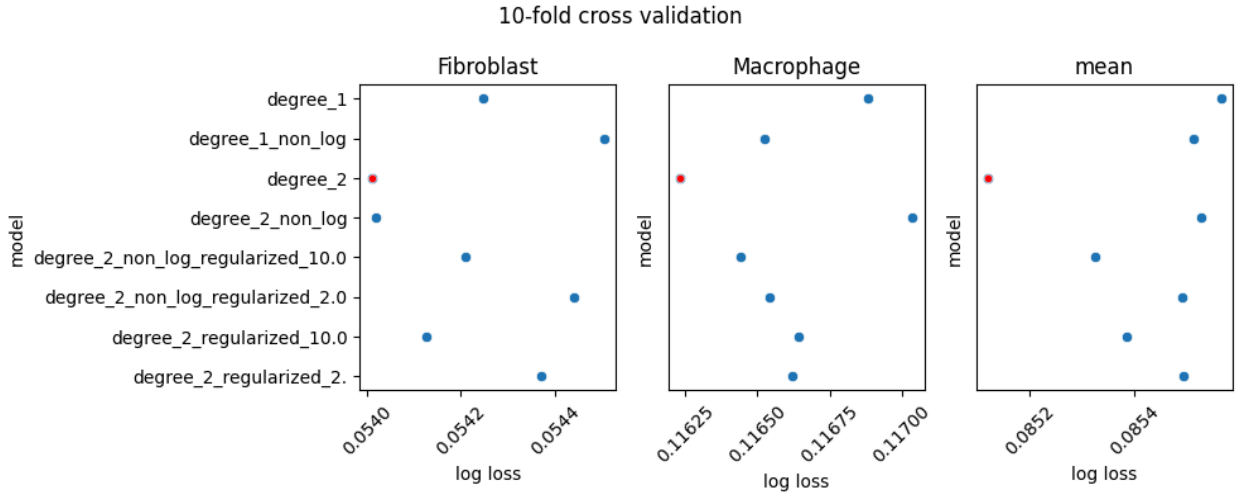

S3B) The Fibroblast-Macrophage phase-portrait is robust to cell-level bootstrap resampling

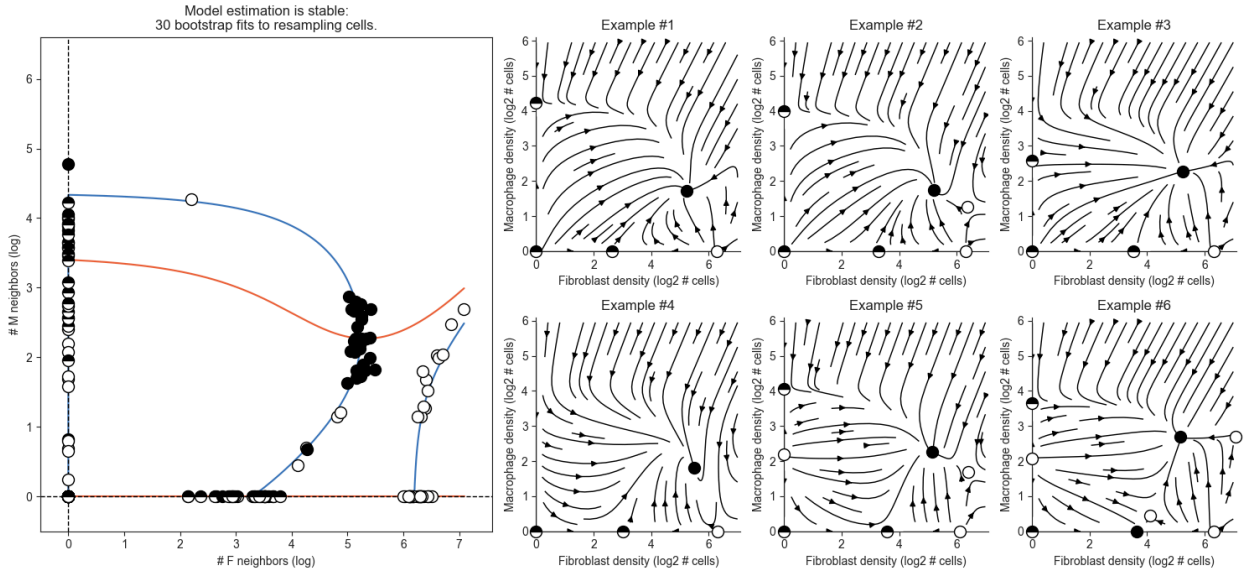

S3C) The Fibroblast-Macrophage phase-portrait is robust to <u>sample-level</u> bootstrap resampling

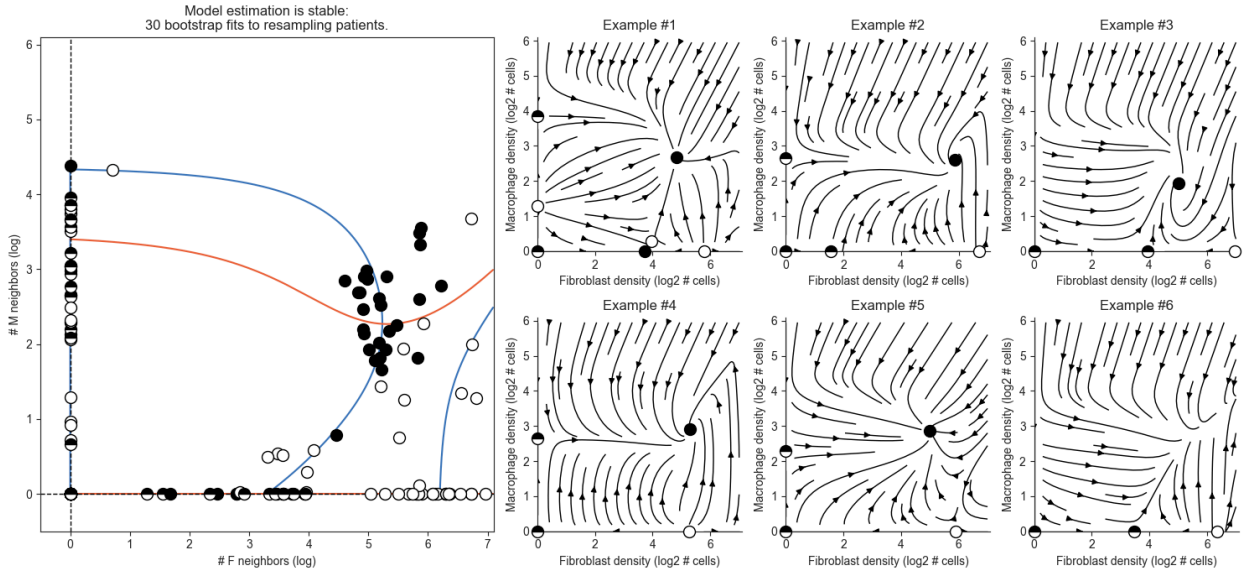

S3D) Number of cells and divisions as a function of neighborhood size and ki67

Because we exclude fibroblasts or macrophages with neighboring adaptive immune cells, the number of cells included in the analysis depends on the neighborhood size. We plot the number of cells and divisions for each combination. In S3F we show that analysis is robust to this choice. Cell numbers drop with neighborhood size because larger size increases probability of T and B cells, and thus exclusion of that neighborhood.

Number of Fibroblast divisions as function of neighborhood size and KI67 threshold

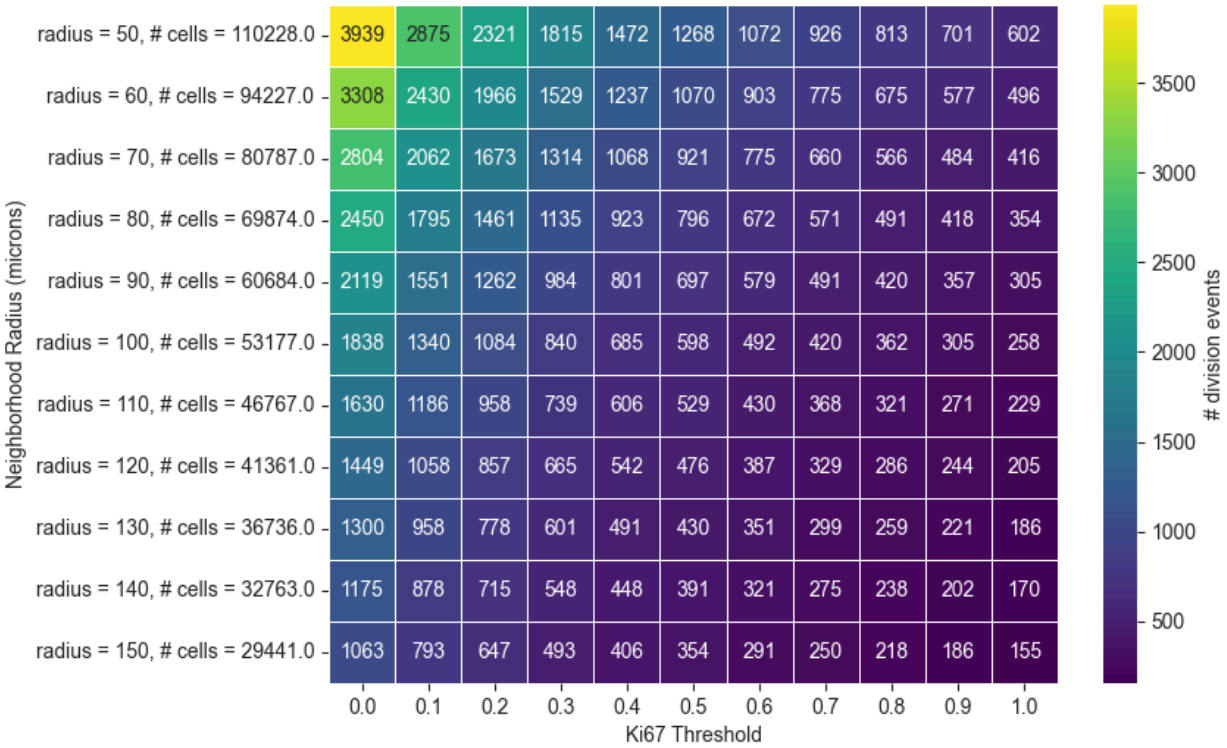

Number of Macrophage divisions as function of neighborhood size and KI67 threshold

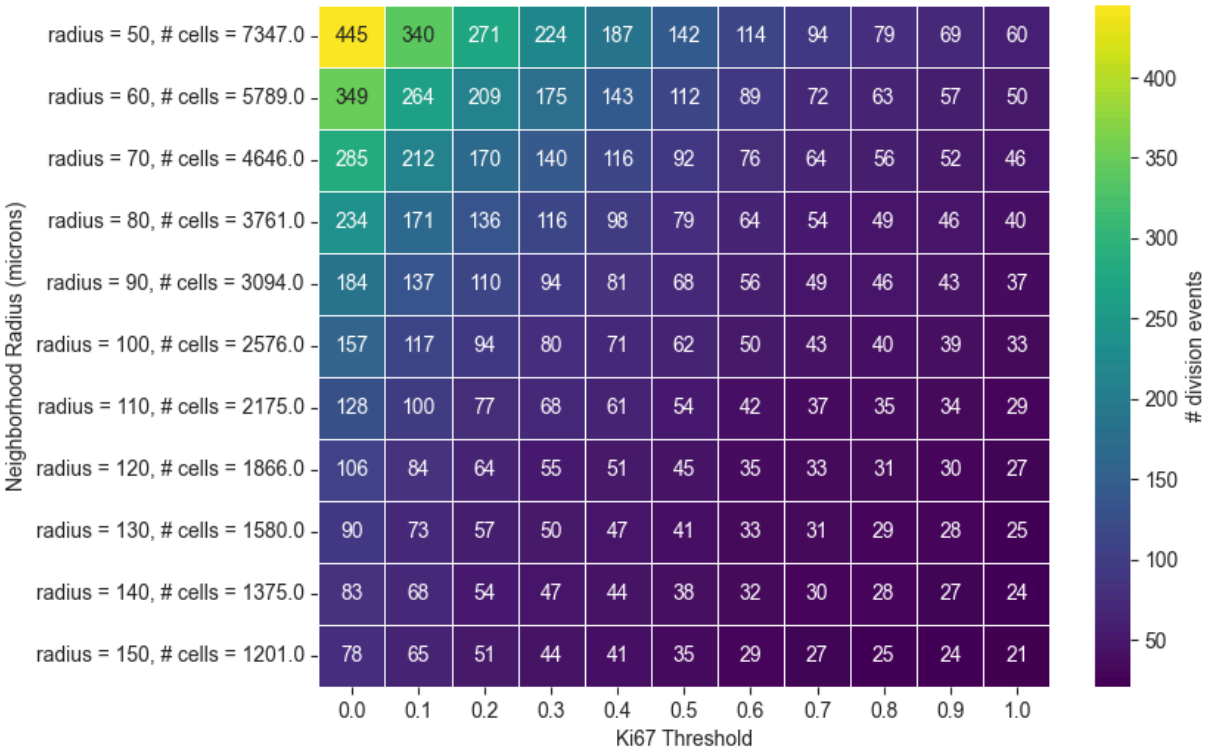

S3E) The Fibroblast-Macrophage phase-portrait is robust to choice of Ki67 threshold and neighborhood size

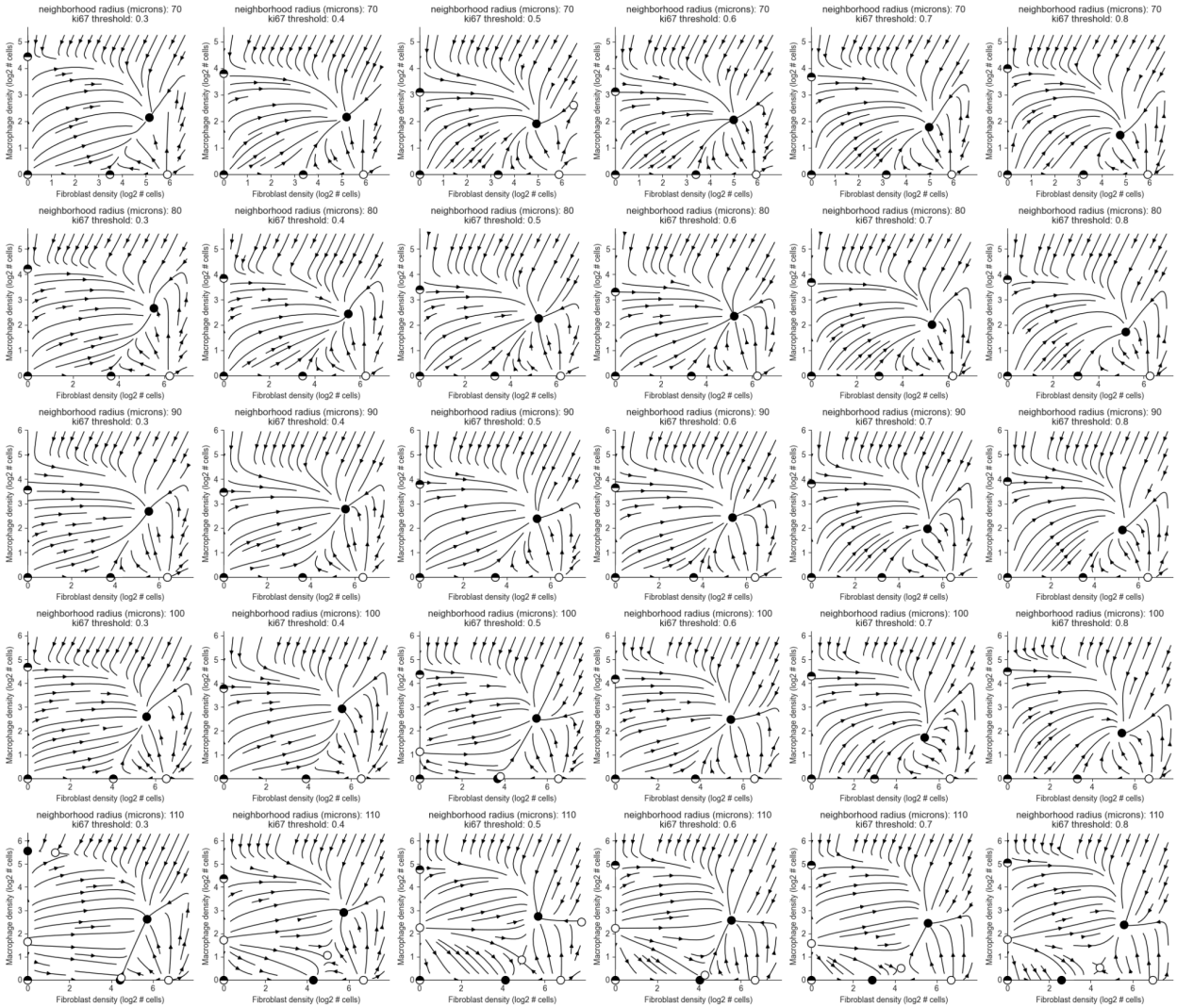

S3F) The Fibroblast-Macrophage phase-portrait is robust to perturbation of the death estimate

Here we plot the phase-portrait against different constant death rates. The constant used throughout this study is equal to the mean division rate. This approximation is exact at steady state. We show that dynamics are largely preserved even for constants that produce a doubling or halving time of 2 weeks for a cell population.

The computation of the doubling time is as follows: say a cell has a mean division rate of 0.02 per time step. For a death rate that is 70% of the division rate, at each time step we gain (0.02 - 0.02*0.7) x the number of cells. Note this is an exponential growth.

We get a doubling time of:
T = log(2) / log(1 + 0.02 - 0.02*0.7) = 115 steps
This is ~2 weeks for a timestep of 3 hours.

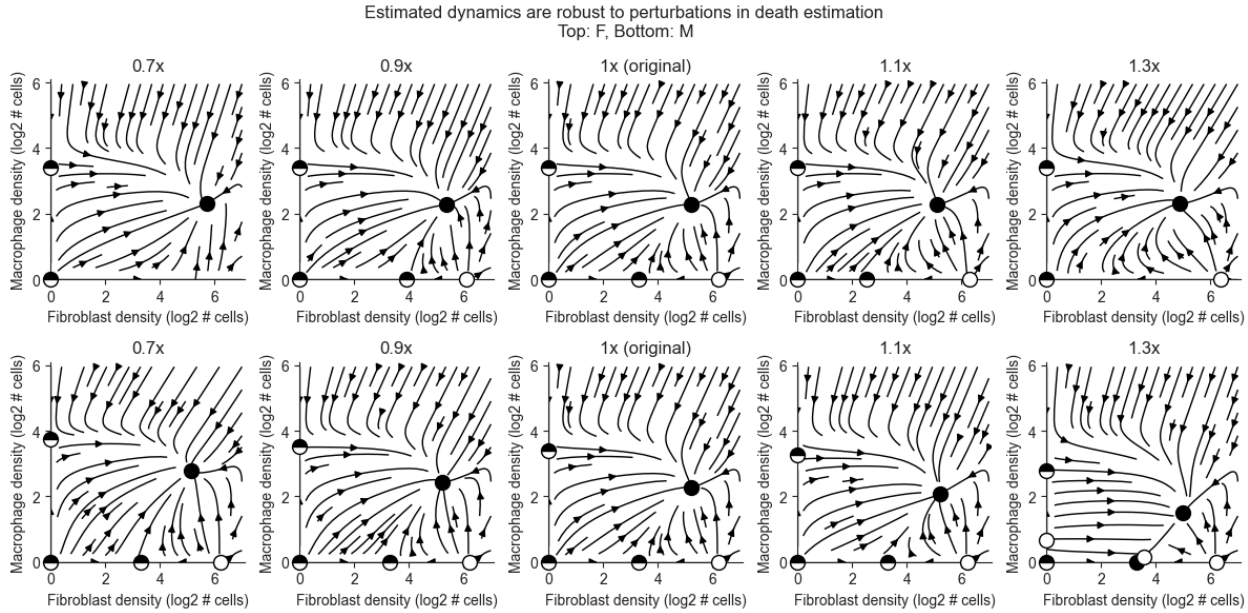

S3G) Fibroblast-Macrophage dynamics are consistent when modeled together with a third cell types

Tumor and Endothelial cells were present in the neighborhoods in the main analysis but weren't included in the model (recall, neighborhoods with adaptive immune cells were excluded). Here, we fit a model including 3 cell types each time, then dynamics are plotted for values ranging from the 20th to the 80th quantile density of the 3rd cell type.

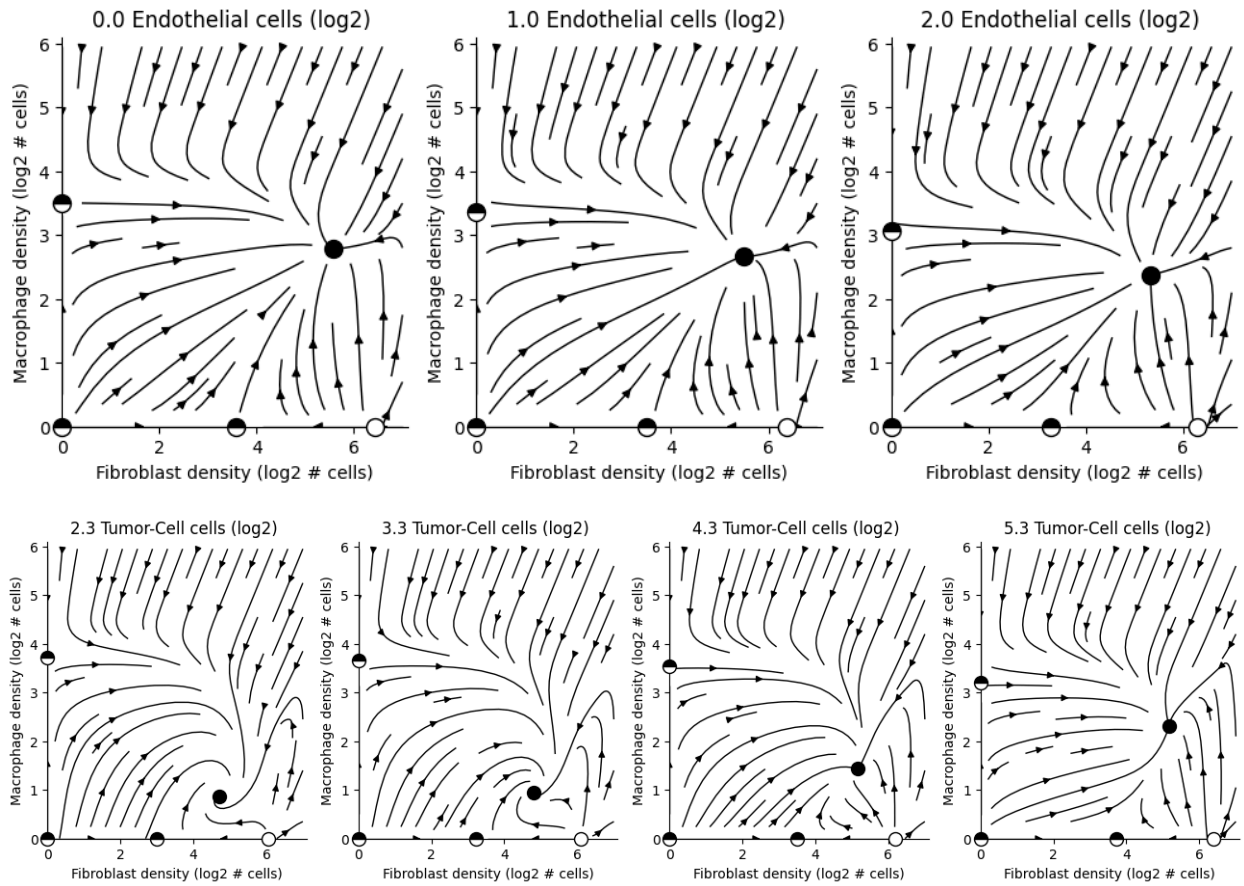

S3H) Fibroblast Macrophage Dynamics are conserved between various meaningful patient subgroups

Note that some fits include a very small sample size. The complete cohort had ~4K macrophages. Despite partitioning this initially low sample size in half or less, many elements of the original phase portrait are preserved. (see simulations that establish accuracy for various sample sizes - S2 C,D,E,F & G)

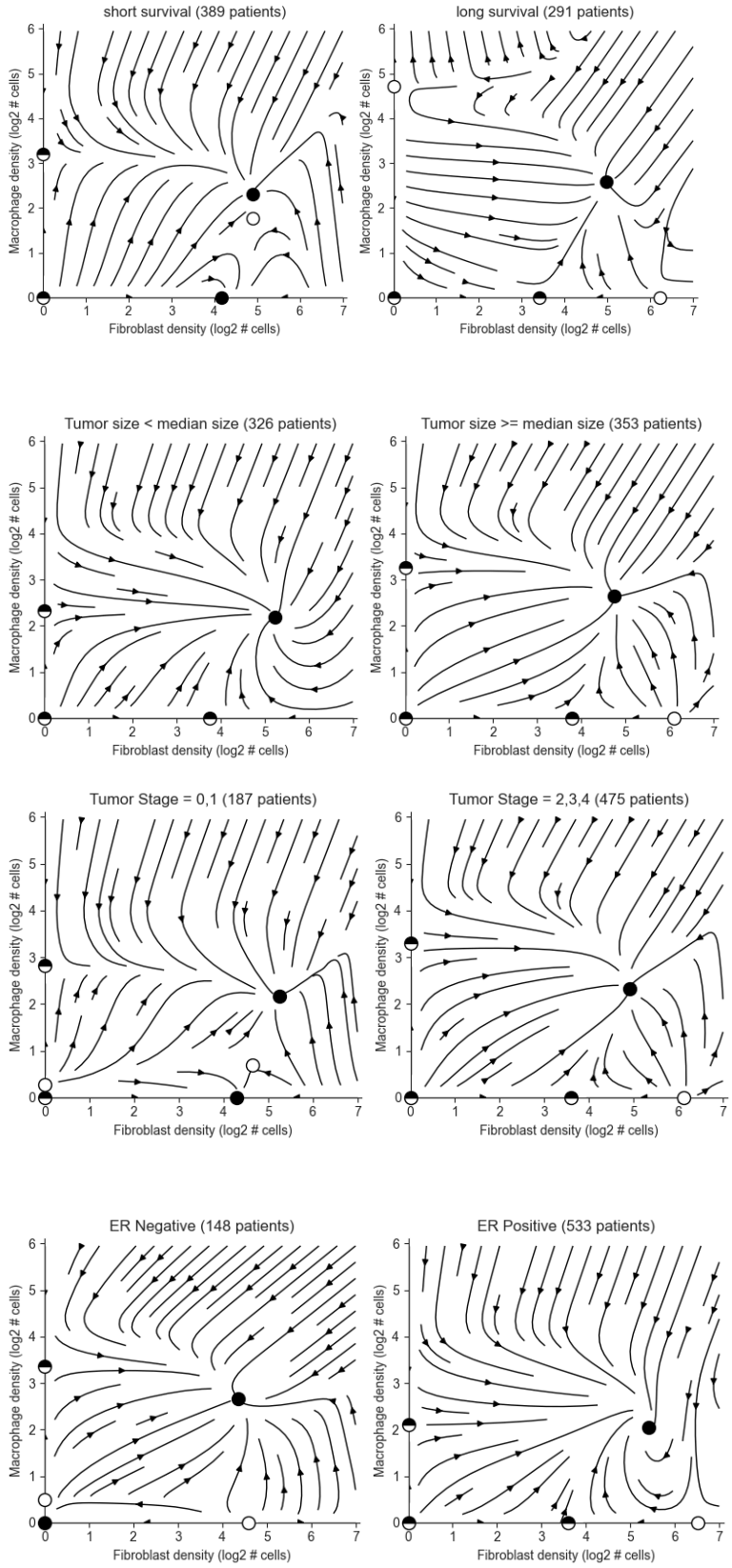
short survival (389 patients)
long survival (291 patients)
Tumor size < median size (326 patients)
Tumor size >= median size (353 patients)
Tumor Stage = 0,1 (187 patients)
Tumor Stage = 2,3,4 (475 patients)
ER Negative (148 patients)
ER Positive (533 patients)
Macrophage density (log2 # cells)
Fibroblast density (log2 # cells)

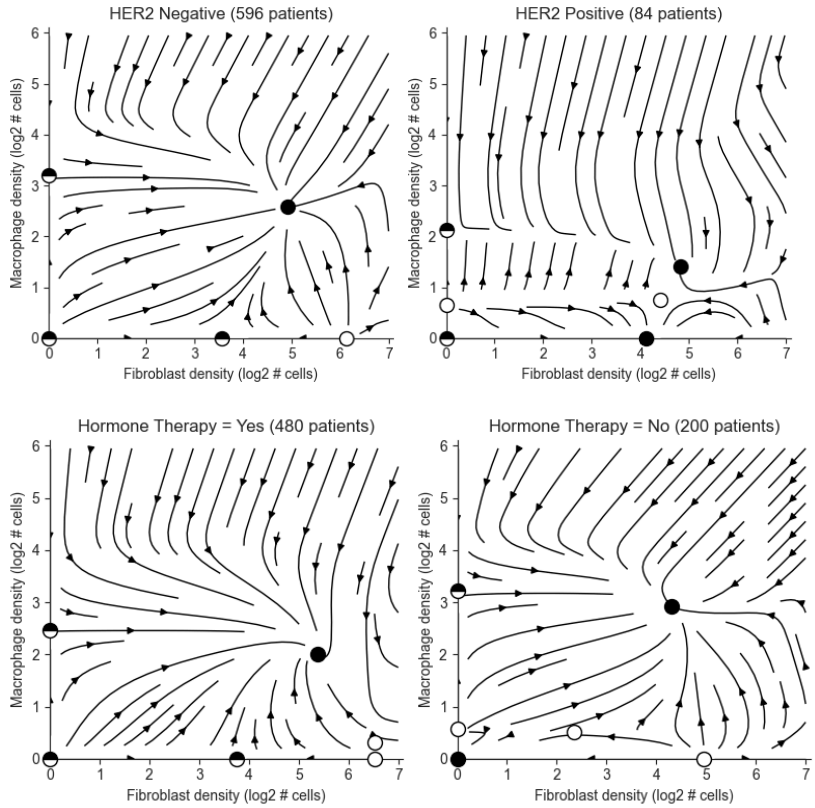

S3I) Inferred fibroblast-macrophage dynamics without excluding neighborhoods with adaptive immune cells

Note that the estimated phase-portrait is dominated by the hot-fibrosis fixed point. Remarkably, this point is located almost precisely at the hot-fibrosis fixed point estimated without adaptive immune cells.

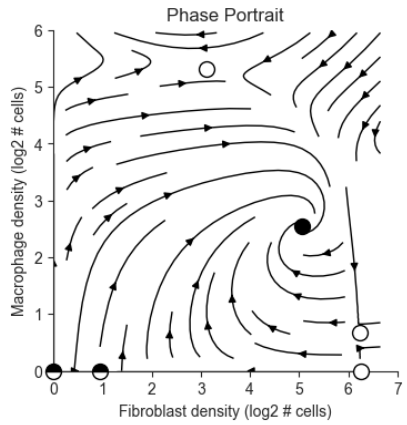

<u>Supplementary 4: T & B cell analysis</u>

S4A) Model Selection

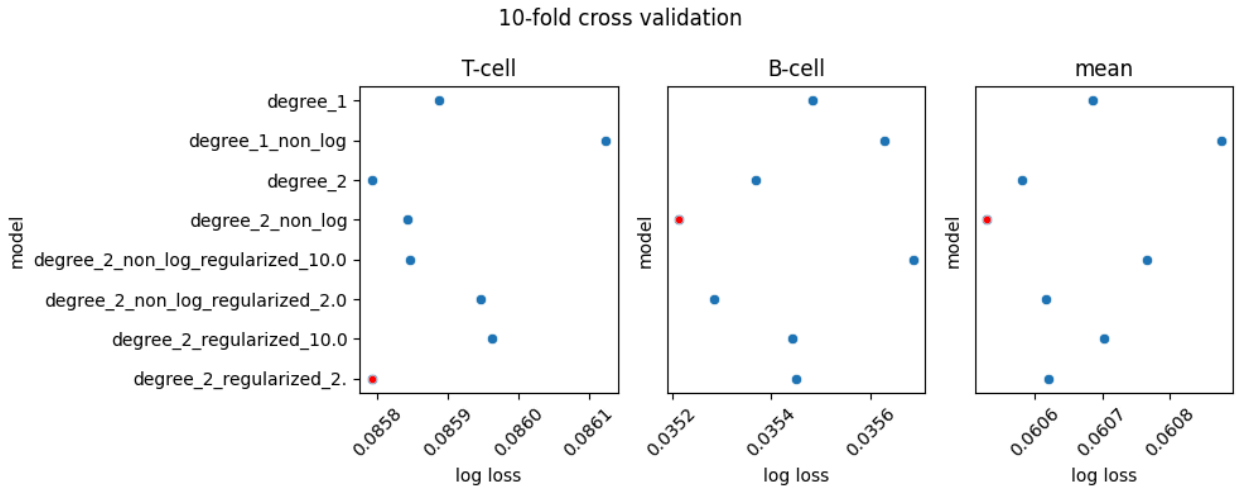

S4B) The T-cell, B-cell phase-portrait is robust to cell-level bootstrap resampling

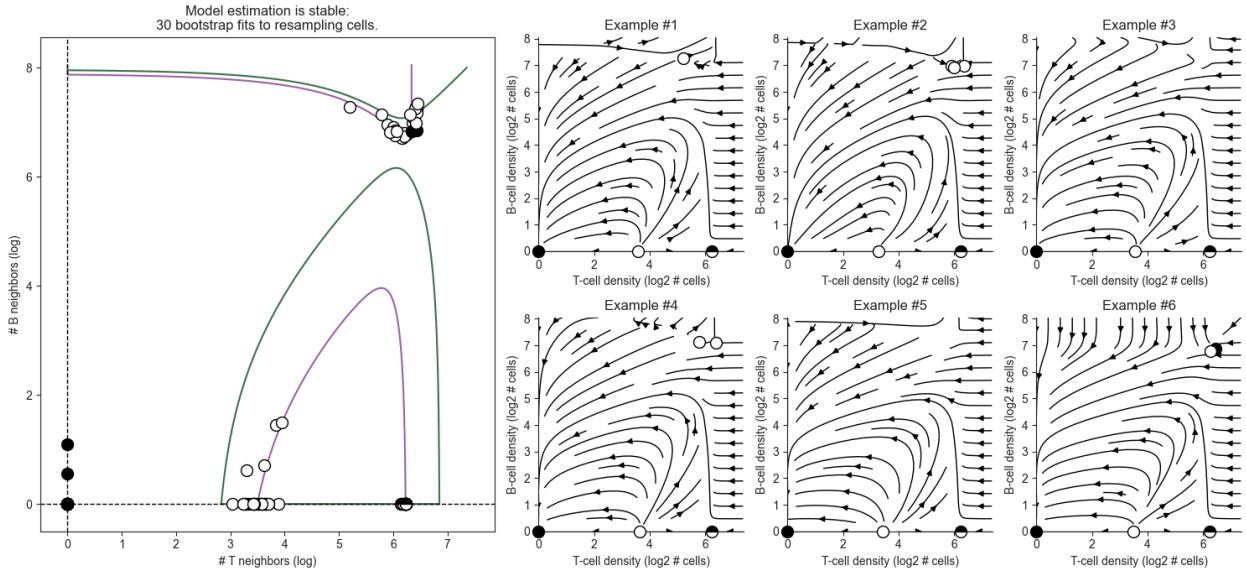

S4C) The T-cell, B-cell phase-portrait is robust to <u>patient</u>-level bootstrap resampling

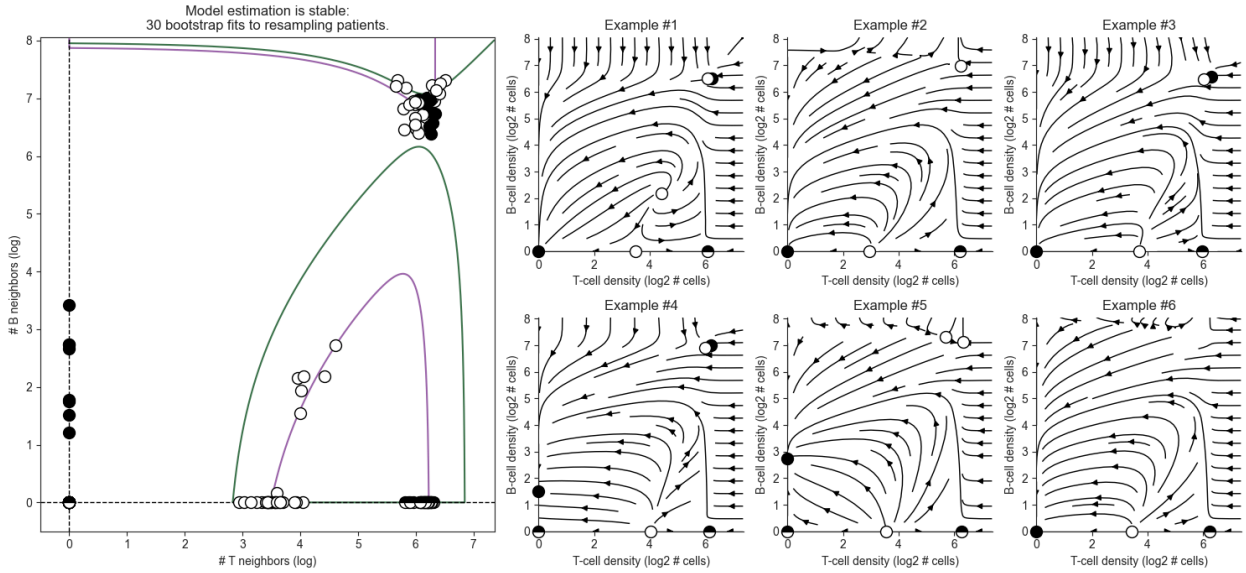

S4D) The T-cell, B-cell phase-portrait is robust to perturbation of the death estimate

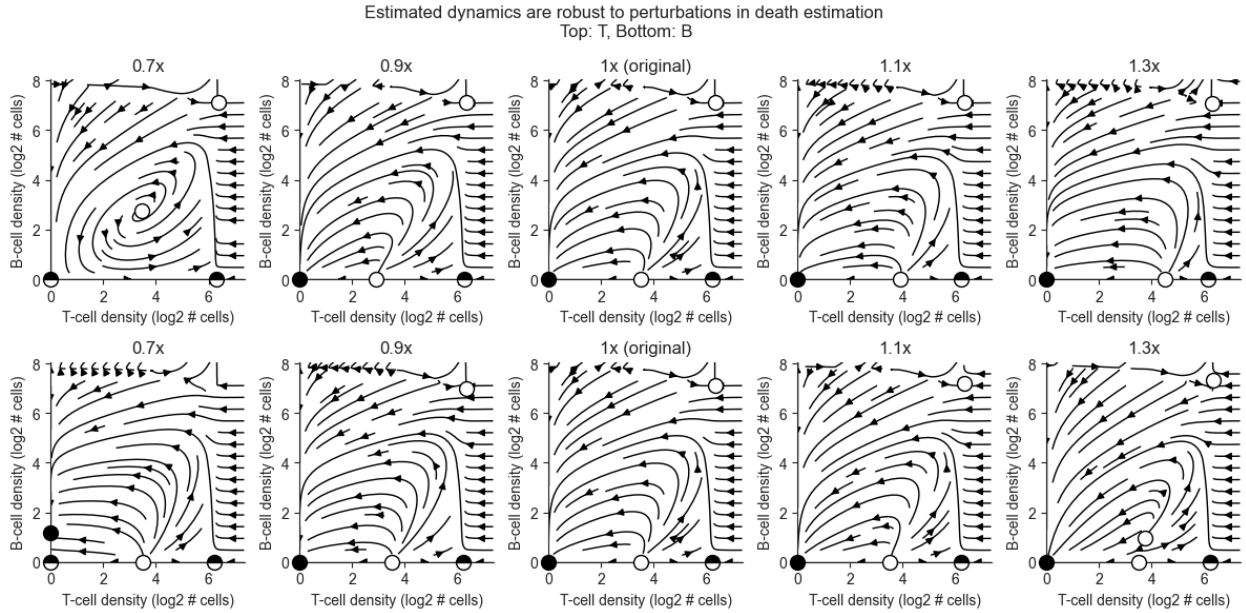

S4E) Ki67 threshold determines fraction of dividing cells:

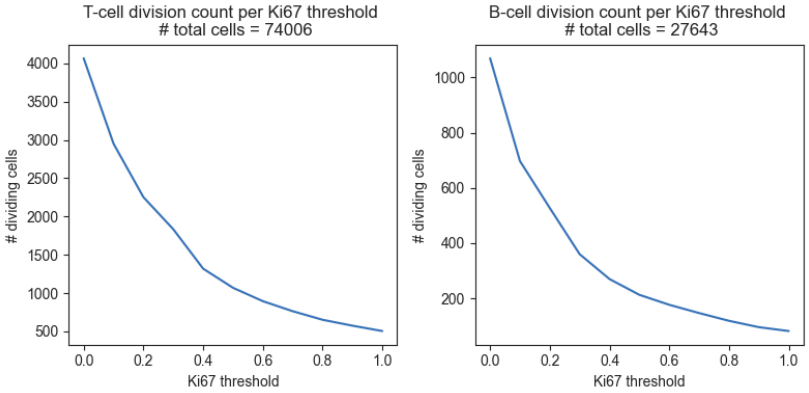

S4F) The T-cell, B-cell phase-portrait estimate is robust to choice of Ki67 threshold and neighborhood size

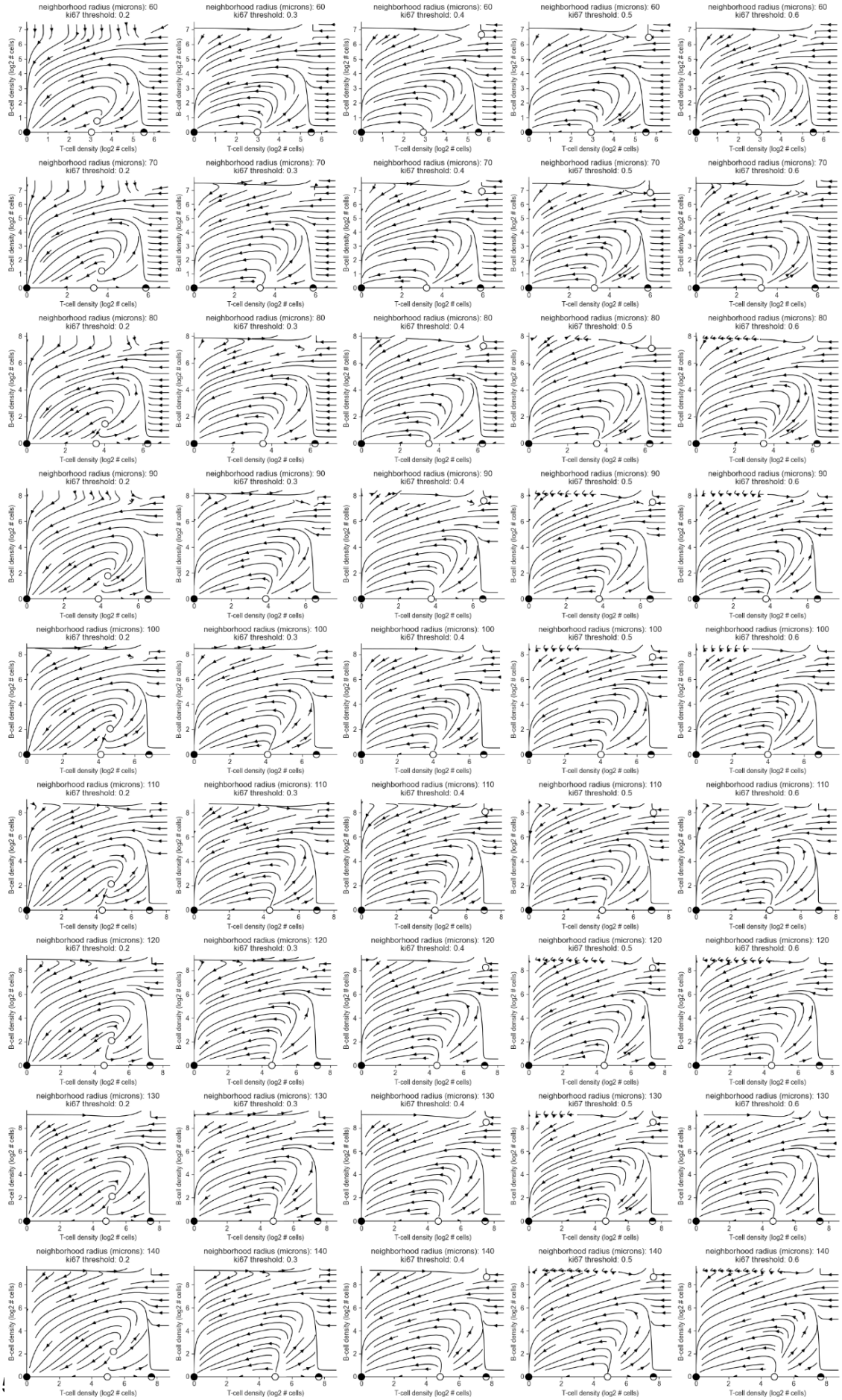
neighborhood radius (microns): 60
ki67 threshold: 0.2
neighborhood radius (microns): 60
ki67 threshold: 0.3
neighborhood radius (microns): 60
ki67 threshold: 0.4
neighborhood radius (microns): 60
ki67 threshold: 0.5
neighborhood radius (microns): 60
ki67 threshold: 0.6
neighborhood radius (microns): 70
ki67 threshold: 0.2
neighborhood radius (microns): 70
ki67 threshold: 0.3
neighborhood radius (microns): 70
ki67 threshold: 0.4
neighborhood radius (microns): 70
ki67 threshold: 0.5
neighborhood radius (microns): 70
ki67 threshold: 0.6
neighborhood radius (microns): 80
ki67 threshold: 0.2
neighborhood radius (microns): 80
ki67 threshold: 0.3
neighborhood radius (microns): 80
ki67 threshold: 0.4
neighborhood radius (microns): 80
ki67 threshold: 0.5
neighborhood radius (microns): 80
ki67 threshold: 0.6
neighborhood radius (microns): 90
ki67 threshold: 0.2
neighborhood radius (microns): 90
ki67 threshold: 0.3
neighborhood radius (microns): 90
ki67 threshold: 0.4
neighborhood radius (microns): 90
ki67 threshold: 0.5
neighborhood radius (microns): 90
ki67 threshold: 0.6
neighborhood radius (microns): 100
ki67 threshold: 0.2
neighborhood radius (microns): 100
ki67 threshold: 0.3
neighborhood radius (microns): 100
ki67 threshold: 0.4
neighborhood radius (microns): 100
ki67 threshold: 0.5
neighborhood radius (microns): 100
ki67 threshold: 0.6
neighborhood radius (microns): 110
ki67 threshold: 0.2
neighborhood radius (microns): 110
ki67 threshold: 0.3
neighborhood radius (microns): 110
ki67 threshold: 0.4
neighborhood radius (microns): 110
ki67 threshold: 0.5
neighborhood radius (microns): 110
ki67 threshold: 0.6
neighborhood radius (microns): 120
ki67 threshold: 0.2
neighborhood radius (microns): 120
ki67 threshold: 0.3
neighborhood radius (microns): 120
ki67 threshold: 0.4
neighborhood radius (microns): 120
ki67 threshold: 0.5
neighborhood radius (microns): 120
ki67 threshold: 0.6
neighborhood radius (microns): 130
ki67 threshold: 0.2
neighborhood radius (microns): 130
ki67 threshold: 0.3
neighborhood radius (microns): 130
ki67 threshold: 0.4
neighborhood radius (microns): 130
ki67 threshold: 0.5
neighborhood radius (microns): 130
ki67 threshold: 0.6
neighborhood radius (microns): 140
ki67 threshold: 0.2
neighborhood radius (microns): 140
ki67 threshold: 0.3
neighborhood radius (microns): 140
ki67 threshold: 0.4
neighborhood radius (microns): 140
ki67 threshold: 0.5
neighborhood radius (microns): 140
ki67 threshold: 0.6
B-cell density (log2 # cells)
T-cell density (log2 # cells)

S4G) T & B cell dynamics are consistent when modeled together with various cell types and under various levels of the 3rd cell

Fibroblast, Macrophage, Tumor & Endothelial cells were present in the neighborhoods in the main analysis but weren't included in the model. Here, we fit a model including 3 cell types each time, then dynamics are plotted for values ranging from the 20th to the 80th quantile density of the 3rd cell type.

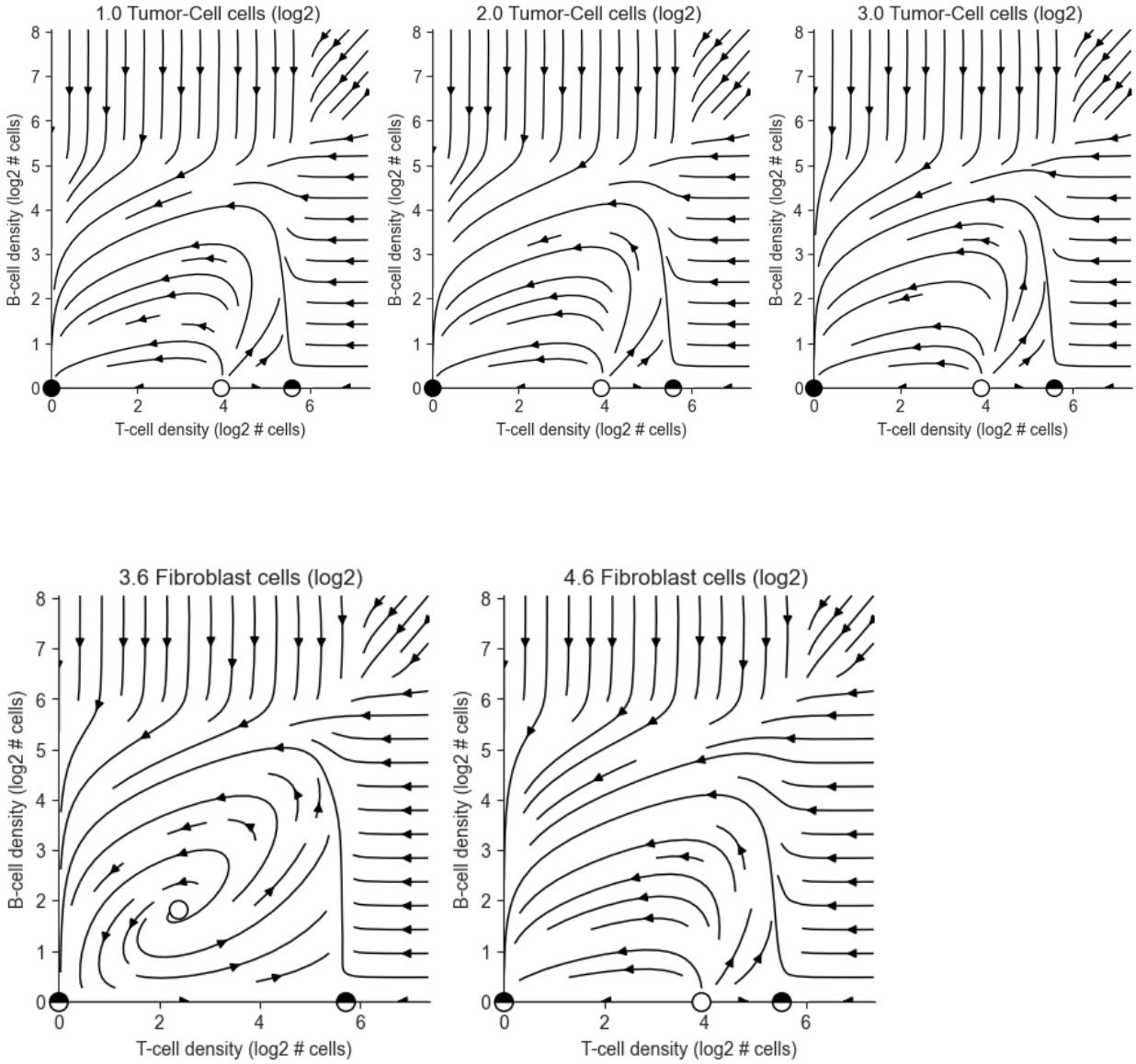

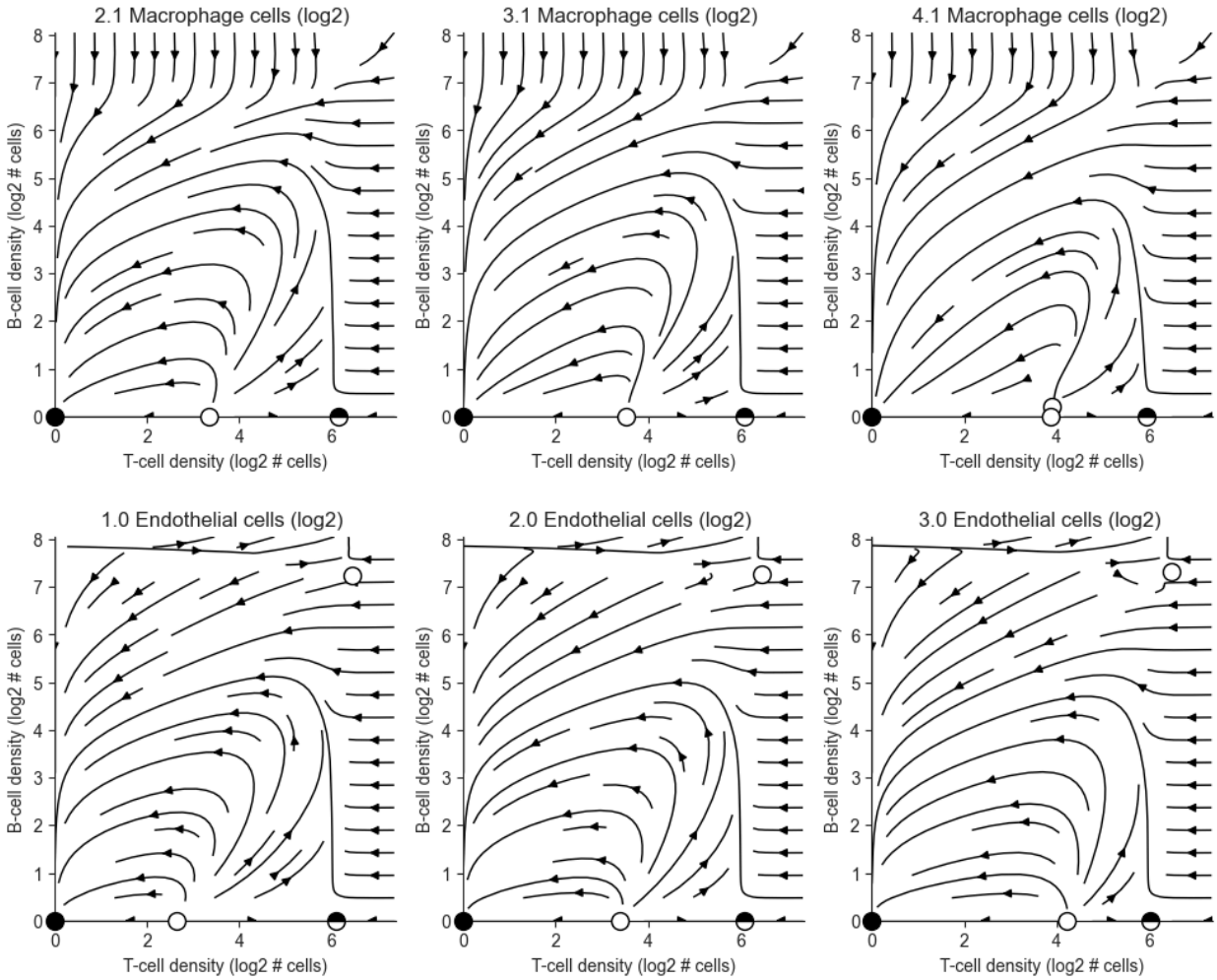

S4H) T & B cell Dynamics are conserved between various meaningful patient subgroups

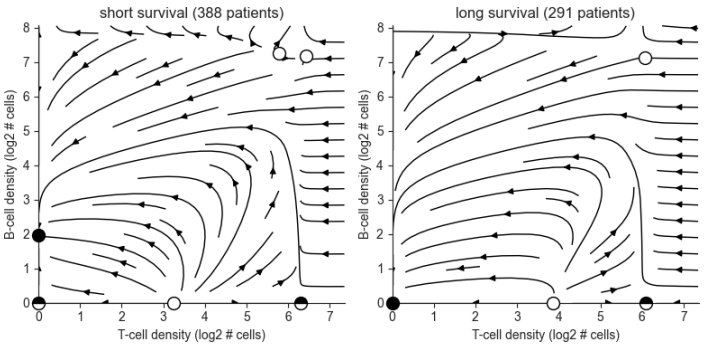

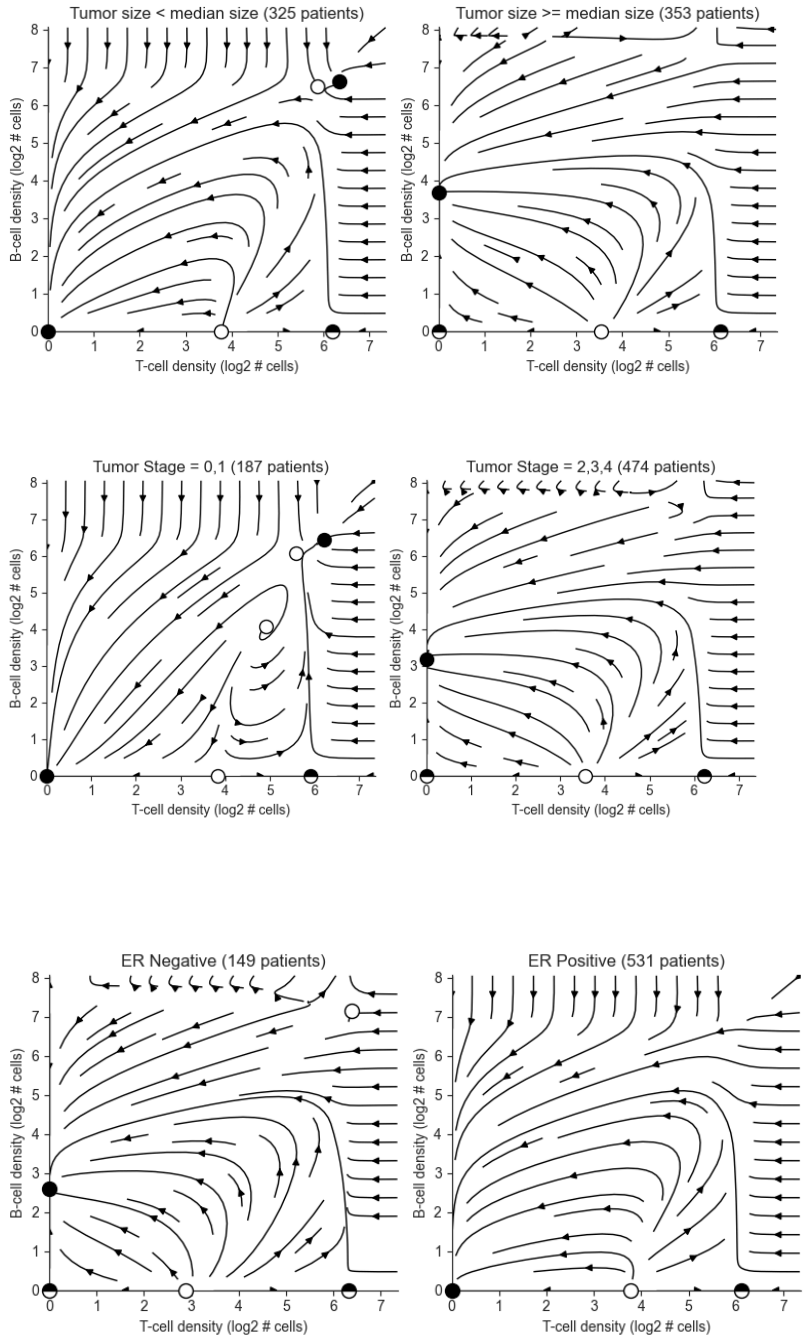
Tumor size < median size (325 patients)
Tumor size >= median size (353 patients)
Tumor Stage = 0,1 (187 patients)
Tumor Stage = 2,3,4 (474 patients)
ER Negative (149 patients)
ER Positive (531 patients)
B-cell density (log2 # cells)
T-cell density (log2 # cells)

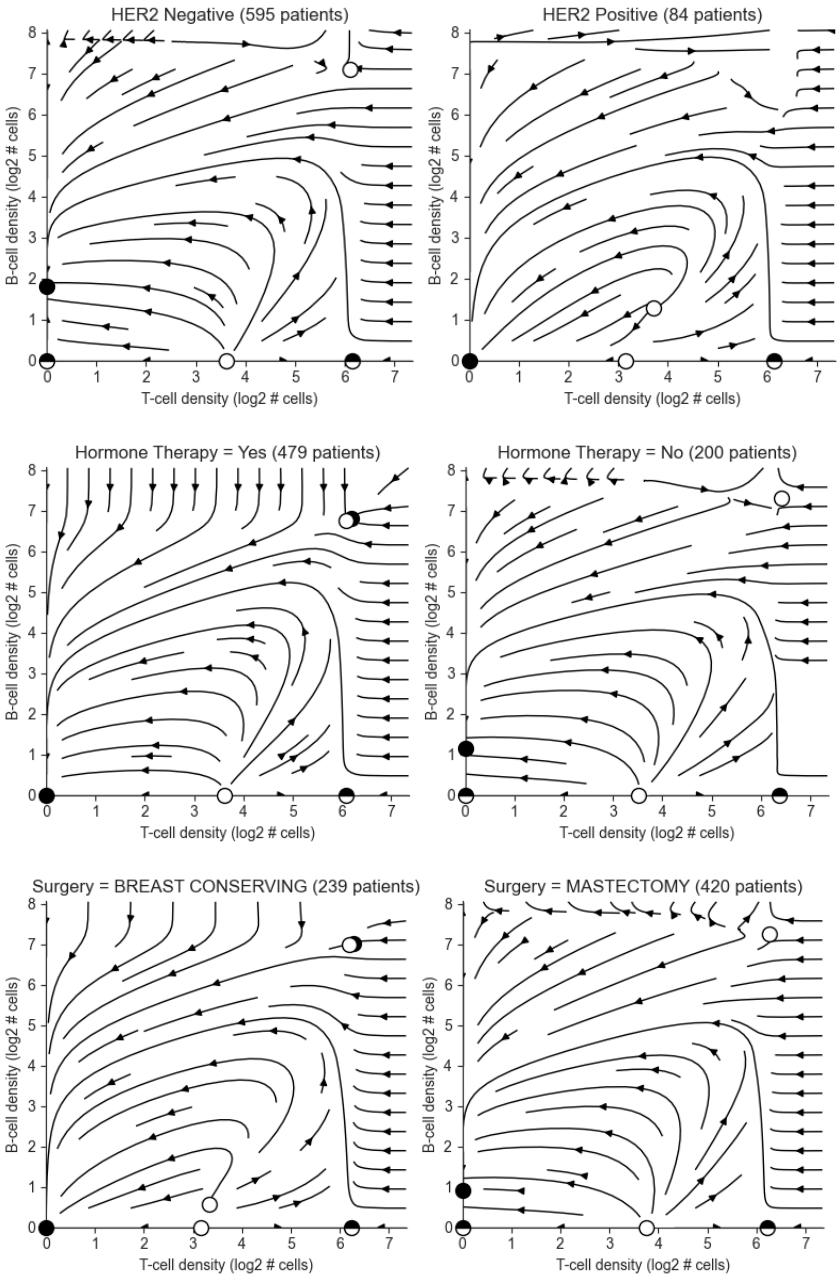
HER2 Negative (595 patients)
HER2 Positive (84 patients)
Hormone Therapy = Yes (479 patients)
Hormone Therapy = No (200 patients)
Surgery = BREAST CONSERVING (239 patients)
Surgery = MASTECTOMY (420 patients)
B-cell density (log2 # cells)
T-cell density (log2 # cells)

Supplementary 5 - Estimating magnitude of error due to unmodeled terms - Fibroblast and Macrophage (FM) model:

S5a - Empirical position of tissues in state-space:

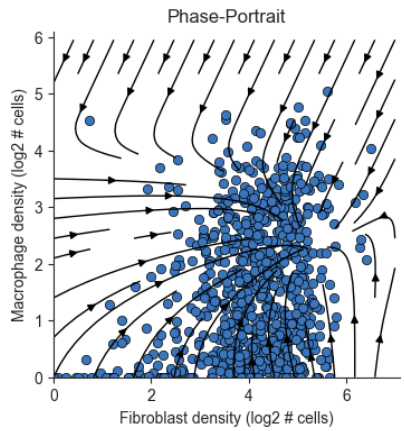

S5b - Estimated density of tissues ρ:

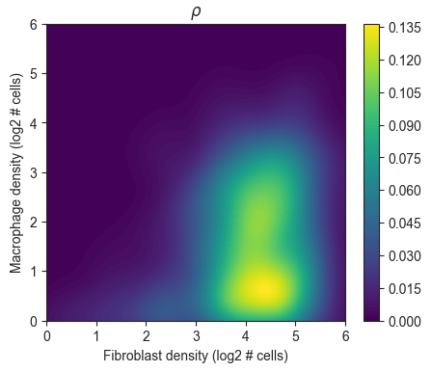

S5c - Estimated divergence of the error field (without diffusion):

The residual field produces a net effect that disperses cells from the peak density.

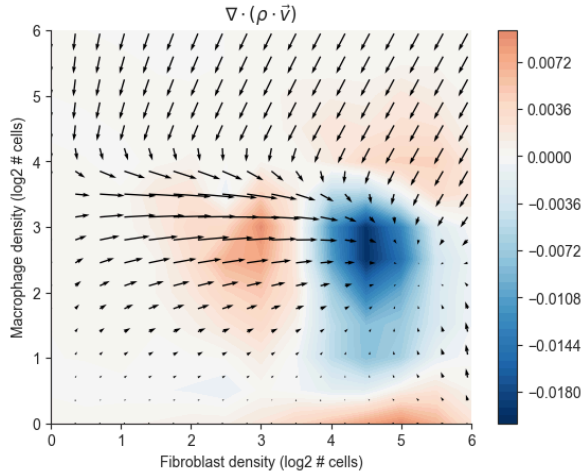

S5c - Estimated divergence of the error field after modeling diffusion:

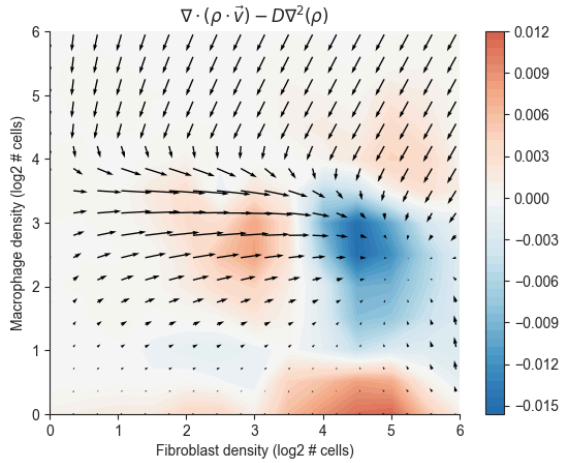

Supplementary 6 - Estimating magnitude of error due to unmodeled terms - T- and B-cell model:

S6a - Empirical position of tissues in state-space:

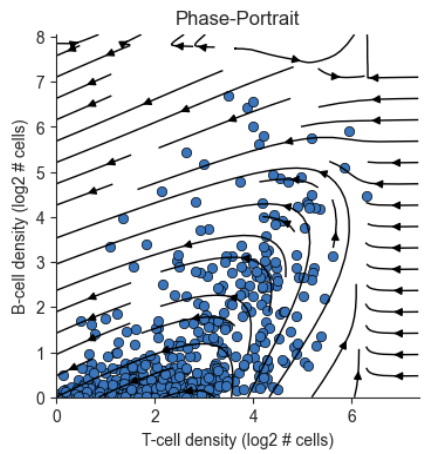

S6b - Estimated density of tissues ρ:

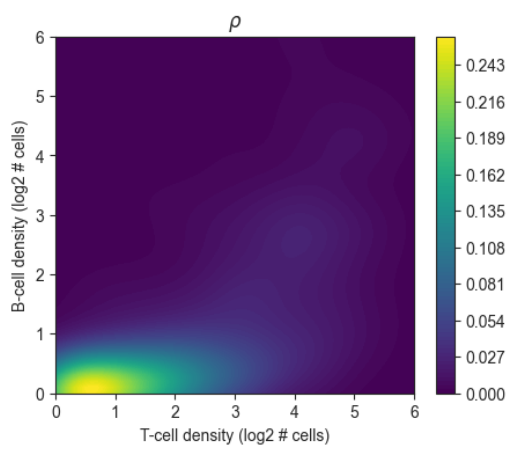

S6c - Estimated divergence of the error field (without diffusion):
There is near-zero influx over most of the state-space. Remarkably, migration of T- and B-cells drives tissues with no T- or B- cells towards the region of the initial threshold of an immune flare. Thus, the high density of immune cells observed at the peak of a flare is primarily driven by local proliferation of adaptive immune cells.

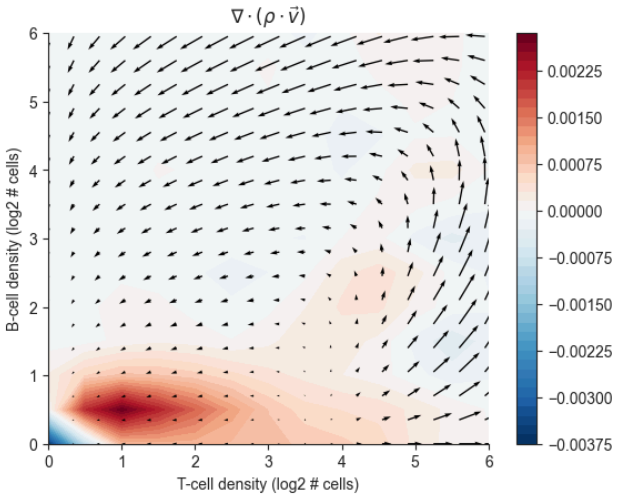

Bibliography:

Adler, Miri, Arun R. Chavan, and Ruslan Medzhitov. 2023. “Tissue Biology: In Search of a New Paradigm.” *Annual Review of Cell and Developmental Biology* 39 (1): 67–89. https://doi.org/10.1146/annurev-cellbio-120420-113830.

Adler, Miri, Avi Mayo, Xu Zhou, Ruth A. Franklin, Matthew L. Meizlish, Ruslan Medzhitov, Stefan M. Kallenberger, and Uri Alon. 2020. “Principles of Cell Circuits for Tissue Repair and Fibrosis.” *iScience* 23 (2): 100841. https://doi.org/10.1016/j.isci.2020.100841.

Armingol, Erick, Hratch M. Baghdassarian, and Nathan E. Lewis. 2024. “The Diversification of Methods for Studying Cell–Cell Interactions and Communication.” *Nature Reviews Genetics*, January, 1–20. https://doi.org/10.1038/s41576-023-00685-8.

Barbera-Guillem, E., M. B. Nelson, B. Barr, J. K. Nyhus, K. F. May, L. Feng, and J. W. Sampsel. 2000. “B Lymphocyte Pathology in Human Colorectal Cancer. Experimental and Clinical Therapeutic Effects of Partial B Cell Depletion.” *Cancer Immunology, Immunotherapy: CII* 48 (10): 541–49. https://doi.org/10.1007/pl00006672.

Binnewies, Mikhail, Edward W. Roberts, Kelly Kersten, Vincent Chan, Douglas F. Fearon, Miriam Merad, Lisa M. Coussens, et al. 2018. “Understanding the Tumor Immune Microenvironment (TIME) for Effective Therapy.” *Nature Medicine* 24 (5): 541–50. https://doi.org/10.1038/s41591-018-0014-x.

Brodt, P., and J. Gordon. 1978. “Anti-Tumor Immunity in B Lymphocyte-Deprived Mice. I. Immunity to a Chemically Induced Tumor.” *Journal of Immunology (Baltimore, Md.: 1950)* 121 (1): 359–62.

Browaeys, Robin, Wouter Saelens, and Yvan Saeys. 2020. “NicheNet: Modeling Intercellular Communication by Linking Ligands to Target Genes.” *Nature Methods* 17 (2): 159–62. https://doi.org/10.1038/s41592-019-0667-5.

Cai, Chen, Jin Zhang, Minyu Li, Zhen-Jie Wu, Ken H. Song, Tina W. Zhan, Lin-Hui Wang, and Ying-Hao Sun. 2016. “Interleukin 10-Expressing B Cells Inhibit Tumor-Infiltrating T Cell

Function and Correlate with T Cell Tim-3 Expression in Renal Cell Carcinoma." *Tumour Biology: The Journal of the International Society for Oncodevelopmental Biology and Medicine* 37 (6): 8209–18. https://doi.org/10.1007/s13277-015-4687-1.

Combes, Alexis J., Bushra Samad, and Matthew F. Krummel. 2023. "Defining and Using Immune Archetypes to Classify and Treat Cancer." *Nature Reviews. Cancer* 23 (7): 491–505. https://doi.org/10.1038/s41568-023-00578-2.

Curtis, Christina, Sohrab P. Shah, Suet-Feung Chin, Gulisa Turashvili, Oscar M. Rueda, Mark J. Dunning, Doug Speed, et al. 2012. "The Genomic and Transcriptomic Architecture of 2,000 Breast Tumours Reveals Novel Subgroups." *Nature* 486 (7403): 346–52. https://doi.org/10.1038/nature10983.

Danenberg, Esther, Helen Bardwell, Vito R. T. Zanotelli, Elena Provenzano, Suet-Feung Chin, Oscar M. Rueda, Andrew Green, et al. 2022. "Breast Tumor Microenvironment Structures Are Associated with Genomic Features and Clinical Outcome." *Nature Genetics* 54 (5): 660–69. https://doi.org/10.1038/s41588-022-01041-y.

Efremova, Mirjana, Miquel Vento-Tormo, Sarah A. Teichmann, and Roser Vento-Tormo. 2020. "CellPhoneDB: Inferring Cell–Cell Communication from Combined Expression of Multi-Subunit Ligand–Receptor Complexes." *Nature Protocols* 15 (4): 1484–1506. https://doi.org/10.1038/s41596-020-0292-x.

"Endocytosis as a Stabilizing Mechanism for Tissue Homeostasis | PNAS." n.d. Accessed December 21, 2023. https://www.pnas.org/doi/10.1073/pnas.1714377115.

Engelhard, Victor, Jose R. Conejo-Garcia, Rafi Ahmed, Brad H. Nelson, Karen Willard-Gallo, Tullia C. Bruno, and Wolf H. Fridman. 2021. "B Cells and Cancer." *Cancer Cell* 39 (10): 1293–96. https://doi.org/10.1016/j.ccell.2021.09.007.

Entenberg, David, Maja H. Oktay, and John S. Condeelis. 2023. "Intravital Imaging to Study Cancer Progression and Metastasis." *Nature Reviews Cancer* 23 (1): 25–42. https://doi.org/10.1038/s41568-022-00527-5.

Fridman, Wolf H., Maxime Meylan, Florent Petitprez, Cheng-Ming Sun, Antoine Italiano, and Catherine Sautès-Fridman. 2022. "B Cells and Tertiary Lymphoid Structures as Determinants of Tumour Immune Contexture and Clinical Outcome." *Nature Reviews Clinical Oncology* 19 (7): 441–57. https://doi.org/10.1038/s41571-022-00619-z.

Fridman, Wolf Herman, Florent Petitprez, Maxime Meylan, Tom Wei-Wu Chen, Cheng-Ming Sun, Lubka T. Roumenina, and Catherine Sautès-Fridman. 2020. "B Cells and Cancer: To B or Not to B?" *Journal of Experimental Medicine* 218 (1): e20200851. https://doi.org/10.1084/jem.20200851.

Gascard, Philippe, and Thea D. Tlsty. 2016. "Carcinoma-Associated Fibroblasts: Orchestrating the Composition of Malignancy." *Genes & Development* 30 (9): 1002–19. https://doi.org/10.1101/gad.279737.116.

Hickey, John W., Elizabeth K. Neumann, Andrea J. Radtke, Jeannie M. Camarillo, Rebecca T. Beuschel, Alexandre Albanese, Elizabeth McDonough, et al. 2022. "Spatial Mapping of Protein Composition and Tissue Organization: A Primer for Multiplexed Antibody-Based Imaging." *Nature Methods* 19 (3): 284–95. https://doi.org/10.1038/s41592-021-01316-y.

Horns, Felix, Joe A. Martinez, Chengcheng Fan, Mehernaz Haque, James M. Linton, Victoria Tobin, Leah Santat, et al. 2023. "Engineering RNA Export for Measurement and Manipulation of Living Cells." *Cell*, July, S009286742300689X. https://doi.org/10.1016/j.cell.2023.06.013.

Ishigami, Emi, Masahiro Sakakibara, Junta Sakakibara, Takahito Masuda, Hiroshi Fujimoto, Shouko Hayama, Takeshi Nagashima, et al. 2019. "Coexistence of Regulatory B Cells and Regulatory T Cells in Tumor-Infiltrating Lymphocyte Aggregates Is a Prognostic Factor in Patients with Breast Cancer." *Breast Cancer (Tokyo, Japan)* 26 (2): 180–89. https://doi.org/10.1007/s12282-018-0910-4.

Izhikevich, Eugene M., and Richard FitzHugh. 2006. "FitzHugh-Nagumo Model." *Scholarpedia* 1 (9): 1349. https://doi.org/10.4249/scholarpedia.1349.

Jerby-Arnon, Livnat, and Aviv Regev. 2022. "DIALOGUE Maps Multicellular Programs in Tissue

from Single-Cell or Spatial Transcriptomics Data." *Nature Biotechnology* 40 (10): 1467–77. https://doi.org/10.1038/s41587-022-01288-0.
Kafri, Ran, Jason Levy, Miriam B. Ginzberg, Seungeun Oh, Galit Lahav, and Marc W. Kirschner. 2013. "Dynamics Extracted from Fixed Cells Reveal Feedback Linking Cell Growth to Cell Cycle." *Nature* 494 (7438): 480–83. https://doi.org/10.1038/nature11897.
Kari, Sana, Kumar Subramanian, Ilenia Agata Altomonte, Akshaya Murugesan, Olli Yli-Harja, and Meenakshisundaram Kandhavelu. 2022. "Programmed Cell Death Detection Methods: A Systematic Review and a Categorical Comparison." *Apoptosis* 27 (7–8): 482–508. https://doi.org/10.1007/s10495-022-01735-y.
Keren, Leeat, Marc Bosse, Steve Thompson, Tyler Risom, Kausalia Vijayaragavan, Erin McCaffrey, Diana Marquez, et al. 2019. "MIBI-TOF: A Multiplexed Imaging Platform Relates Cellular Phenotypes and Tissue Structure." *Science Advances* 5 (10): eaax5851. https://doi.org/10.1126/sciadv.aax5851.
Kim, Jihoon, Bon-Kyoung Koo, and Juergen A. Knoblich. 2020. "Human Organoids: Model Systems for Human Biology and Medicine." *Nature Reviews Molecular Cell Biology* 21 (10): 571–84. https://doi.org/10.1038/s41580-020-0259-3.
Kirschenbaum, Daniel, Ken Xie, Florian Ingelfinger, Yonatan Katzenelenbogen, Kathleen Abadie, Thomas Look, Fadi Sheban, et al. 2023. "Time-Resolved Single-Cell Transcriptomics Defines Immune Trajectories in Glioblastoma." *Cell* 0 (0). https://doi.org/10.1016/j.cell.2023.11.032.
Kokkinos, John, George Sharbeen, Koroush S. Haghighi, Rosa Mistica C. Ignacio, Chantal Kopecky, Estrella Gonzales-Aloy, Janet Youkhana, et al. 2021. "Ex Vivo Culture of Intact Human Patient Derived Pancreatic Tumour Tissue." *Scientific Reports* 11 (1): 1944. https://doi.org/10.1038/s41598-021-81299-0.
La Manno, Gioele, Ruslan Soldatov, Amit Zeisel, Emelie Braun, Hannah Hochgerner, Viktor Petukhov, Katja Lidschreiber, et al. 2018. "RNA Velocity of Single Cells." *Nature* 560 (7719): 494–98. https://doi.org/10.1038/s41586-018-0414-6.
Laumont, Céline M., Allyson C. Banville, Mara Gilardi, Daniel P. Hollern, and Brad H. Nelson. 2022. "Tumour-Infiltrating B Cells: Immunological Mechanisms, Clinical Impact and Therapeutic Opportunities." *Nature Reviews Cancer* 22 (7): 414–30. https://doi.org/10.1038/s41568-022-00466-1.
Lebel, Yael, Tomer Milo, Alon Bar, Avi Mayo, and Uri Alon. 2023. "Excitable Dynamics of Flares and Relapses in Autoimmune Diseases." *iScience* 26 (11). https://doi.org/10.1016/j.isci.2023.108084.
Lee-Chang, Catalina, Monica Bodogai, Alejandro Martin-Montalvo, Katarzyna Wejksza, Mitesh Sanghvi, Ruin Moaddel, Rafael de Cabo, and Arya Biragyn. 2013. "Inhibition of Breast Cancer Metastasis by Resveratrol-Mediated Inactivation of Tumor-Evoked Regulatory B Cells." *Journal of Immunology (Baltimore, Md.: 1950)* 191 (8): 4141–51. https://doi.org/10.4049/jimmunol.1300606.
Leung, Chak Ming, Pim de Haan, Kacey Ronaldson-Bouchard, Ge-Ah Kim, Jihoon Ko, Hoon Suk Rho, Zhu Chen, et al. 2022. "A Guide to the Organ-on-a-Chip." *Nature Reviews Methods Primers* 2 (1): 1–29. https://doi.org/10.1038/s43586-022-00118-6.
Martins, Filipe, Latifyan Sofiya, Gerasimos P. Sykiotis, Faiza Lamine, Michel Maillard, Montserrat Fraga, Keyvan Shabafrouz, et al. 2019. "Adverse Effects of Immune-Checkpoint Inhibitors: Epidemiology, Management and Surveillance." *Nature Reviews Clinical Oncology* 16 (9): 563–80. https://doi.org/10.1038/s41571-019-0218-0.
Mayer, Shimrit, Tomer Milo, Achinoam Isaacson, Coral Halperin, Shoval Miyara, Yaniv Stein, Chen Lior, et al. 2023. "The Tumor Microenvironment Shows a Hierarchy of Cell-Cell Interactions Dominated by Fibroblasts." *Nature Communications* 14 (1): 5810. https://doi.org/10.1038/s41467-023-41518-w.
Miyara, Shoval, Miri Adler, Elad Bassat, Yalin Divinsky, Kfir B. Umansky, Jacob Elkahal, Alexander Genzelinakh, et al. 2023. "Circuit to Target Approach Defines an Autocrine Myofibroblast Loop That Drives Cardiac Fibrosis." bioRxiv.

https://doi.org/10.1101/2023.01.01.522422.
Murakami, Yuki, Hiroaki Saito, Shota Shimizu, Yusuke Kono, Yuji Shishido, Kozo Miyatani, Tomoyuki Matsunaga, et al. 2019. “Increased Regulatory B Cells Are Involved in Immune Evasion in Patients with Gastric Cancer.” *Scientific Reports* 9 (1): 13083. https://doi.org/10.1038/s41598-019-49581-4.
Murphy, Kenneth, and Casey Weaver. 2016. *Janeway’s Immunobiology*. Garland Science.
Oleinika, Kristine, Claudia Mauri, and Alan D. Salama. 2019. “Effector and Regulatory B Cells in Immune-Mediated Kidney Disease.” *Nature Reviews Nephrology* 15 (1): 11–26. https://doi.org/10.1038/s41581-018-0074-7.
Oyler-Yaniv, Alon, Jennifer Oyler-Yaniv, Benjamin M. Whitlock, Zhiduo Liu, Ronald N. Germain, Morgan Huse, Grégoire Altan-Bonnet, and Oleg Krichevsky. 2017. “A Tunable Diffusion-Consumption Mechanism of Cytokine Propagation Enables Plasticity in Cell-to-Cell Communication in the Immune System.” *Immunity* 46 (4): 609–20. https://doi.org/10.1016/j.immuni.2017.03.011.
Pereira, Bernard, Suet-Feung Chin, Oscar M. Rueda, Hans-Kristian Moen Vollan, Elena Provenzano, Helen A. Bardwell, Michelle Pugh, et al. 2016. “The Somatic Mutation Profiles of 2,433 Breast Cancers Refines Their Genomic and Transcriptomic Landscapes.” *Nature Communications* 7 (May): 11479. https://doi.org/10.1038/ncomms11479.
Pittet, Mikael J., Christopher S. Garris, Sean P. Arlauckas, and Ralph Weissleder. 2018. “Recording the Wild Lives of Immune Cells.” *Science Immunology* 3 (27): eaaq0491. https://doi.org/10.1126/sciimmunol.aaq0491.
Qin, Zhihai, Günther Richter, Thomas Schüler, Sabrina Ibe, Xuetao Cao, and Thomas Blankenstein. 1998. “B Cells Inhibit Induction of T Cell-Dependent Tumor Immunity.” *Nature Medicine* 4 (5): 627–30. https://doi.org/10.1038/nm0598-627.
Quinn, Jeffrey J., Matthew G. Jones, Ross A. Okimoto, Shigeki Nanjo, Michelle M. Chan, Nir Yosef, Trever G. Bivona, and Jonathan S. Weissman. 2021. “Single-Cell Lineages Reveal the Rates, Routes, and Drivers of Metastasis in Cancer Xenografts.” *Science* 371 (6532): eabc1944. https://doi.org/10.1126/science.abc1944.
“Quorum Sensing Allows T Cells to Discriminate between Self and Nonself.” n.d. Accessed January 15, 2024. https://doi.org/10.1073/pnas.1222467110.
Sahai, Erik, Igor Astsaturov, Edna Cukierman, David G. DeNardo, Mikala Egeblad, Ronald M. Evans, Douglas Fearon, et al. 2020. “A Framework for Advancing Our Understanding of Cancer-Associated Fibroblasts.” *Nature Reviews Cancer* 20 (3): 174–86. https://doi.org/10.1038/s41568-019-0238-1.
Schürch, Christian M., Salil S. Bhate, Graham L. Barlow, Darci J. Phillips, Luca Noti, Inti Zlobec, Pauline Chu, et al. 2020. “Coordinated Cellular Neighborhoods Orchestrate Antitumoral Immunity at the Colorectal Cancer Invasive Front.” *Cell* 182 (5): 1341-1359.e19. https://doi.org/10.1016/j.cell.2020.07.005.
Setten, Elisa, Alessandra Castagna, Josué Manik Nava-Sedeño, Jonathan Weber, Roberta Carriero, Andreas Reppas, Valery Volk, et al. 2022. “Understanding Fibrosis Pathogenesis via Modeling Macrophage-Fibroblast Interplay in Immune-Metabolic Context.” *Nature Communications* 13 (1): 6499. https://doi.org/10.1038/s41467-022-34241-5.
Shah, Sangeeta, Anagha A. Divekar, Shannon P. Hilchey, Hyun-Mi Cho, Corliss L. Newman, Seung-Uon Shin, Hovav Nechustan, et al. 2005. “Increased Rejection of Primary Tumors in Mice Lacking B Cells: Inhibition of Anti-Tumor CTL and TH1 Cytokine Responses by B Cells.” *International Journal of Cancer* 117 (4): 574–86. https://doi.org/10.1002/ijc.21177.
Shalapour, Shabnam, Joan Font-Burgada, Giuseppe Di Caro, Zhenyu Zhong, Elsa Sanchez-Lopez, Debanjan Dhar, Gerald Willimsky, et al. 2015. “Immunosuppressive Plasma Cells Impede T-Cell-Dependent Immunogenic Chemotherapy.” *Nature* 521 (7550): 94–98. https://doi.org/10.1038/nature14395.
Shalapour, Shabnam, Xue-Jia Lin, Ingmar N. Bastian, John Brain, Alastair D. Burt, Alexander A.

Aksenov, Alison F. Vrbanac, et al. 2017. “Inflammation-Induced IgA+ Cells Dismantle Anti-Liver Cancer Immunity.” *Nature* 551 (7680): 340–45. https://doi.org/10.1038/nature24302.

“The Spectrum of Inflammatory Responses.” n.d. Accessed December 20, 2023. https://doi.org/10.1126/science.abi5200.

Tirado-Lee, Leidamarie. n.d. “Spatially Resolved Transcriptomics: An Introductory Overview of Spatial Gene Expression Profiling Methods.” 10x Genomics. Accessed August 6, 2023. https://www.10xgenomics.com/blog/spatially-resolved-transcriptomics-an-introductory-overview-of-spatial-gene-expression-profiling-methods.

Tlsty, Thea D., and Lisa M. Coussens. 2006. “Tumor Stroma and Regulation of Cancer Development.” *Annual Review of Pathology* 1: 119–50. https://doi.org/10.1146/annurev.pathol.1.110304.100224.

Uxa, Sigrid, Paola Castillo-Binder, Robin Kohler, Konstanze Stangner, Gerd A. Müller, and Kurt Engeland. 2021. “Ki-67 Gene Expression.” *Cell Death & Differentiation* 28 (12): 3357–70. https://doi.org/10.1038/s41418-021-00823-x.

Wang, Shuang, Kenneth Li, Eliana Pickholz, Ross Dobie, Kylie P. Matchett, Neil C. Henderson, Chris Carrico, et al. 2023. “An Autocrine Signaling Circuit in Hepatic Stellate Cells Underlies Advanced Fibrosis in Nonalcoholic Steatohepatitis.” *Science Translational Medicine* 15 (677): eadd3949. https://doi.org/10.1126/scitranslmed.add3949.

Weinberg, Robert A. 2014. *The Biology of Cancer*. Second edition. New York: Garland Science, Taylor & Francis Group.

Weinreb, Caleb, Samuel Wolock, Betsabeh K. Tusi, Merav Socolovsky, and Allon M. Klein. 2018. “Fundamental Limits on Dynamic Inference from Single-Cell Snapshots.” *Proceedings of the National Academy of Sciences* 115 (10): E2467–76. https://doi.org/10.1073/pnas.1714723115.

Wu, Sunny Z., Ghamdan Al-Eryani, Daniel Lee Roden, Simon Junankar, Kate Harvey, Alma Andersson, Aatish Thennavan, et al. 2021. “A Single-Cell and Spatially Resolved Atlas of Human Breast Cancers.” *Nature Genetics* 53 (9): 1334–47. https://doi.org/10.1038/s41588-021-00911-1.

Yoshizaki, Ayumi, Tomomitsu Miyagaki, David J. DiLillo, Takashi Matsushita, Mayuka Horikawa, Evgueni I. Kountikov, Rosanne Spolski, Jonathan C. Poe, Warren J. Leonard, and Thomas F. Tedder. 2012. “Regulatory B Cells Control T-Cell Autoimmunity through IL-21-Dependent Cognate Interactions.” *Nature* 491 (7423): 264–68. https://doi.org/10.1038/nature11501.

Yuen, Grace J., Ezana Demissie, and Shiv Pillai. 2016. “B Lymphocytes and Cancer: A Love-Hate Relationship.” *Trends in Cancer* 2 (12): 747–57. https://doi.org/10.1016/j.trecan.2016.10.010.